NASA CR-132550

STUDY OF PROVIDING OMNIDIRECTIONAL VIBRATION ISOLATION TO ENTIRE SPACE SHUTTLE PAYLOAD PACKAGES

By C.S. Chang

Prepared under Contract No. NAS1-12290 by
New Technology, Inc.
Huntsville, Alabama

for

NATIONAL AERONAUTICS AND SPACE ADMINISTRATION

FOREWORD

This final report is prepared for National Aeronautics and Space Administration, Langley Research Center, Hampton, Virginia, by New Technology, Inc., under contract NAS1-12290, "Study of Providing Omnidirectional Vibration Isolation to Entire Space Shuttle Payload Packages."

The Technical Representative for NASA was Dr. Robert W. Fralich, Structural Mechanics Branch, Structures and Dynamics Division, Langley Research Center. The principal investigators were C.S. Chang, G.D. Robinson, and D.E. Weber.

CONTENTS

LIST OF FIGURES

SUMMARY

Techniques to provide omnidirectional vibration isolation for a Space Shuttle Payload Package were investigated via reduced-scale model studies. Development, design, fabrication, assembly and test evaluation of a 0.125-scale isolation model are described in this report. This model was designed for direct inclusion in a similarly scaled structural dynamics model of the Space Shuttle system of NASA/Langley Research Center where further investigations of isolation techniques and their benefits are intended.

Final drawings for fabricated mechanical components are identified in the report. Prints of all drawings are included in separate covers as Appendix A.

Section 1

INTRODUCTION

With economy and versatility established as basic goals in the development of the Space Shuttle, the consideration of built-in means to provide a reduced vibrational environment to the entire payload package is consistent with program objectives. Initial developmental and installational costs for a vibration isolation system in the Orbiter should easily see returns in terms of lowered costs for payload packaging development and for vibration qualification tests, for each and every payload.

Described in this report is a feasibility study directed toward the development of a technology for providing omnidirectional vibration isolation. Both passive and active damping techniques were investigated. A fully functioning, reduced-scale model of an isolation system with a simulated payload was developed, fabricated, and test evaluated. This model system was designed for easy integration into Langley Research Center's 0.125-scale structural dynamics model of the Space Shuttle system for further developmental studies in payload isolation technology, and for experimental investigation of related dynamic control problems involving a softly sprung and highly damped payload.

It is anticipated that results of the program will serve as preliminary engineering data which are useful for full-scale system design and for evaluation of system economy with and without total payload package isolation.

For the Space Shuttle, the frequency of vibration excitation of significant magnitude extends from the very low (less than one Hertz due to, say, wind and gust) into mid-audio range (several thousand Hertz, created by rocket engine noises, aerodynamic turbulances, etc.). A large number of natural modes of vibration of the vehicle will be excited. Consequently, vibration isolation for the payload package in all directions is desirable.

Principles of vibration isolation are well known and require no elaboration in this report. Only a summary of the general results are outlined below:

By definition, a payload package is to be delivered by a vehicle from one point to another in space. Consequently, the payload and the vehicle must be coupled to each other. The requirement of deliverability, however, demands only static or quasi-static coupling. To minimize dynamic loads, it is desirable to uncouple the two structures so that vibrations are not "transmitted" to the contents of the payload package. An ideal payload suspension system would, therefore, provide both static coupling and dynamic decoupling simultaneously.

Dynamic decoupling can be achieved by minimizing both the stiffness and the damping of the interface between the payload and the vehicle to the point where low-frequency response magnitudes approach those allowed by clearances between them.

Suspension design and calculation approaches are described in Section 2. Damper requirements and the design of a damper system for subdueing low-frequency vibrations in the longitudinal direction are discussed in Section 3. An active system was selected to provide lateral damping between the simulated payload and the Orbiter model. Section 4 describes project efforts associated

with the development of mechanical, electromagnetic and electronic components of this active damper system.

Hardware fabrication and system assembly are described in Section 5 .

Three phases of tests were conducted. Small shakers were used in Phase I, Dynamic Calibration, and in Phase II, Isolation Performance Tests,at New Technology, Inc., (NTI). A very large shaker was used to generate prescribed "base acceleration" environment to the specimen during Phase III tests. Test approaches, procedures, equipment and instrumentation are summarized in Section 6.

Conclusions and a number of recommendations are presented in the last section of this report.

Section 2

SUSPENSION DESIGN FOR THE SIMULATED PAYLOAD

2.1 SIMULATED PAYLOAD PACKAGE

The 0.125-scale structural dynamics model of the Space Shuttle was completed during the Summer of 1973. The first-generation payload models are a number of simple structural elements which simulate anticipated payloads in inertial properties only. The basic model payload design (Reference 1) uses two 15.24 cm (6" x 2.83#) standard aluminum channels, welded to form a box beam. Four beam lengths were used: 200 cm, 111 cm, 57 cm and 46 cm. The beam-shaped payload simulators are pin-connected to Orbiter bulkheads. There is, therefore, no deliberate vibration isolation provision.

In the current study, an aluminum circular cyclinder (NTI DWG. 20088)* of the following dimensions is used as the main element of yet another simulated payload package:

O.D. = 11.430 cm (4.500")

I.D. = 10.230 cm (4.026")

Length = 72.187 cm (28.420")

The cross-sectional dimensions of the circular tube were selected to provide approximately the same properties as the box-beam payload simulators. The length of the tube was selected to provide a simulated payload assembly which can be incorporated easily into the Orbiter model. The new payload simulator includes a permanent magnet assembly on each end of the aluminum tube (see NTI DWGS. 20084 and 20092)** The overall length of the composite payload simulator is 99.3 cm, and its total mass is 23 kg.

*A complete set of drawings have been turned over to NASA/LaRC. They are also available from NTI on request. For a pictorial view of the item, see also Figure 23.

** See also Figure 27

2.2 SUSPENSION DESIGN

2.2.1 Requirements

The design objective of the suspension system is to separate the overall vibration modes of the entire Space Shuttle vehicle into two distinct groups on the frequency axis in such a way that mode shapes for the lower-frequency group involve "rigid-body" payload displacements only. In a proper suspension design, the creation of these rigid-body payload modes would make it possible to prevent high-frequency vibrations from reaching the payload. (i.e., such that the magnitude of the mode shape on the payload for each and every high-frequency mode is significantly lowered from what it would have been without the suspension). What distinguishes isolation requirements of this project from those for the more common situation is that isolation in all directions must be achieved simultaneously, and that the degree of isolation must be preserved for all "static preload" conditions in all directions corresponding to true static preloads due to gravitation and due to low-frequency vehicle accelerations during boost, maneuvering, wind drift, etc.

Had the purpose of this investigation been to develop a true-to scale omnidirectional vibration isolation model for the Space Shuttle, quantitative design specifications must be derived from the above-mentioned combination of static, quasi-static and dynamic environments. They would, in turn, lead to detailed specifications for such performance characteristics as:

(a) Rigid-body frequencies of the payload.

(b) Maximum allowable relative displacements between the payload and the Orbiter.

(c) Maximum acceleration levels to be endured, its spectral shape and duration in or on the payload package

(d) Weight, size, strength, life expectancy, etc., of the system

In this preliminary study, however, some of these detailed and complex requirements could not have been established as the schedule was too early with respect to the overall Shuttle program. Other requirements were often waived in consideration of a direct and concise effort on the central issue of establishing feasibility of omnidirectional payload vibration isolation itself. For example, strength, maximum deflection and similar requirements which specify the allowable loads of the suspension system were not rigidly set up. Instead, practicality and "reasonableness" in the model scale were used during the design process to develop a system whose capabilities are compatible with the vehicle model. On the other hand, suspension properties such as stiffness and inherent damping were more accurately designed.* As shown by test data in Section 6, the resulting system developed under this philosophy represents a very "usable" model for study purposes of this and future projects involving the Shuttle model.

2.2.2 Approach

Several types of suspension elements were considered for the vibration isolation system. The selected approach utilizes pre-tensioned steel cables exclusively. Compared with a system made up of coil springs, flexures, or air springs and the like, a pre-tensioned cable system has the following advantages:

---

* For example, the suspension system stiffness was designed to place rigid-body payload modes below 8 Hz in all lateral directions; and below 12 Hz in the longitudinal direction. These limits were established on the basis of preliminary modal analyses of the full-scale Space Shuttle in mid-1973.

(a) Among all concepts investigated, it led to the simplest configuration.

(b) It is practical to scale the cable and, hence, the suspension system, up to a full-scale design.

(c) The simplicity of the system makes it more reliable. It should be relatively easy to qualify for flight hardware.

(d) It does not require a new manufacturing technology.

2.2.3 Configuration

The suspension system configuration is schematically illustrated in Figure 1. The stiffness of the system is governed by the pre-tension of the cables, which are designed to place the natural frequencies of rigid-body payload modes below 8 Hz in all lateral directions, and below 12 Hz in the axial direction.

2.2.4 Design Analysis

When the suspension system is correctly designed, it should be light and compliant so that high-frequency modes of the payload-vehicle system will be insensitive to small variations of its stiffness characteristics. On the other hand, the low frequency modes are very much stiffness dependent. For design calculation purposes, the low-frequency mode shapes will be assumed, a priori, to contain rigid-body displacements of both the payload and the vehicle, so that all deformations take place in the suspension system.

For a rigid-body translational mode, let

i = mode index;

m_p = payload mass;

m_v = vehicle mass;

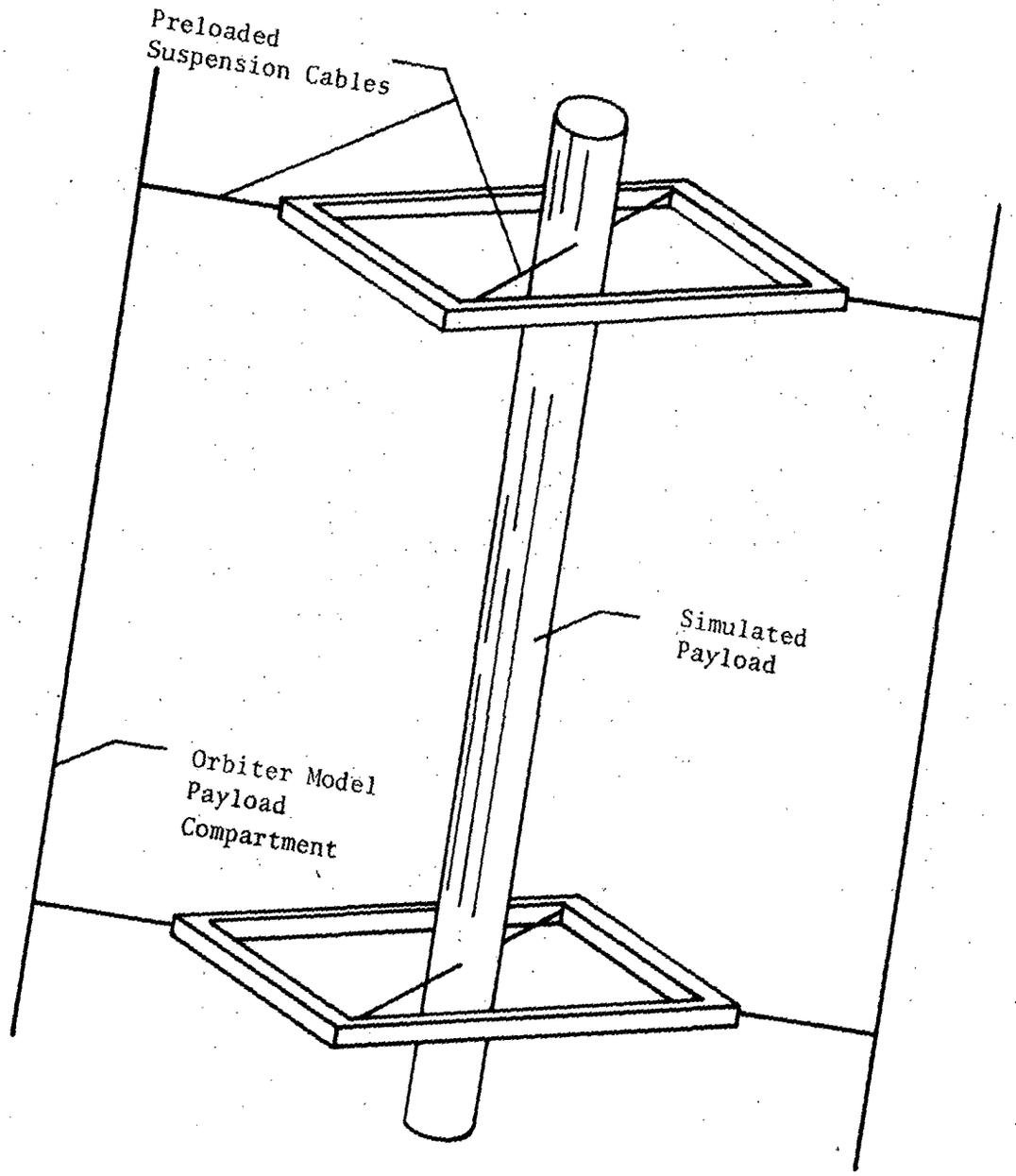

Figure 1 Omnidirectional Suspension Schematics

K_i = stiffness of the suspension in the assumed mode shape;

X_p = absolute displacement of the payload in the i^{th} mode;

X_v = absolute displacement of the vehicle in the i^{th} mode;

and ω_i = undamped angular natural frequency of the i^{th} mode.

The undamped mode shaped is determined from conservation of linear momentum and is given by

$$X_v/X_p = m_p/m_v . \tag{1}$$

The relative displacement between the payload and the vehicle, X_i, is the normal coordinate for that mode

$$X_i = (1+ m_p/m_v)\ X_p. \tag{2}$$

Equation (2) is very useful since it allows the designer to estimate the relative displacement by

(a) assuming the vehicle to be stationary (i.e., assuming $m_p \ll m_v$),

(b) determining the payload vibration amplitude, and

(c) applying the correction factor $(1+m_p/m_v)$ in accordance with Equation (2).

The angular natural frequency of the mode is given by the equation:

$$\omega_i^2 = (1+m_p/m_v)\ K_i/m_p. \tag{3}$$

Consequently,

$$\omega_i = (1+ m_p/m_v)^{\frac{1}{2}}\ \omega_i', \tag{4}$$

where $\omega'_i = (K_i/m_p)^{\frac{1}{2}}$ is the angular natural frequency obtained by assuming $m_p/m_v = 0$.

Similar expressions may be derived for each of the rigid-body payload rotational modes.

The most severe vibration environment for the Space Shuttle is expected during boost phases of the flight. Consequently, vibration isolation of the payload is most critically needed during this time when the vehicle mass is the greatest. It is, therefore, justifiable in the following to assume $m_p/m_v \ll 1$ for suspension stiffness design purposes.

The assumed mode shapes are such that one of the principal axes of vibration is always in the direction of the preload. The other two principal axes are perpendicular to this direction and to each other. Design calculations are relatively simple since only two types of force-deflection relationships have to be analyzed, and only for simple pairs of pre-tensioned cables.

Figure 2 shows a pair of pre-tensioned suspension cables under an applied force F. The force-deflection relationship at mid-span is dependent on the pre-tension, T_o, in the cables. Let

EA = uni-axial stiffness of the cable,

L = semi-span;

F = force applied at mid-span;

D = deflection at mid-span under F;

and T = total tension in the cable.

The following force-deflection relationship is derived:

$$F = 2(D/L)\ \{T_o + EA\ [(1+D^2/L^2)^{\frac{1}{2}} - 1]\}\ /\ (1+D^2/L^2)^{\frac{1}{2}} \qquad (5)$$

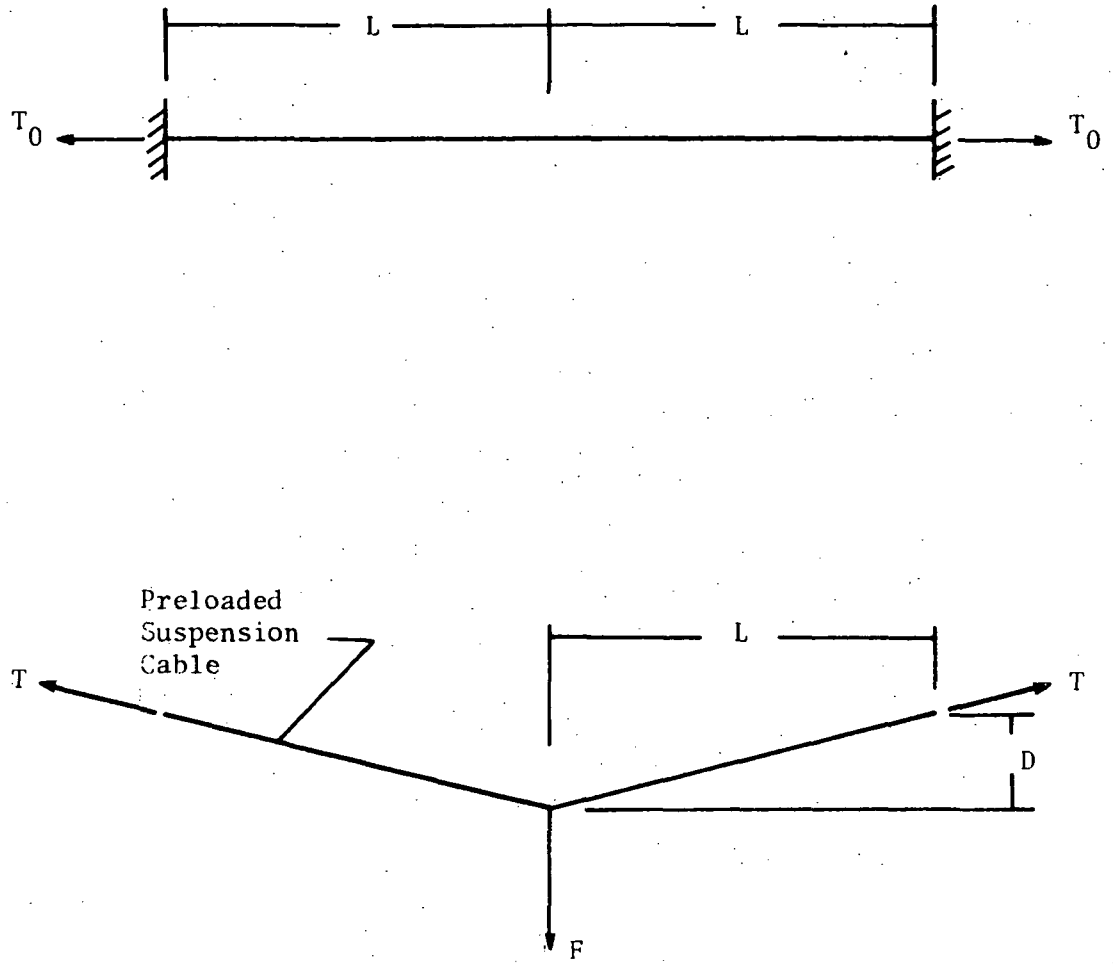

Figure 2 Suspension Cable Force - Displacement Nomenclature

The expression for the total tension is

$$T = T_o + EA\left[(1+D^2/L^2)^{\frac{1}{2}} - 1\right]. \qquad (6)$$

The small-deflection stiffness, K, for any static loading condition is given by the expression

$$K = \frac{dF}{dD} = 2\{EA[(1+D^2/L^2)^{3/2}-1]+T_o\}/[L(1+D^2/L^2)^{3/2}] \approx (3EAD^2/L^2+2T_o)/L. \qquad (7)$$

The desired value of K is determined by natural frequency considerations and is approximately 3.5 kN/m. The permissible length of each cable is limited to approximately 10 cm by the size of the 0.125 scale of the Orbiter. The static deflection due to earth's gravity is determined by clearance considerations for the dampers and is limited to a value of approximately 0.5 cm. After a number of iterations, the following design was selected:

Cable: .159 cm diam., 7x7 CRES aircraft cable with

$EA = 2.23 \times 10^5$ N and $T_{max} = 2{,}170$ N

$L = 9.860$ cm;

$T_o = 774$ N;

$K = 3.37$ kN/m

Cable design details are found in NTI DWGs. 20091-1 and -2.*

The calculated upper limit of the natural frequency of the rigid-body payload translational mode in the direction of the preload due to earth's gravity is 8.1 Hz.

The natural frequency of the rigid-body payload roll mode is made low by attaching the suspension cables near the longitudinal centerline of the payload.

*See also Figure 24

The natural frequency of the rigid-body translational mode in a direction normal to the static preload is bounded from above by the simple pendulum frequency in the inertial preload field, see Figure 3. In the earth's gravity and for a static preload deflection of 0.5 cm, the calculated natural frequency is 7 Hz.

The natural frequency of the rigid-body payload translational mode in the axial direction is controlled by mechanical design features of the active damper system in addition to the above cables and is about 12 Hz.

The natural frequencies of the remaining two rigid-body rotational modes are controlled by suitable positioning of the cable attachment points along the length of the payload and are both less than 8 Hz for the same preload condition and for the corresponding rotational inertial of the payload.

According to the above discussions and Equations (5) and (7), natural frequencies for all six assumed rigid-body modes are reduced, from the above-mentioned values for the preloaded condition, as the preload is reduced. The assumption of the existence of these rigid body modes is, therefore, justified for all preload conditions as the natural frequencies will be significantly lower than those of the Space Shuttle model without the isolated payload package.

The suspension system is implemented with the help of a cage structure (NTI DWG. 20093)*which also serve as the interface between the suspension system and the Orbiter. The assembled payload, suspension, cage and installation in the Orbiter Payload compartment are shown in NTI DWG 20094.

---

*See also Figure 27.

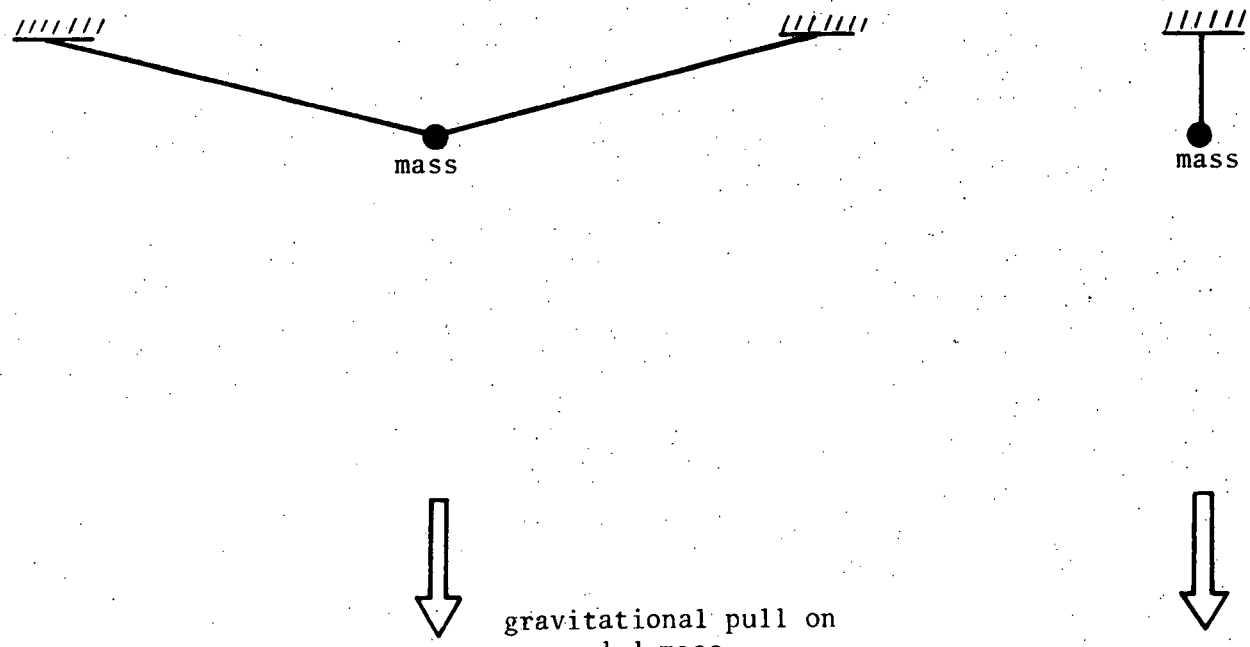

Figure 3 Pendulum Mode of Rigid-Body Oscillation of Suspended Payload

Section 3

DAMPING

3.1 DAMPING REQUIREMENTS

The compliant suspension system isolates the payload from high-frequency vibrations of the vehicle while creating low-frequency payload rigid-body modes which are easily excited to large displacement amplitudes by low-level, low-frequency forcing functions on the vehicle. Dampers are, therefore, required to limit relative displacement amplitudes.*

In the following derivation of requirements for damper characteristics, the payload, the vehicle, the suspension system and the damper are schematically represented for each mode by the system in Figure 4. The equation of motion written in terms of the relative displacement X_i is

$$m_p \ddot{X}_i + C_i(1+m_p/m_v)\,\dot{X}_i + K_i(1+m_p/m_v)\,X_i = -(m_p/m_v)F(t) \qquad (8)$$

where C_i is the coefficient of the damper, and $F(t)$ is the force on m_v.

---

* In the suspension system design, only those elements and joint constructions with low damping are used. In this manner, dampers may be developed independently of the suspension system.

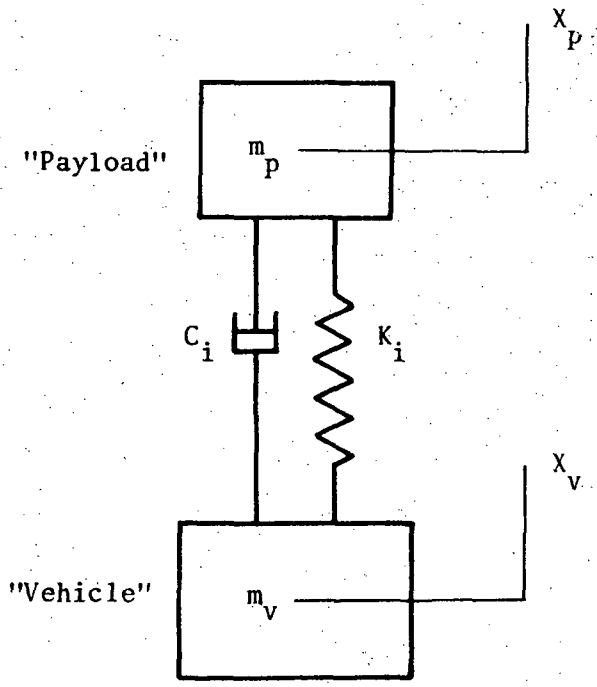

Figure 4 Schematic Representation of Suspended Payload and Vehicle

The modal damping factor is

$$\zeta_i = C_i \, (1+m_p/m_v)^{1/2} \, /(2m_p\omega_i') \ , \tag{9}$$

or $$\zeta_i \approx C_i/(2m_p\omega_i'), \text{ for } m_v >> m_p . \tag{10}$$

According to the frequency response function derived from Equation (8), the optimum damping factor is approximately 0.65. The corresponding damper coefficient is

$$C_i = 2 \times 0.65 \, m_p \, \omega_i' \ . \tag{11}$$

For lateral translational modes

$$\omega_i \leq 2\pi \times 8 = 50 \text{ radians/sec} \ ,$$

and $$m_p = 23 \ k_g \ ,$$

and the required damper coefficient for these modes is

$$C_i < 1.5 \text{ kN/m/sec}$$

For the longitudinal mode , the angular natural frequency is <75.4 rad/sec. and the required damper coefficient is <2.25 kN/m/sec.

Damper coefficients greater than these values are both unnecessary (for the rigid-body modes) and harmful (since greater high-frequency vibration is "transmitted" with higher damping).

In addition, the dampers must maintain the above specified characteristics throughout the specified static deflection range due to preloads in any direction.

3.2 LONGITUDINAL DAMPERS

3.2.1 Approach

For the full-scale Space Shuttle, the greatest low-frequency excitation is expected to be in the longitudinal direction. It is, therefore, desirable to implement a model damper which has the potential to be scaled up -- in size, in damping coefficient, in force capability and, most importantly, in being practical. This last requirement may be intuitively translated as possessing an optimum mixture of such characteristics as simplicity, reliability, ruggedness and care-free operations. One such damper is the squeeze-film damper (References 2,3, and 4). The basic configuration is shown schematically in Figure 5. If an incompressible viscous fluid is used between the two parallel plates, the expression for the normal force, F_s, developed to resist the separation of the plates is

$$F_s = 3\pi\mu V R^4/2h^3, \qquad (12)$$

where μ = absolute viscosity of the fluid film between the plates

V = relative normal velocity of plate separation

R = radius of the fluid film

h = nominal distance between the plates

The damping coefficient for small-amplitude vibrations is, therefore,

$$C_s = 3\pi\mu R^4/2h^3. \qquad (13)$$

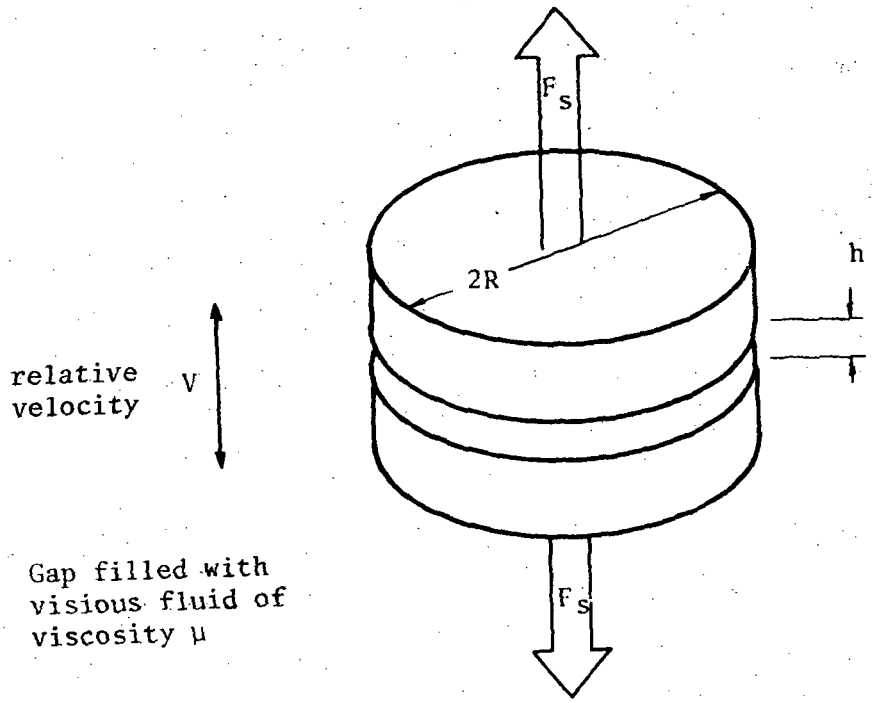

$$F_s = 3\Pi\mu VR^4/2h^3$$

Figure 5 Basic Squeeze-Film Damper Configuration

The advantages of this damper are

(a) Large damping coefficients can be easily obtained.

(b) It can tolerate large parallel displacements of the plates.

Equation (13) indicates a potential disadvantage of the squeeze-damper: The damping coefficient is a highly nonlinear function of the distance between the plates. In order to reduce the dynamic coupling between the vehicle and the payload at high frequencies for reduced transmissibility, one of the plates is placed in series with a spring,* as shown in Figure 6. The effect of the additional spring is analyzed below.

The vehicle, the payload, the suspension and the damper are schematically represented by the two mass system in Figure 7. The damper force and the force in the auxiliary spring are equal:

$$C_i(\dot{X}_p - \dot{X}') = K'(X' - X_v) , \tag{14}$$

or

$$C_i(\dot{X}_p - \dot{X}') + K'(X_p - X') = K'(X_p - X_v) . \tag{15}$$

Taking Laplace transform of both sides:

$$(C_i s + K')[\, x_p(s) - x'(s)] = K' x_i(s) . \tag{16}$$

---

* Subsequent tests indicated that the spring, while successful in reducing transmission of high frequency vibrations, also limited the maximum damping achievable at low frequencies. Modifications were made after the first series of tests to eliminate these springs. The design analyses are kept in this report to document the original approach.

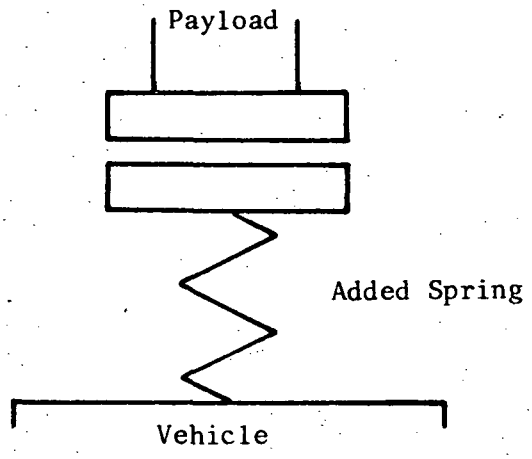

Figure 6 Spring in Series with Damper Plate

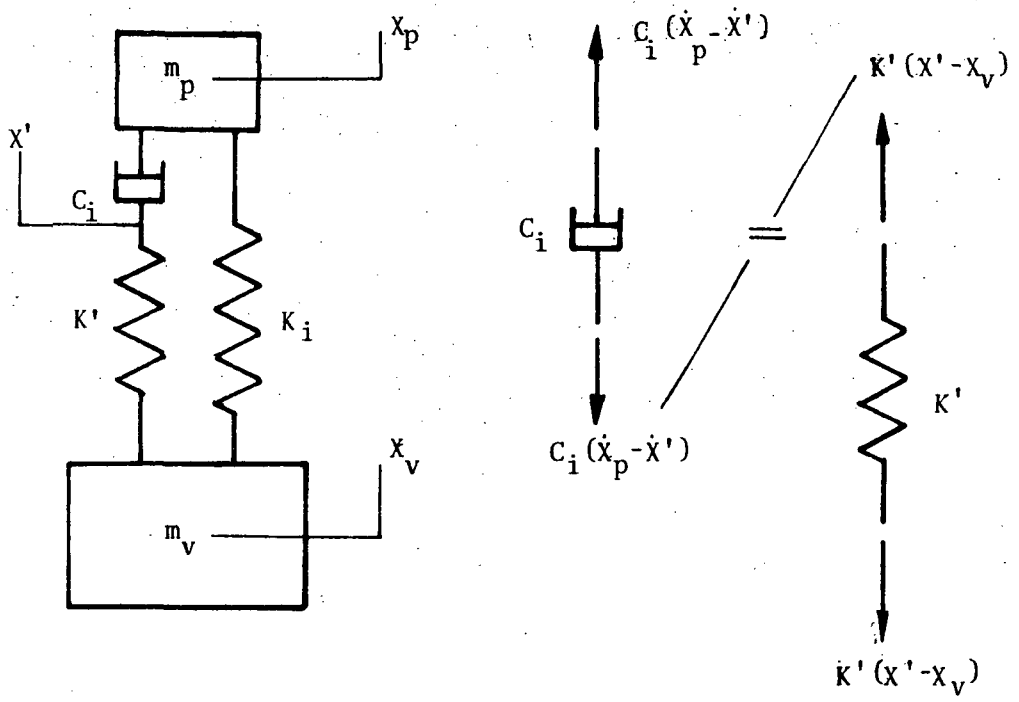

Figure 7 Damper in Series with Spring in a Two-Mass System

Consequently,

$$C_i s\,[x_p(s) - x'(s)] = C_i K' s\, x_i(s)/(C_i s + K'). \qquad (17)$$

The equation of motion of the system, written in terms of the relative displacement X_i is

$$m_p \ddot{X}_i + K_i(1+m_p/m_v)\, X_i + C_i(1+m_p/m_v)(\dot{X}_p - \dot{X}') = -\frac{m_p}{m_v} F(t). \qquad (18)$$

After taking the Laplace transform of both sides of Equation (18) and inserting Equations (4), (9) and (17), the following solution of $x_i(s)$ is obtained:

$$x_i(s) = \frac{-f(s)/m_v}{s^2 + \omega_i 2 + 2\zeta_i \omega_i s/(1+C_i s/K')},$$

where f(s) is the transform of F(t). The addition of a series spring of stiffness K' to the damper, therefore, introduces a first-order roll-off of the damping factor, ζ_i, with a cut-off frequency established by the factor C_i/K'.

3.2.2 Design

Because of the high compliance of the suspension system in the longitudinal direction, relatively large static deflection of the payload with respect to the vehicle is to be expected. For operations in the Orbiter model, the squeeze-film damper must function properly when the payload axis is vertical, horizontal or in between. The resulting variation of the operating gap of a squeeze-film damper will introduce variations of the damping coefficient which are too large to be tolerated. In order to minimize this problem, two squeeze-film dampers are used in the design, see Figure 8. In orientation (A), with the payload-axis vertical, Damper Unit (1) would provide nearly all of the damping forces since its operating gap is much smaller. In Orientation (B), with the payload axis horizontal, Damper Unit

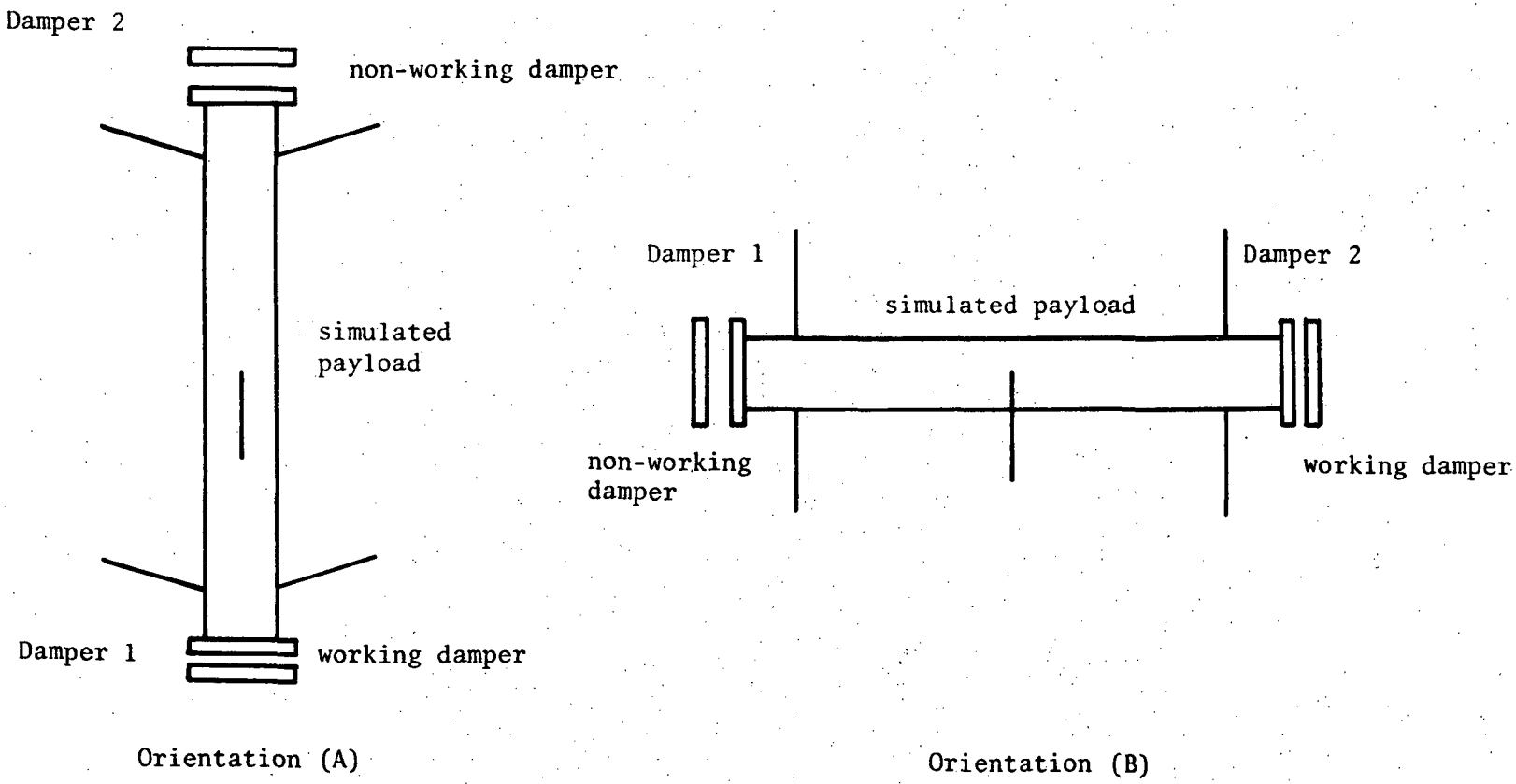

Figure 8 Method to Provide Proper Damping in Various Payload Orientations

(1) loses its effectiveness while the gap in Damper Unit (2) closes and it becomes the governing damper. For in-between orientations, both dampers are contributing. It should be noted that the design does not permit inverted vertical orientations of the payload as the gap of Damper Unit (2) will be completely closed.

In the final design of the model system, the nominal operating gap is 0.5 cm. Other design features are:

(a) The parallel plates are much greater than required in order to permit sufficient latitude for parameter variation should such occasion be demanded.

(b) Grease is used in the gap. The diameter of the film is, consequently, easily varied to change the damping coefficient.

(c) The auxiliary spring rate was made approximately twice that of the main suspension system in the longitudinal direction. When the low-frequency damping factor is 0.65, the calculated cut-off frequency for the damper is 1.54 times higher than the natural frequency of the payload translational frequency in the longitudinal direction. The rate of roll-off of the damping coefficient with respect to frequency is 20 dB/decade.

In the actual design, the auxiliary spring for each damper consists of two steel beams, pin connected at both ends to an end ring of the cage structure.* The beams are made of 0.635 cm square tubings, with a wall thickness of 0.011 cm.

---

*See footnote on page 67.

Section 4
ACTIVE DAMPERS

4.1 APPROACH

Two electromagnetic actuators are used to provide adjustable damping for lateral rigid-body modes of the simulated payload. Each actuator system is located at the end of the 72-cm aluminum tube and can generate a force in any direction in a plane normal to the payload's longitudinal axis. The two actuator systems, therefore, can provide damping for two translational modes and for two rocking modes (e.g., pitch and yaw modes when they coincide with the principal coordinates of the system.).

Based on previous experiences, the feasibility to scale up the electromagnetic dampers for such applications as in a full-scale Space Shuttle vibration isolation system is practically non-existant because of its excessive weight, high power consumption, and limited force and stroke capabilities. For model-scale studies on isolation techniques and benefits, the above restrictions are not of major concern. The principal advantage of the electro-magnetic actuators lies in their versatility. Various control systems can be developed and used in conjunction with the actuators for further experimental investigations related to payload isolation technology.

4.2 DESCRIPTION

Each two-directional electromagnetic actuator (EMA) consists of the following major components: (a) a primary permanent field magnet (NTI DWG 20082),(b) A 4-coil armature plate (NTI DWG 20078),(c) A secondary permanent field magnet (NTI DWG. 20083),and (d) A sensor coil assembly (NTI DWG 20081). The assembled EMA is seen in NTI DWG 20094 and Figure 31.

4.3 PRINCIPLE OF OPERATION

The magnetic field between the parallel flat pole faces of the primary field magnet is approximately unformly distributed and has a distinct outline which is nearly the same as the pole faces themselves. The flux lines are normal to the pole faces and are approximately straight. The armature coils reside partially between the pole pieces. The boundary of appreciable magnetic field is indicated in Figure 9 on the armature coil assembly. The pair of coils a and c must be used in unison. When electrical currents of equal magnitude, I_{ac}, is passing through these two coils, equal and opposite forces are generated on the armature and on the magnet. The direction of the resultant force $\overline{F}_{ac}$, acting on the armature plate due to currents in coils a and c is shown in Figure 9. The magnitude of this force is proportional to the instantaneous magnitude of I_{ac}. Coils b and d are used in the same way, except the direction of the resultant force, $\overline{F}_{bd}$, generated by them is always perpendicular to $\overline{F}_{ac}$.

Consequently, both the magnitude and the direction of the resultant force $\overline{F}(= \overline{F}_{ac} + \overline{F}_{bd})$ can be controlled by controlling the magnitude, phase, and direction of currents I_{ac} and I_{bd}.

In order to use the EMA as an active damper, the force resultant must be controlled and made proportional to the relative velocity between the armature and the field magnet. This is accomplished with the help of the two-directional relative velocity sensor shown schematically in Figure 10. The secondary field magnet is rigidly attached to the primary magnet. The search coils are mounted on and move with the armature plate.

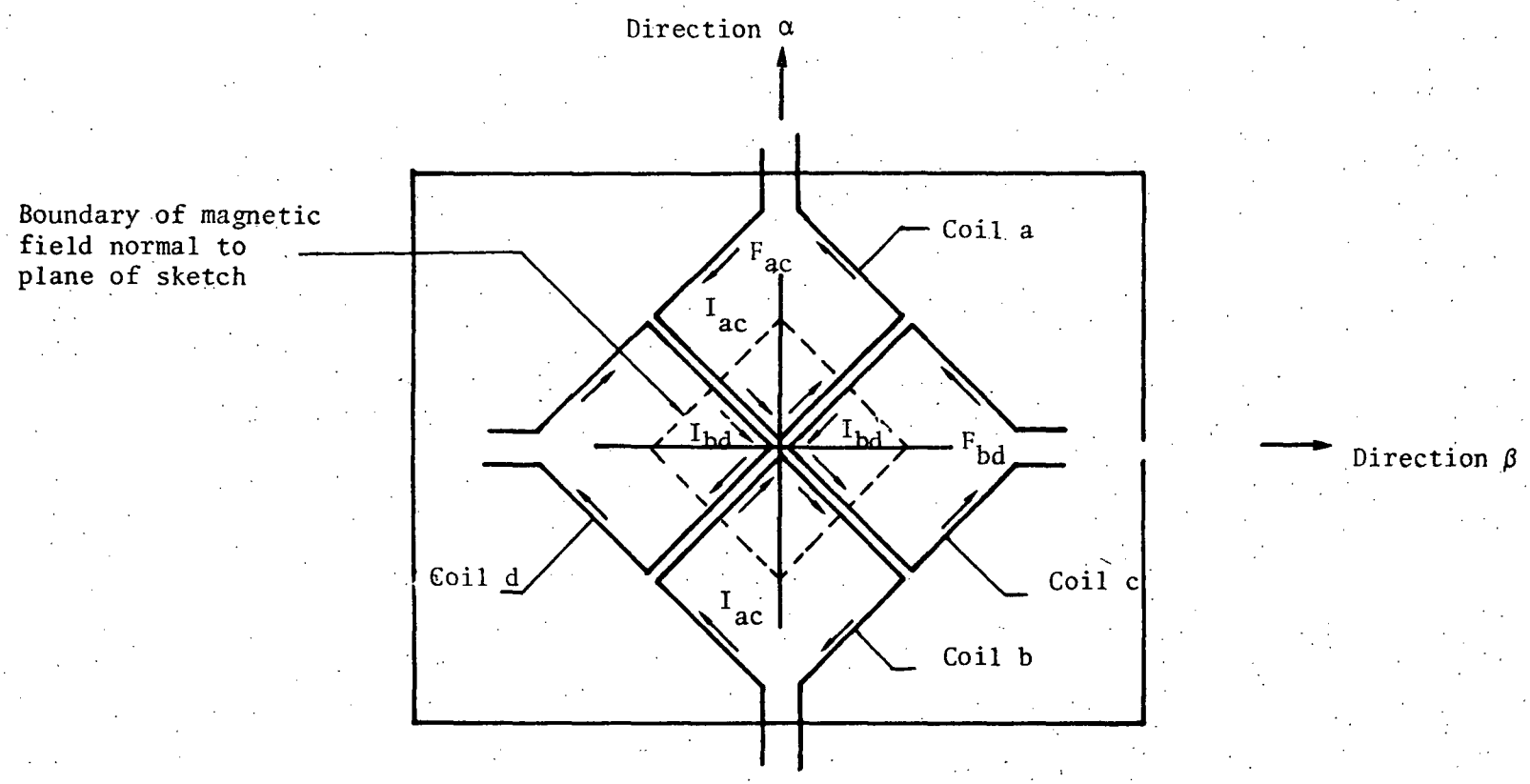

Figure 9 Principle of Operation of Electromagnetic Actuator

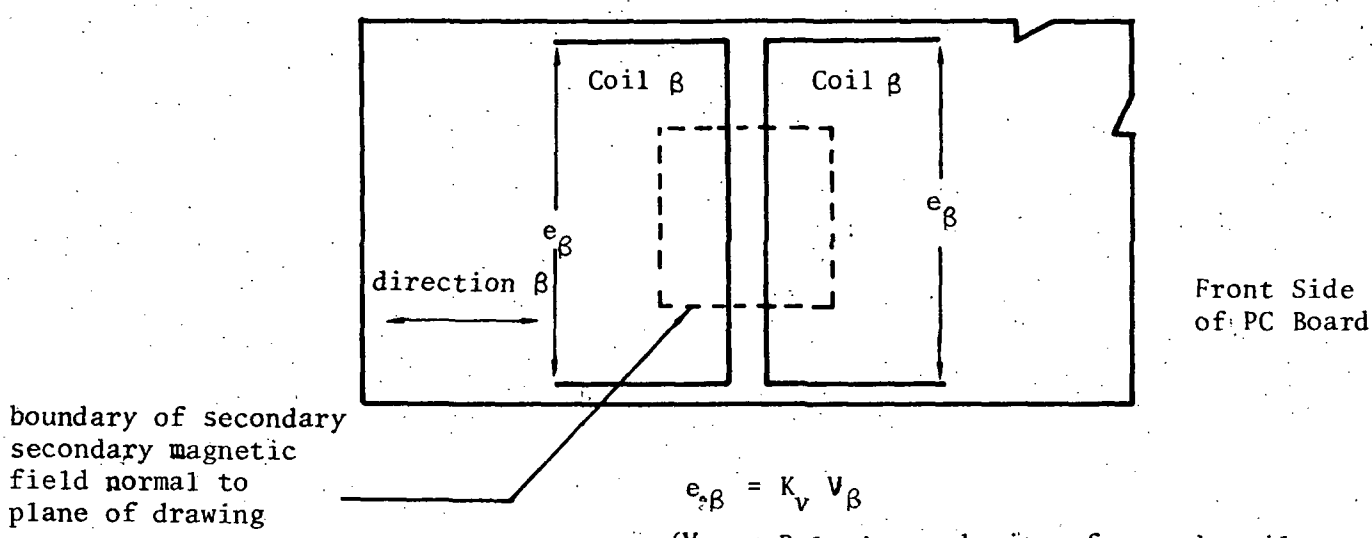

$e_\beta = K_v V_\beta$

(V_β = Relative velocity of search coils with respect to magnetic field in direction β).

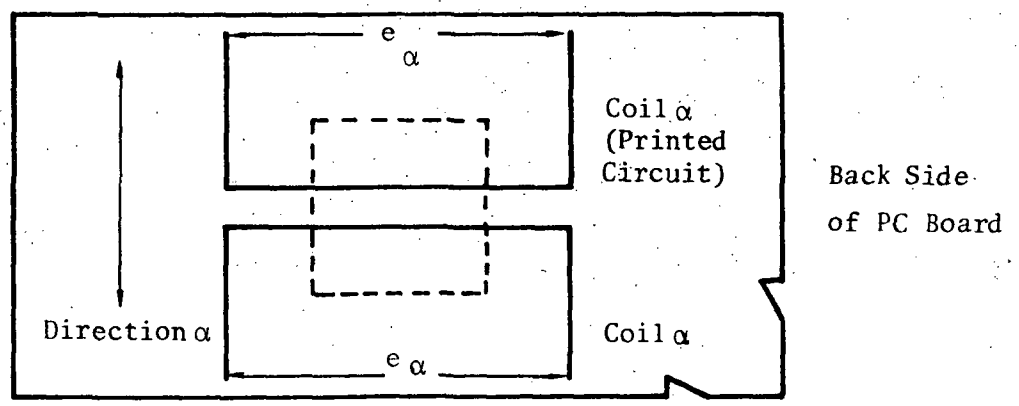

$e_\alpha = K_v V_\alpha$

(V_α = Relative velocity of search coils with respect to magnetic field in direction α).

Figure 10 Schematic Showing Principle of Operation of Relative Velocity Sensor

It acts as a dc generator. The open-circuit output voltage is proportional to the relative velocity between the secondary field magnet and the search coil. The design arrangement is such that the output of the search coil, α, is proportional to the instantaneous relative velocity component in the direction α in Figure 9. The operation of search coil β and the armature coils b and d is similar. The combination of the actuator and the velocity sensor makes it possible to generate damping forces in any direction in the plane of the armature plate.

4.4 STABILITY ANALYSIS

If the payload and the vehicle are really rigid bodies, and if all electronic components and the EMA have flat frequency responses and zero phase lag, the system (the damper, the controls, and the structure) is inherently stable. In actuality, instability can occur in nearly all practical systems since the above requirements are usually not easily satisfied for a sufficiently wide band of frequencies. In the following stability analysis, both the rigid-body assumption of the payload and the vehicle, and the frequency-independence assumption of the transfer function of the electronics are removed. It will be shown that with care, the system design can be made stable for most practical requirements.

Let i = 1, 2, ...= mode index;

ω_i = undamped angular natural frequency;

m_i = generalized mass;

$F_i(t)$ = generalized force;

ζ_i = modal damping (parasitic structural damping);

Furthermore, let the subscript

a identify the position of the EMA magnet;

b, the EMA armature;

α, the velocity sensor magnet;

β, the velocity pickup coil;

and let

$V_a(t)\ \tilde{n}_a$ = velocity vector of the actuator magnet, ($\tilde{n}_a$ being a unit vector);

$V_b(t)\ \tilde{n}_b$ = velocity vector of the actuator armature;

$V_\alpha(t)\ \tilde{n}_\alpha$ = velocity vector of the sensor magnet;

$V_\beta(t)\ \tilde{n}_\beta$ = velocity vector of the pick-up coil;

$F_a(t)\ \tilde{m}_a$ = damping force applied on the actuator magnet, ($\tilde{m}_a$ being a unit vector);

and $F_a(t)\ \tilde{m}_b$ = damping force applied on the actuator armature.

An external force, $F_e(t)\ \tilde{m}_e$, applied to the point identified by the subscript e on the vehicle is included to identify the input port of the closed-loop system, which is shown in block-diagram in Figure 11.

The mode shapes at points a, b, α, β, and e are the vectors $\phi_{ia}\ \tilde{n}_{ia}$, $\phi_{ib}\ \tilde{n}_{ib}$, $\phi_{i\alpha}\ \tilde{n}_{i\alpha}$, $\phi_{i\beta}\ \tilde{n}_{i\beta}$ and $\phi_{ie}\ \tilde{n}_{ie}$, respectively, where $\tilde{n}_{ia}$, $\tilde{n}_{ib}$, $\tilde{n}_{i\alpha}$, $\tilde{n}_{i\beta}$ are unit vectors. Shorthand notations:

$$v_\alpha \equiv v_\alpha(s) \equiv L\{V_\alpha(t)\};$$

$$v_\beta \equiv v_\beta(s) \equiv L\{V_\beta(t)\};$$

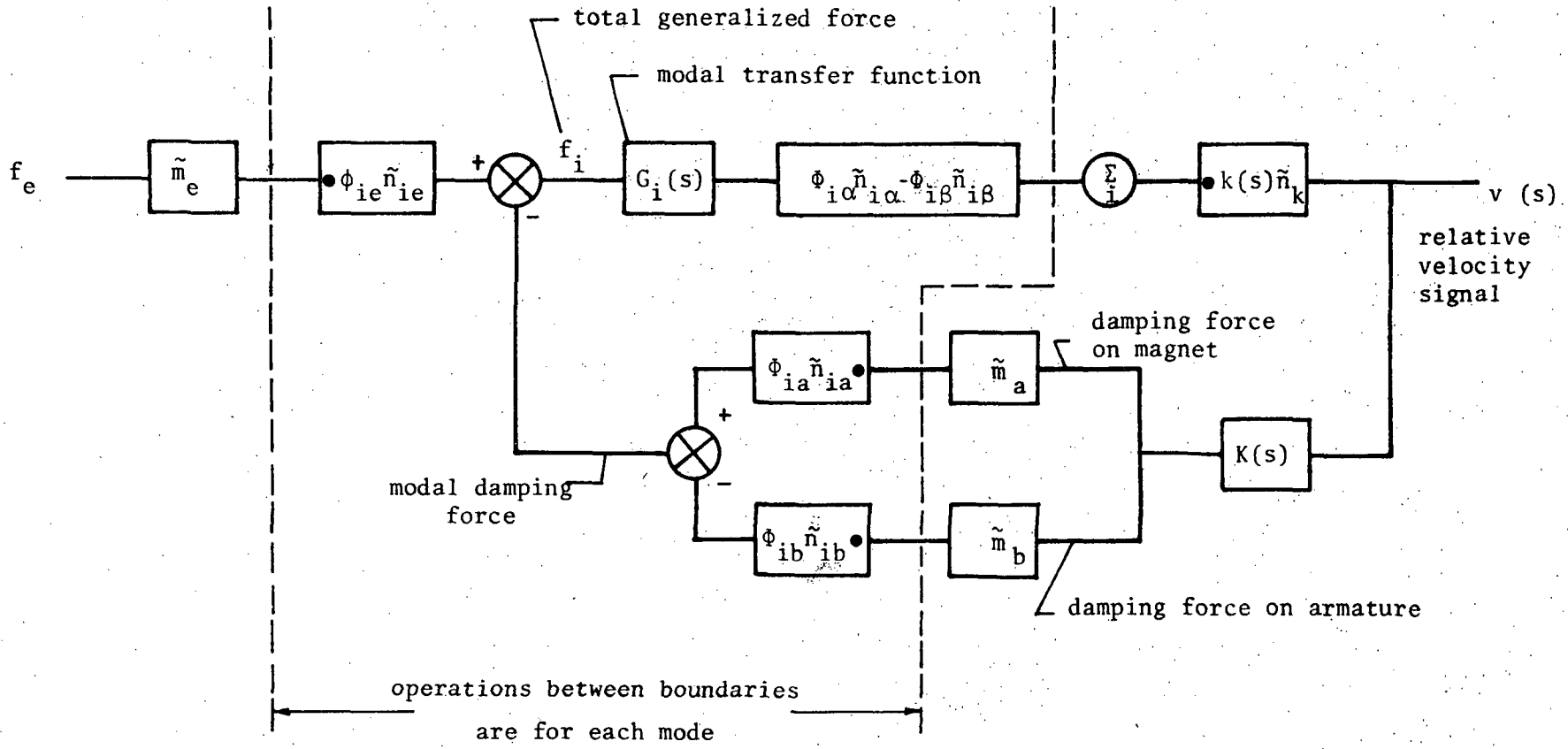

Notes: $\tilde{m}_e$, $\tilde{m}_a$, ...$\tilde{n}_{ie}$, $\tilde{n}_{ia}$, ... are unit vectors

$$G_i(s) = s/[m_i(s^2+2\zeta_i\omega_i s+\omega_i^2)]$$

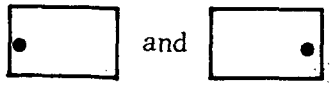

and denote dot products of vectors

Figure 11 Block Diagram of Closed-Loop System for Damper Stability Analysis

$$f_a \equiv f_a(s) \equiv L\{F_a(t)\};$$

$$f_b \equiv f_b(s) \equiv L\{F_b(t)\};$$

$$f_e \equiv f_e(s) \equiv L\{F_e(t)\};$$

$$f_i \equiv f_i(s) \equiv L\{F_i(t)\};$$

are used in Figure 11 and in subsequent discussions.

System imperfections which should be kept in mind are (a) a real relative velocity sensor has non-zero gage lengths, and, hence, is subject to misalignment. In other words, the unit vectors $\tilde{n}_\alpha$ and $\tilde{n}_\beta$ are not always the exact opposite of each other, and (b) the transducer can only pick up two components of the relative velocity vector instead of all three. The transducer transfer function is specified by its frequency response function k(s) and a unit vector $\tilde{n}_k$ indicating the direction of its axis of sensitivity. The output of the transducer is

$$v(s) = k(s)\, \tilde{n}_k \cdot (v_\alpha \tilde{n}_\alpha - v_\beta \tilde{n}_\beta). \tag{20}$$

The structure is characterized by transfer functions in the generalized coordinates

$$G_i(s) = s/[m_i(s^2 + 2\,\zeta_i\omega_i s + \omega_i{}^2)]. \tag{21}$$

The control system and the actuator transfer functions are combined and denoted by K(s) in Figure 11. Let

$$\tilde{m}_a \cdot \tilde{n}_{ia} = A_i ; \tag{22}$$

$$\tilde{m}_b \cdot \tilde{n}_{ib} = B_i ; \tag{23}$$

$$\tilde{n}_k \cdot \tilde{n}_{i\alpha} = A_i' ; \tag{24}$$

$$\tilde{n}_k \cdot \tilde{n}_{i\beta} = B_i' ; \tag{25}$$

$$\tilde{m}_e \cdot \tilde{n}_{ie} = E_i . \tag{26}$$

The closed-loop transfer function between the transducer output, v(s) and the external force input, $f_e(s)$, can now be derived from Equation (20) and Figure 11:

$$v = k\,\tilde{n}_k \cdot (v_\alpha \tilde{n}_\alpha - v_\beta \tilde{n}_\beta)$$

$$= k \sum_i [(f_e \tilde{m}_e)\cdot(\phi_{ie}\tilde{n}_{ie})][(\phi_{i\alpha}\tilde{n}_{i\alpha} - \phi_{i\beta}\tilde{n}_{i\beta})\cdot\tilde{n}_k]\, G_i$$

$$-kKv \sum_i [\tilde{m}_a \cdot (\phi_{ia}\tilde{n}_{ia})][(\phi_{i\alpha}\tilde{n}_{i\alpha} - \phi_{i\beta}\tilde{n}_{i\beta})\cdot\tilde{n}_k]\, G_i$$

$$+kKv \sum_i [\tilde{m}_b \cdot (\phi_{ib}\tilde{n}_{ib})][(\phi_{i\alpha}\tilde{n}_{i\alpha} - \phi_{i\beta}\tilde{n}_{i\beta})\cdot\tilde{n}_k]\, G_i$$

Substituting Equations (22) to (26) into the last equation and re-arranging terms, the following transfer function for the closed loop is derived

$$\frac{v(s)}{f_e(s)} = \frac{k(s) \sum_i E_i\phi_{ie} (A_i'\phi_{i\alpha} - B_i'\phi_{i\beta}) G_i(s)}{1+k(s)K(s)\sum_i (A_i\phi_{ia} - B_i\phi_{ib})(A_i'\phi_{i\alpha} - B_i'\phi_{i\beta}) G_i(s)} \quad . \tag{27}$$

The following stability criteria of the system may be derived by investigating the behavior of the open-loop gain

$$H(s) = k(s) K(s) \sum_i (A_i\phi_{ib} - B_i\phi_{ib})(A_i'\phi_{i\alpha} - B_i'\phi_{i\beta}) G_i(s) \tag{28}$$

in the standard-form transfer function of Equation (27):

(a) For an ideal system, the transfer function of the transducer, the control system and the actuator are real constants, (i.e., $k(s)K(s) = K>0$); the sensor magnet and the primary magnet are together (i.e., $a = \alpha$, $\phi_{ia} = \phi_{i\alpha}$, $\tilde{m}_a = \tilde{m}_\alpha$ and $\tilde{n}_{ia} = \tilde{n}_{i\alpha}$) so that $A_i = A_i'$; and the sensor coils and the actuator armature coils are together (i.e., $b = \beta$, $\phi_{ib} = \phi_{i\beta}$, $\tilde{m}_b = \tilde{m}_\beta$ and $\tilde{n}_{ib} = \tilde{n}_{i\beta}$) so that $B_i = B_i'$. Under these conditions, Equation (28) is reduced to

$$H(s) = kKs \sum_i (A_i\phi_{ia} - B_i\phi_{ib})^2/[m_i(s^2+2\zeta_i\omega_i s+\omega_i^2)] \tag{29}$$

The gain-vs.-phase plot of the open-loop transfer function of Equation (29) is shown in Figure 12, which indicates a minimum of $\pm 90°$ phase margin for all values of K due to the fact that term $(A_i\phi_{ia} - B_i\phi_{ib})^2$ is always positive. This ideal system is, therefore, stable for all values of gain even though the structure has infinitely many elastic modes.

The effect of relative velocity feedback may be observed near any natural frequency ω_I. The ideal transfer function is then approximately

$$\frac{v(s)}{f_e(s)} = \frac{k\, E_I\phi_{Ie}(A_I\phi_{Ia} - B_I\phi_{Ib})}{m_I[s^2 + (2\zeta_I\omega_I + K/m_I)\, s + \omega_I^2]} \tag{30}$$

which is the same as the modal transfer function of the structure alone, except for the extra term Ks in the denominator. Linear, viscous modal damping is, therefore, added to the I^{th} mode. Since I is arbitrary, it may be concluded that damping is added to all modes.

(b) In a real situation, it is impossible to have the actuator and the velocity sensor occupy the same location, so that there is bound to be some differences between a and α, b and β, ϕ_{ia} and $\phi_{i\alpha}$, ϕ_{ib} and $\phi_{i\beta}$, $\tilde{n}_{ia}$ and $\tilde{n}_{i\alpha}$, $\tilde{n}_{ib}$ and $\tilde{n}_{i\beta}$. Normally, the differences are small for low-frequencies if the sensor and the actuator are reasonably close to each other.

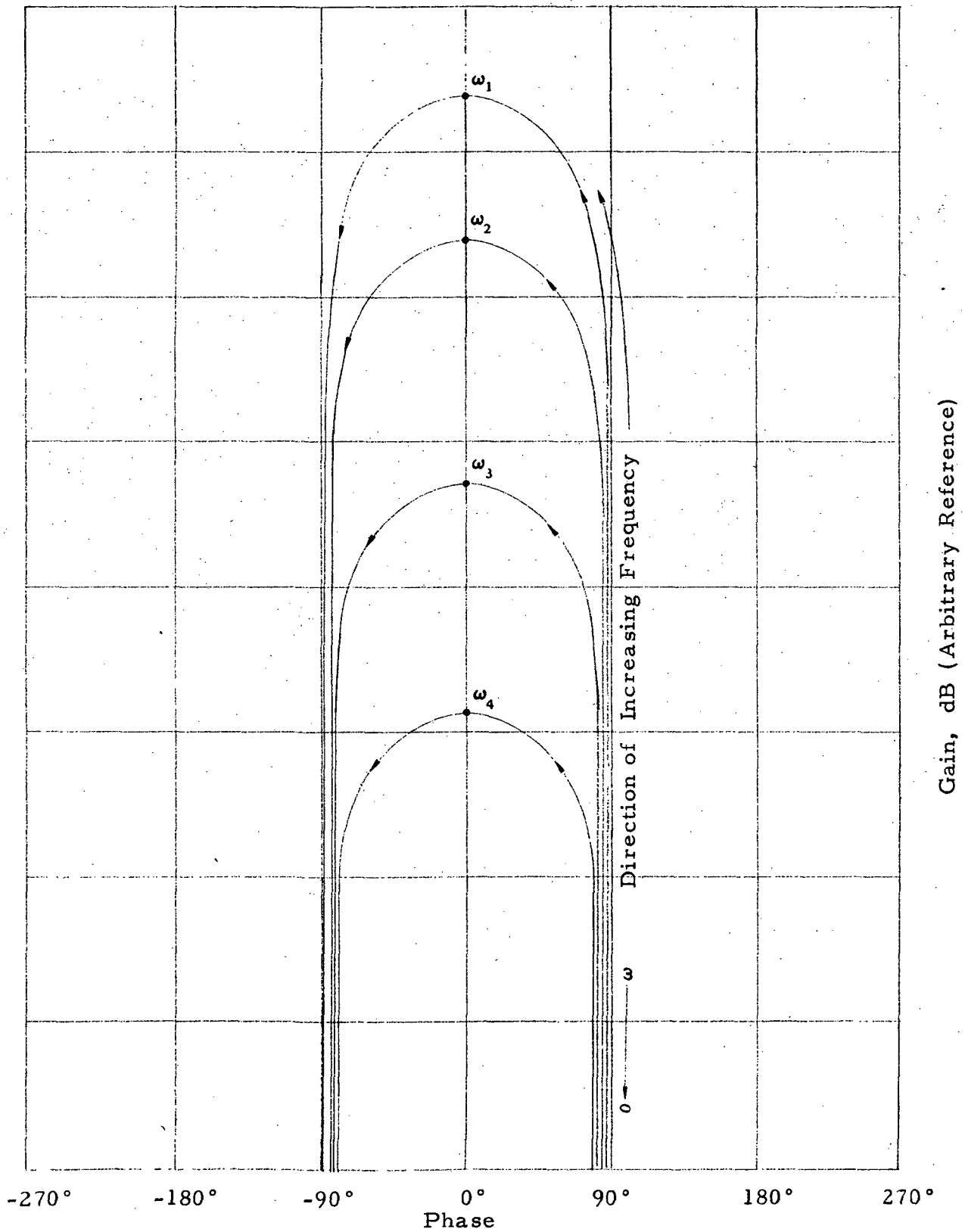

Figure 4 Ideal Open-Loop Gain vs. Phase Plot

For low frequencies, then, the products $(A_i\phi_{ia} - B_i\phi_{ib})(A'_i\phi_{i\alpha} - B'_i\phi_{i\beta})$ are positive and positive damping are added to the low-frequency modes covered by this condition. At high frequencies, some of the mode shapes will have an odd number of node points between the sensor and the acutator. The above product will be negative for these modes and negative damping will be introduced. As the gain is increased, this negative damping will eventually overcome inherent structural damping in one of these modes and diverging oscillation in that mode, at its natural frequency, will occur.

(c) If the feedback signal is obtained by integration of an accelerometer signal from the payload, the open-loop transfer function would have the form

$$H(s) = k(s)\, K(s) \sum_i (A_i\phi_{ia} - B_i\phi_{ib})\, A'_i\phi_{i_\alpha}\, G_i. \qquad (31)$$

Unlike with relative velocity feedback, the factor $(A_i\phi_{ia} - B_i\phi_{ib})\, A'_{ib}\phi_{i\alpha}$ can be either positive or negative for the various modes, depending on the mode shapes. Instability can occur for the same reason described in (b) above.

(d) It is desirable to use wideband transducers, signal conditioning equipment, power amplifiers and actuators so that the factor k(s) K(s) does not introduce significant phase shift in H(s).

4.5 DESIGN CALCULATIONS

4.5.1 Field Magnets

Based on approximate weight, size, force and stroke requirements for dampers, preliminary designs of the primary magnet for the actuator and of the secondary magnet for the relative velocity transducer were accomplished. Indications were that the following design objectives can be met:

(a) Primary Magnet (Actuator)

Pole Dimensions: 3.55 cm x 3.55 cm

Magnetic Gap: 0.838 cm *

Flux Density in Gap: 10^4 gausses

Approximate Mass: 8 kg

Maximum Envelop Dimension: 20 cm

(b) Secondary Magnet (velocity sensor)

Pole Dimensions: 2.54 cm x 2.54 cm

Magnetic Gap: 0.508 cm *

Flux Density in Gap: 5×10^3 gausses

Final magnet designs satisfying these requirements were firmly established by Indiana General Magnetic Products Division of Electronic Memories & Magnetics Corporation, Valparaiso, Indiana, who also cast, ground, assembled, magnetized and stabilized two complete Alnico 5 magnet assemblies. NTI DWGS. 20082 and 20083 show final magnetic design details, and 20084 shows the assembly.

---

*Gap dimensions were governed by the minimum coil thicknesses and clearance requirements.

4.5.2 Actuator Coil

Each of the four actuator coils in one armature plate contains 400 turns of No. 28 magnet wire*.

The average effective length of each turn of the coil in the magnetic field is 2.70 cm. The force generated by this length of wire carrying I amperes in the 10^4-gauss field is .027xI N. The total force generated by the 800 turns of coil in each pair of coils is 21.6xI N.

The maximum force capability of the actuator is limited by the heat dissipating capability of the entire assembly at the maximum allowable temperature of one of its components. In this particular design, this limit is the breakdown temperature of the magnet wire insulation which is 220°C. The rate of heat generation is calculated as follows: At room temperature, the resistance of each of the four coils is 7 ohms. This is increased by 79% to 12.5 ohms when the coil temperature reaches the allowed maximum of 220°C. If the steady-state current which maintains this temperature is I_m amperes, rms, the heat generated by the four coils will be 50 I_m^2 watts. Conversely, if the armature assembly can dissipate D watts of heat at 220°C, equilibrium will be reached at $I_m = 0.141\ D^{1/2}$ amperes, rms. The corresponding resultant force generated by I_m is

$$f_{max} = 0.707 \times 21.6 \times 0.141\ D^{1/2} = 2.2D^{1/2}\ N, \text{ rms.} \qquad (32)$$

---

*Heavy Armored Poly-Thermaleze insulation (Belden)

4.5.3 Velocity Transducer Sensitivity

Each sensing coil of the relative velocity transducer contains 40 turns; the magnetic field is 5×10^3 gausses; and the active length of each turn is 2.54 cm, the transducer sensitivity is

$$40 \times 5 \times 10^3 \times 2.54 \times 10^{-8} \text{ volts/(cm/sec)}$$

or approximately 5.1 mv/(cm/sec).

4.5.4 Control System Gain

The required damping coefficient to attain a modal damping factor of 0.65 was determined in Section 3.1 to be

$$C = 15 \text{ N/(cm/sec)}$$

Two coils are used in parallel to develop the damping force in each direction. The parallel resistance of these two coils at room temperature is

$$R = 3.5 \text{ ohms.}$$

The current-to-force conversion factor of two coils is, according to design calculations,

$$K_c = 21.6 \text{ N/amp.}$$

The velocity transducer sensitivity is

$$k = 0.0051 \text{ v/(cm/sec)}$$

The voltage gain, K_v, of the damper control amplifier is given in terms of the above parameters by the expression

$$K_v = RC_i/k\ K_c = 476\ v/v \tag{33}$$

at room temperature. The upper limit on the required gain is, when the actuator coil temperature is at 220° C,

$$\max K_v = 476 \times 1.79 = 852\ v/v \tag{34}$$

4.6 COIL FABRICATION DETAILS

The fabrication of both the actuator coils and the velocity sensor coils was quite tedious. A number of techniques were developed during the project and are described in this report as permanent documentation.

4.6.1 Armature Coil

Each armature coil was hand wound. The setup is shown in Figure 13. Coil form details and assembly are shown in NTI DWG. 20079. Four complete assemblies were used. As shown in Figure 13, a constant wire tension of approximately 0.445 N was maintained during winding. The magnitude of this tension was optimized via a number of trial windings. On the one hand, this force appeared to be the minimum required to yield a proper wire packing density; on the other hand, higher forces (say at twice the tension) actually stretched wires permanently. The tensions were maintained in the wire after the winding process until the coil was potted in epoxy.

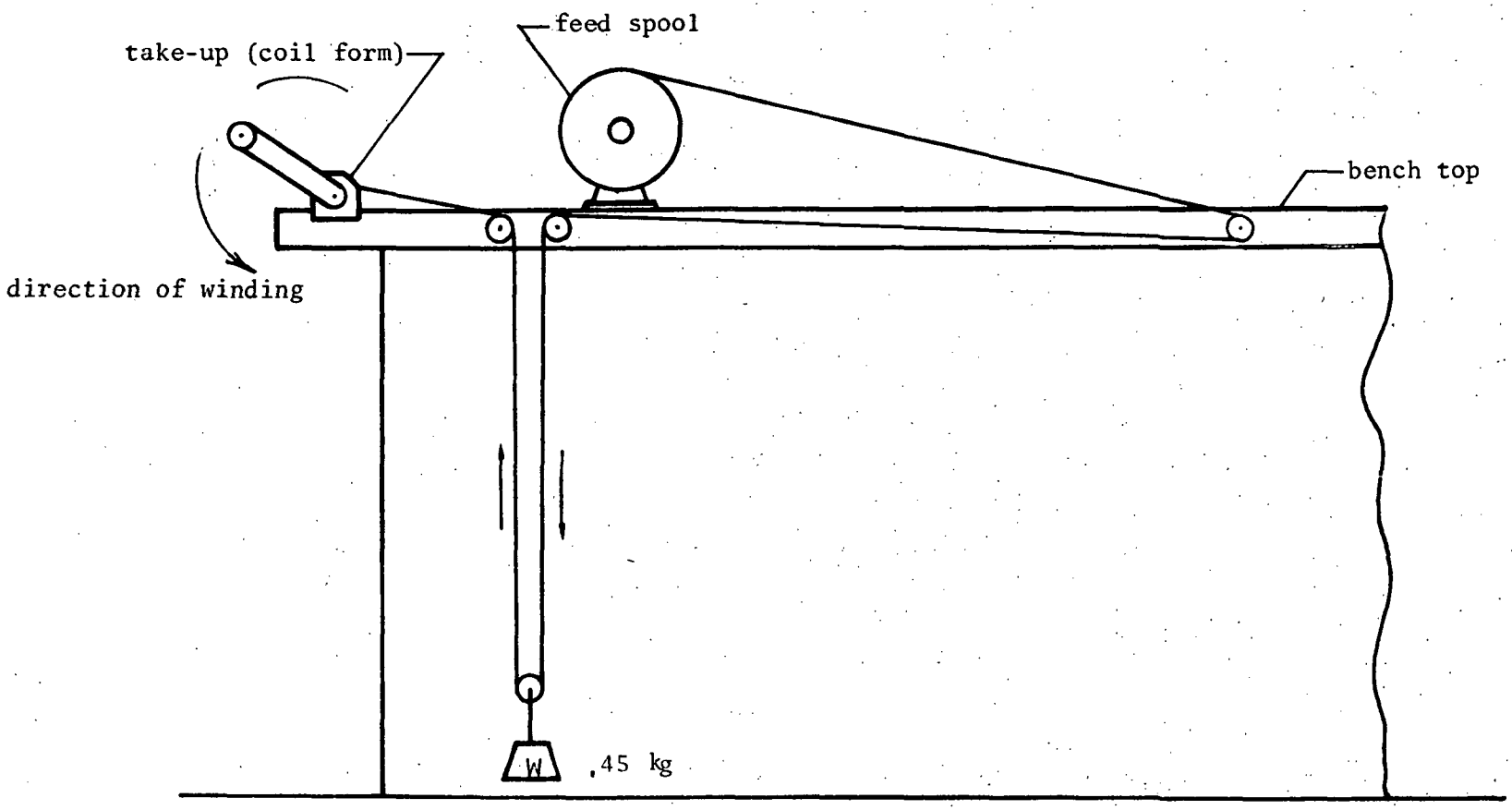

Figure 13 Coil Winding Setup

The coil and the forms were vacuum-impregnated in an impregnating epoxy resin (Eccoseal 1207,manufactured by Emerson & Cuming, Inc., Dielectric Materials Division, Canton, Mass.) the following procedure was followed:

(a) The coils were cleaned with alcohol.

(b) The exterior surfaces of the coil forms were coated with a releasing compound (silicon grease).The interior sufaces of the coil forms were pre-coated with the releasing compound.

(c) Sufficient Eccoseal 1207 was mixed with its hardner, and heated to 65° C. Air was removed by applying a vacuum of approximately 2.5 inches of water.

(d) The four coils, together with their molds, were completely immersed in the warm Eccoseal 1207.

(e) A partial vacuum of approximately 2.5 inches of water was applied and held for 30 minutes.

(f) The vacuum was released and the resin was forced into the coils by atmospheric pressure.(30 minutes)

(g) The coils were drained and cured at 120°C for four hours, followed by 2 hours at 176°C.

(h) After cooling, the molds were disassembled and the coils were thoroughly cleaned in alcohol for potting in the carrier plate.

4.6.2 Armature Coil Assembly

Four impregnated armature coils were potted in each carrier plate (NTI DWG 20077). The assembled armature is shown in NTI DWG 20078. The following procedures were used:

(a) Lead wires were soldered to the terminal screws.

(b) The terminal assembly and the lead wires were potted in the carrier plate with Stycast 1209 (manufactured by Emerson & Cuming, Inc.)

(c) The four coils were clamped in place in the carrier and, using a minimum amount of stycast 1209, the coils were tached to the carrier plate. Curing was promoted by heating to 100°C.

(d) After cooling, the leads were soldered to the coils.

(e) Both the carrier assembly and the prepared Stycast mixture were heated to 65°C, and the mixture was poured into the cavity between the clamping plate and the carrier, with sufficient excess to cover all air passages.

(f) The assembly was placed in a vacuum jar and air was evacuated (to 2.5 inches of water, and held for 30 minutes)

(g) The vacuum was released and the epoxy was allowed to fill the voids between the carrier and the clamping plate. (30 minutes)

(h) Excess epoxy was wiped off.

(i) Curing was carried out at 100°C for 4 hours, followed by 150°C for 1 hour and 175°C for 12 hours.

4.6.3 Velocity Transducer Coils

The velocity transducer search coils were fabricated from three identical double-sided p.c. boards. Etched on each side of each board are 20 turns of sensing coil. Standard p.c. board technology was used to fabricate these search coils. The turns on the two sides of the board

sense velocity in perpendicular (90°) directions. Figure 14 shows photographs of the two sides of the p.c. board. Note also the soldering pads for lead and jumper wires. Three such cards were stacked and epoxy bonded to form a plate 0.21 cm thick. The coils sensitive to velocities in like directions were soldered in series to form an effective sensing coil of 60 turns.*

Eccoseal 1207 was used to bond the p.c. boards. Vacuum impregnation procedures described in Section 4.6.1 were used. Teflon jacketed lead wires were soldered to the coils and an additional potting was used to prtect the soldered joints. The other ends of these leads were soldered to a terminal board which is potted in a separate step to one of the coil plate support blocks (NTI DWG 20081).

4.7 DAMPER ASSEMBLY

The damper magnet assemblies are mounted on the ends of the 72-cm aluminum tubing with an aluminum adapter plate (NTI DWGS 20086 and 20092). After the payload simulator package is properly suspended in the Cage Structure, the armature plate is inserted through the gap of the primary magnet and attached to the Cage Structure posts, using four steel cables (NTI DWG 20091, Sheet 3). The velocity sensor coil assembly and its support blocks are mounted onto the armature plate at this time. The two coil systems are kept in the middle of the their respective magnetic gaps by adjusting the tensions in the steel cables and the flexible support rods. (NTI DWG 20086).

---

*Of the four completed sensing coil assemblies, only one survived the potting process intact. The other three had to be repaired, and only 40 turns were salvaged for each coil. Compensation for the reduced number of turns was made in the damper control amplifiers.

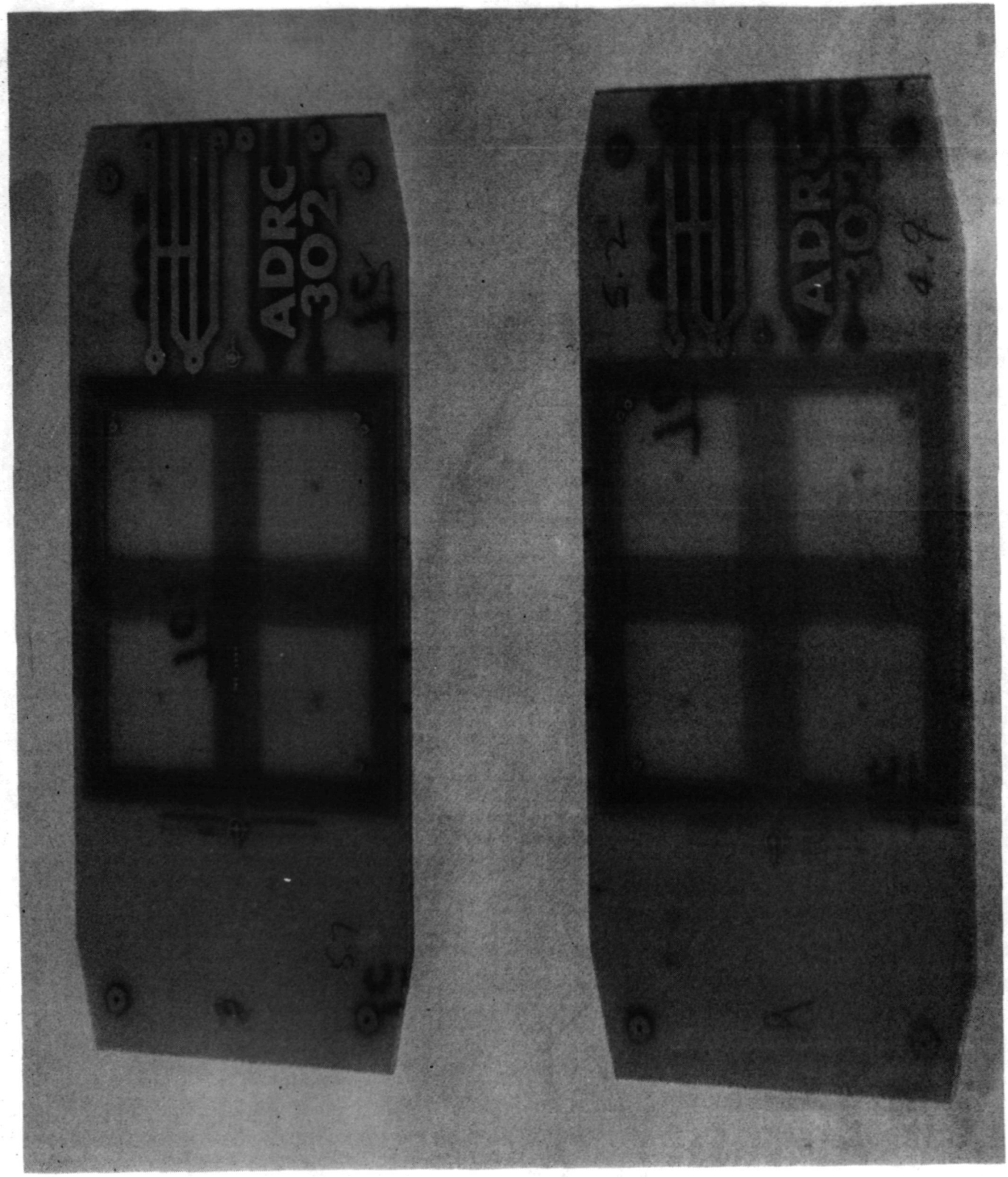

Figure 14 Velocity Sensing Coils on P.C. Card

4.8 DAMPER CONTROL SYSTEM

Four independent control channels are required to operate the EMA. Figure 15 is a schematic of the control electronics.

An RCA HC2000H Power Op Amp is used to drive the EMA. With supply power regulated by two Powertec Model DCR 1B24-4.5 Power Regulators,* the HC2000H is capable of delivering 4.5 amps at ±18.5 volts.

The HC2000H is connected as an non-inverting amplifier with a gain of 3.9, which is established by the internal feedback resistor of 18.2 kΩ from Pin 2 to Pin 9 of the HC2000H and an external 6.2 kΩ resistor from Pin 9 to Common. At this gain, the bandwidth is approximately 10 kHz.

The zero-offset drift of the power amplifier is controlled by the Datel Model 200 C Instrumentation Amplifier. This instrumentation amplifier is used mainly to provide the voltage gain for the relative velocity signal required by damping specifications. However, when the output terminal of the HC2000H is connected to the Sense terminal of the 200C, the former becomes a current booster only. The overall voltage drift is reduced to that of the 200C, 1μv/°C, RTI. The overall gain is controlled by the Gain Adjust potentiometers on the front panel, and is variable from 2 to 1000 The frequency response of the composite amplifier is shown in Figure 18. The Reference Terminal of the 200C is also used. In this case, it provides a convenient means of introducing an adjustable drive signal from an external source. Consequently, the EMA can be used both as a damper and as a shaker, simultaneously, in checkout tests.

A second Datel 200C is included in each channel of electronics to amplify and buffer the relative velocity signal from the main control stream,

* Power Supply Schematics are shown in Figures 16 & 17.

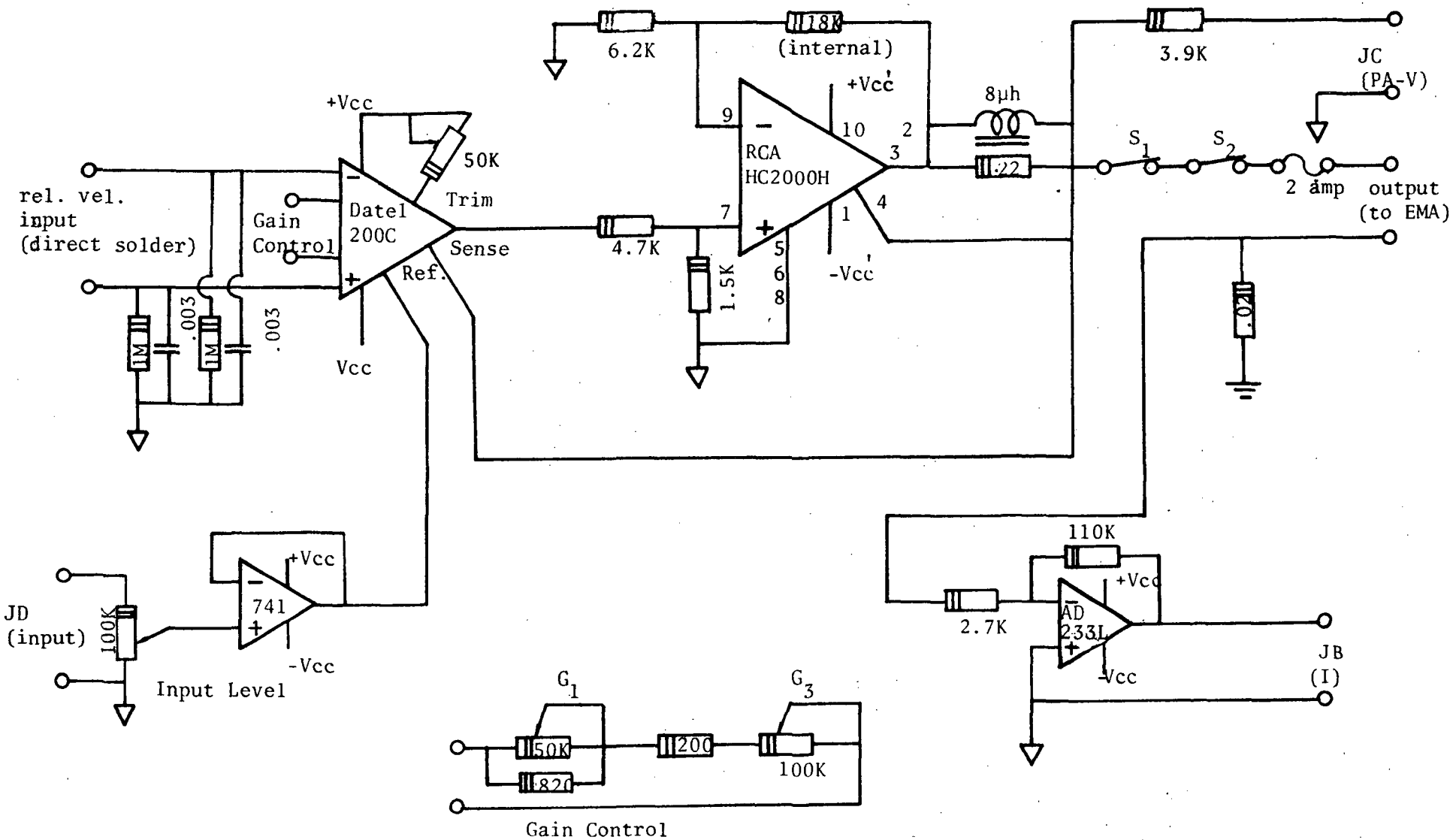

Figure 15 Damper Control Schematics

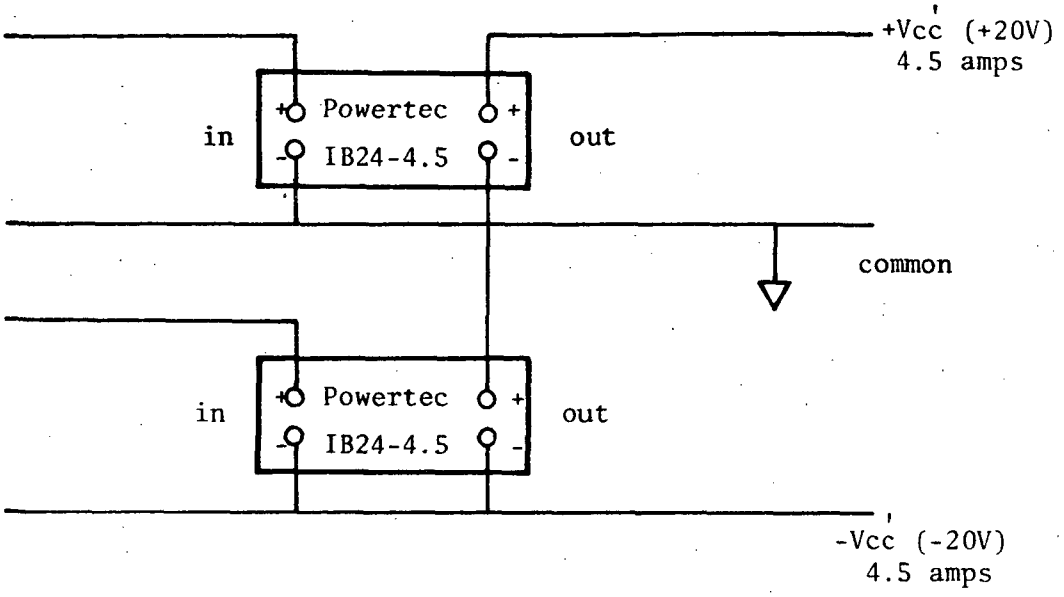

Figure 16. Power Supply Voltage Regulator for Power Amplifier

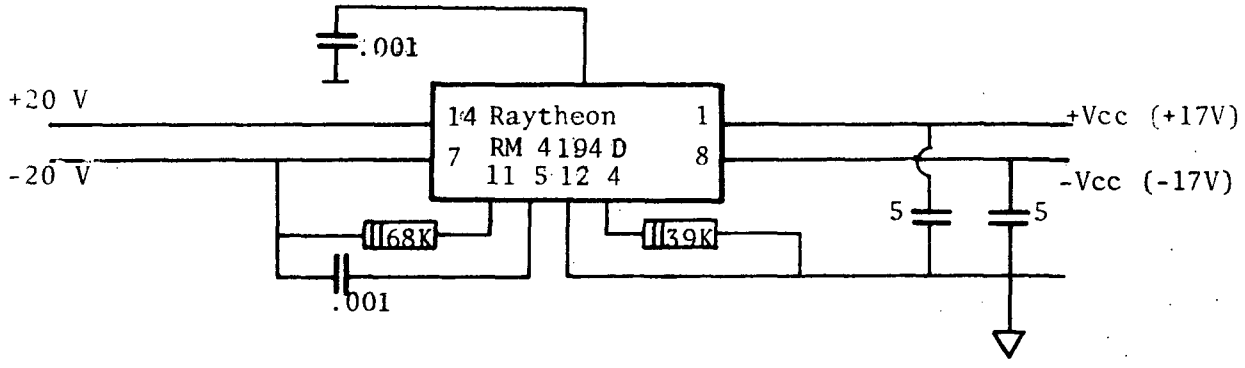

Figure 17 Power Supply Voltage Regulator for Instrumentation Amplifiers

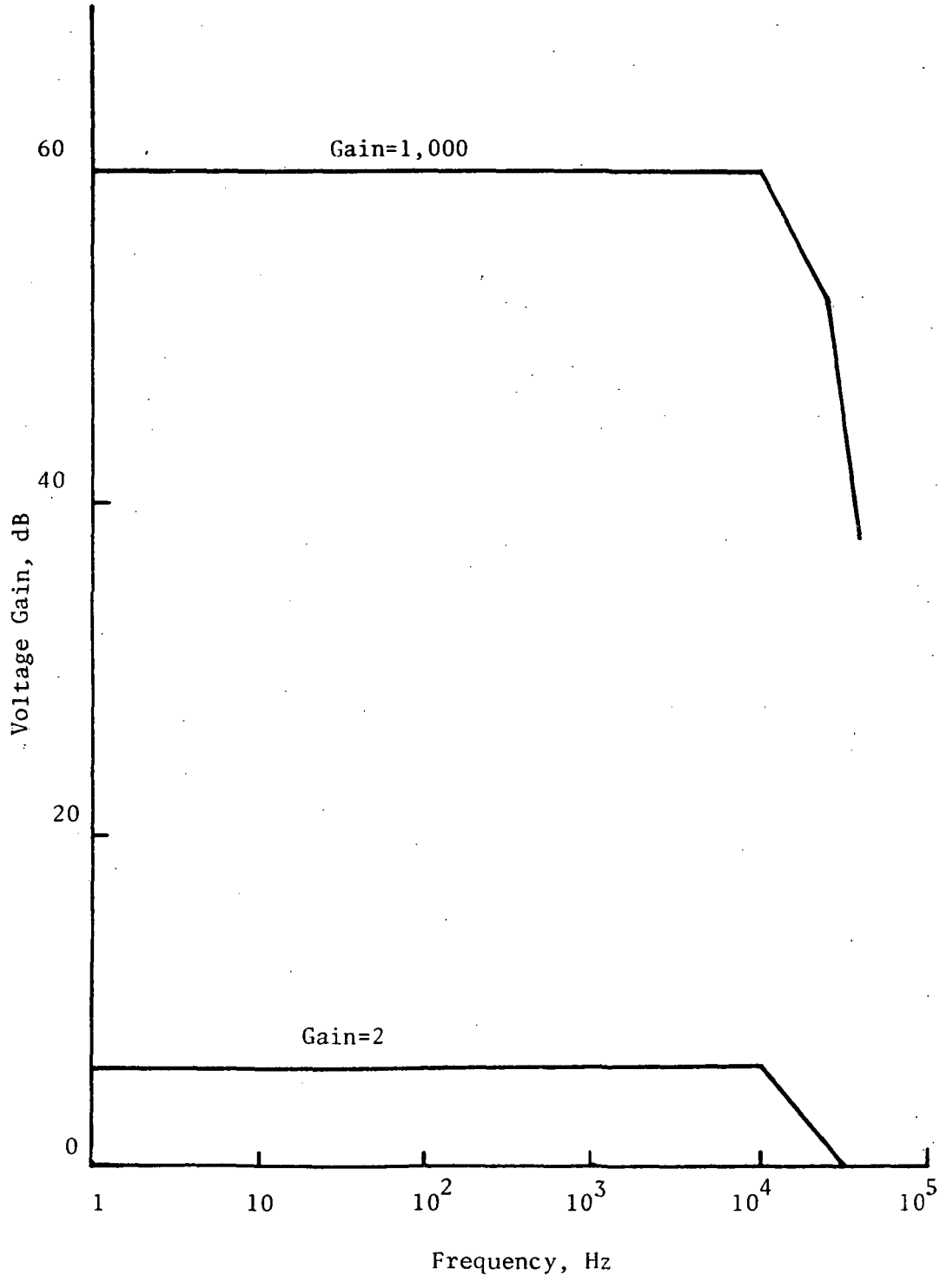

Figure 18 Frequency Response Curves for Composite Amplifiers

An Analog Devices Model 233L Chopper Stabilized Op Amp is also included in the system. As implemented, it amplifies and buffers the output of a 0.02-ohm current-sensing resistor between the actuator coil and power supply common, for current monitoring purposes. However, the main purpose of including this low-drift (0.1μv/°C) op. amp is to provide circuit flexibility for potential future system modifications.

Schematics of the circuit around the second Datel amplifier and the 233L are shown in Figure 20.

Schematics of circuits around the second Datel amplifier are shown in Figure 19; and schematics of circuits around the Analog series' 2336 are shown in Figure 20.

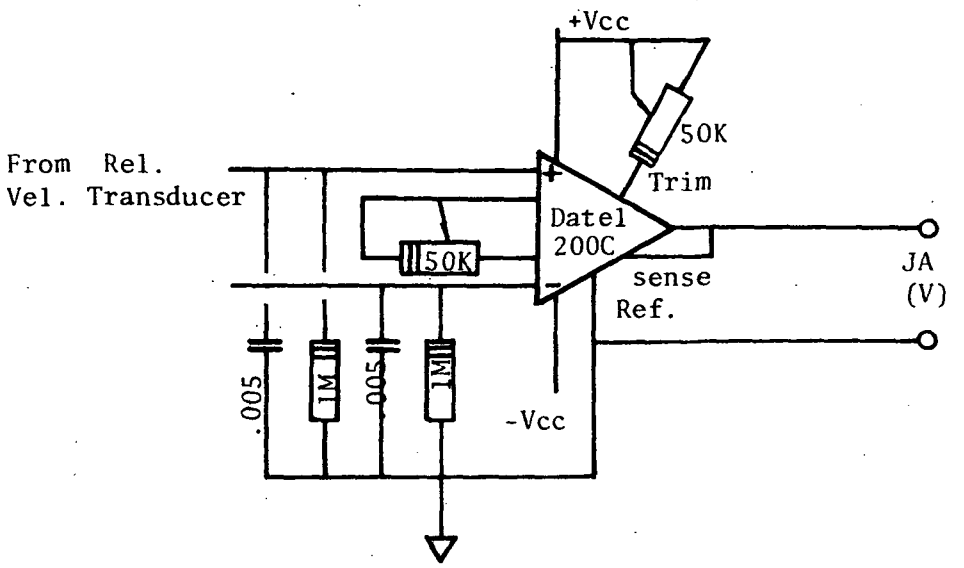

Figure 19. Buffer Amplifier for Relative Velocity Monitoring

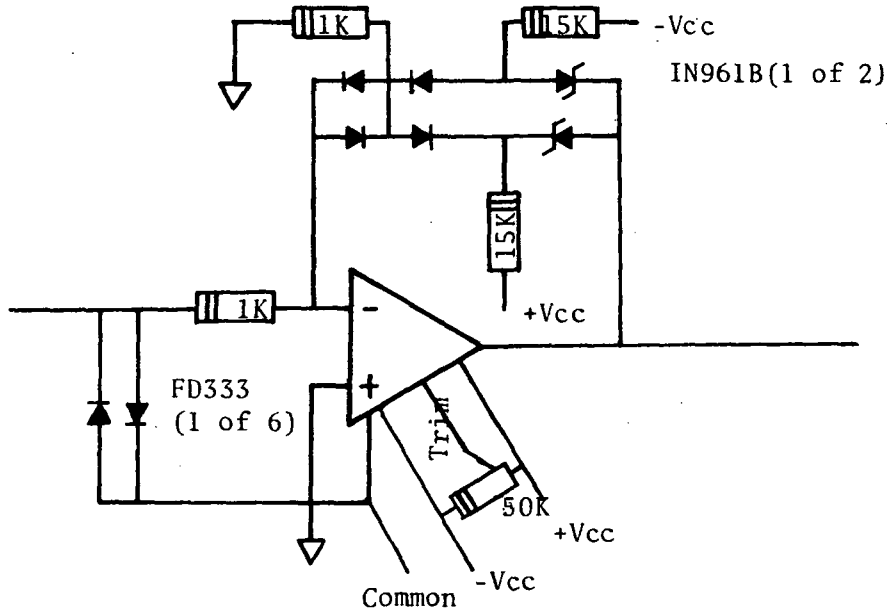

Figure 20 Over-Voltage and Latch-up Protection Circuits for Analog Devices 233L Op Amp

Section 5

HARDWARE

5.1 MANUFACTURERS

Four separate phases of fabrication were involved during this project:

(a) Permanent Magnet Assemblies, by Indiana General, Magnetic Products Division of Electronic Memories and Magnetics Corporation Valparaiso, Indiana;

(b) Mechanical Components, by General Products, Inc., Huntsville, Alabama;

(c) Coils, by NTI;

(d) Electronics, by NTI.

In addition, the suspension cables were assembled and proof tested by Sling Center, Inc., of Brighton, Alabama.

5.2 PHOTOGRAPHS

The following is a list of photographs of all components of the system, taken at various stages of fabrication and assembly.

Figure 21 Finished Magnet Assemblies and Armature Plates

Figure 22 Cage Structure Components*

Figure 23 Payload Simulator and Damper Components

Figure 24 Armature Coil Carrier Plates

Figure 25 Armature Coils and Carrier Plate (Side 1)

Figure 26 Armature Coils and Carrier Plate (Side 2)

Figure 27 Assembled System View 1*

---

*With the exception of the final modification of the squeeze-film damper, as described on page 67 and in Section 6.

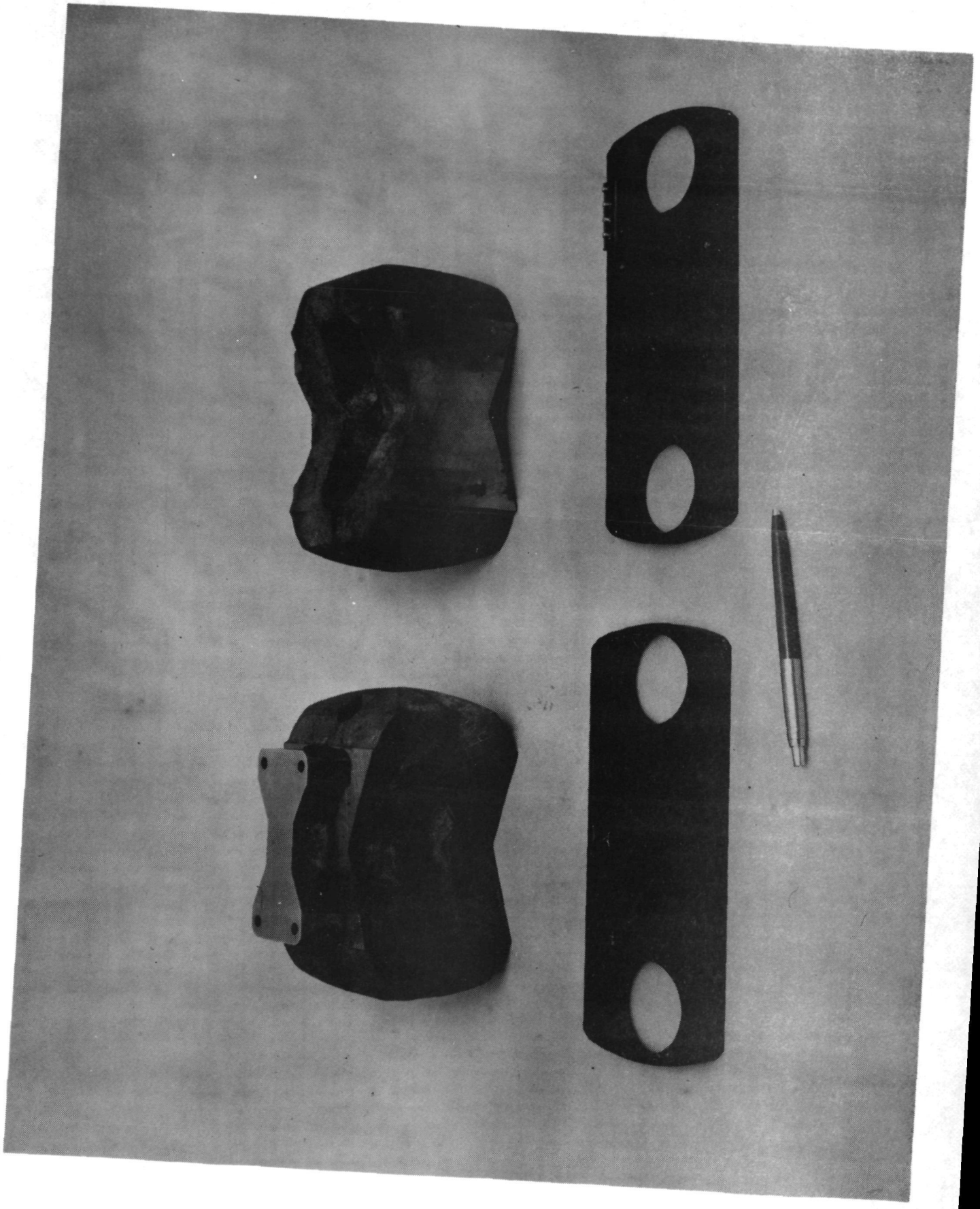

Figure 21 Finished Magnet Assemblies and Armature Plates

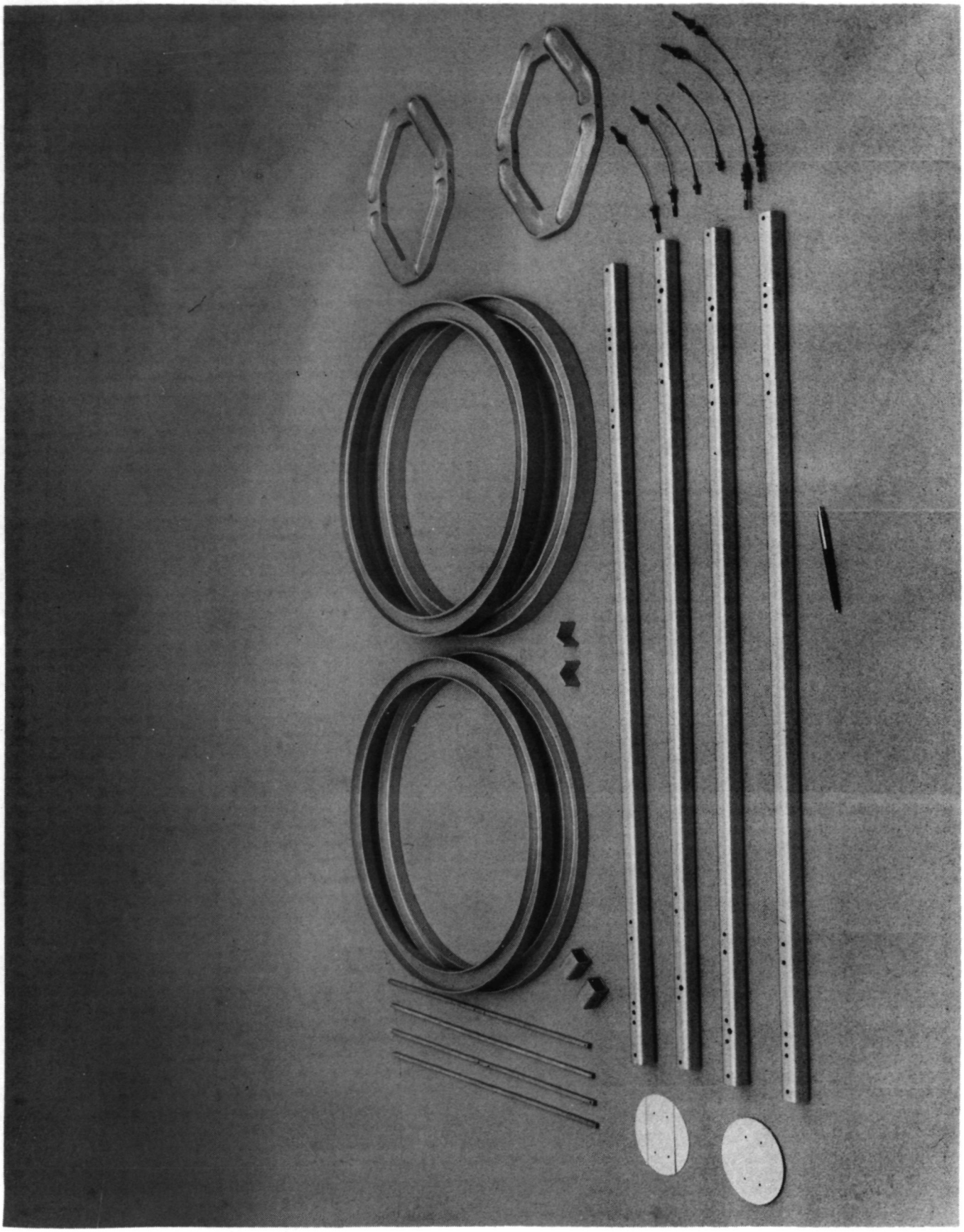

Figure 22 Cage Structure Components

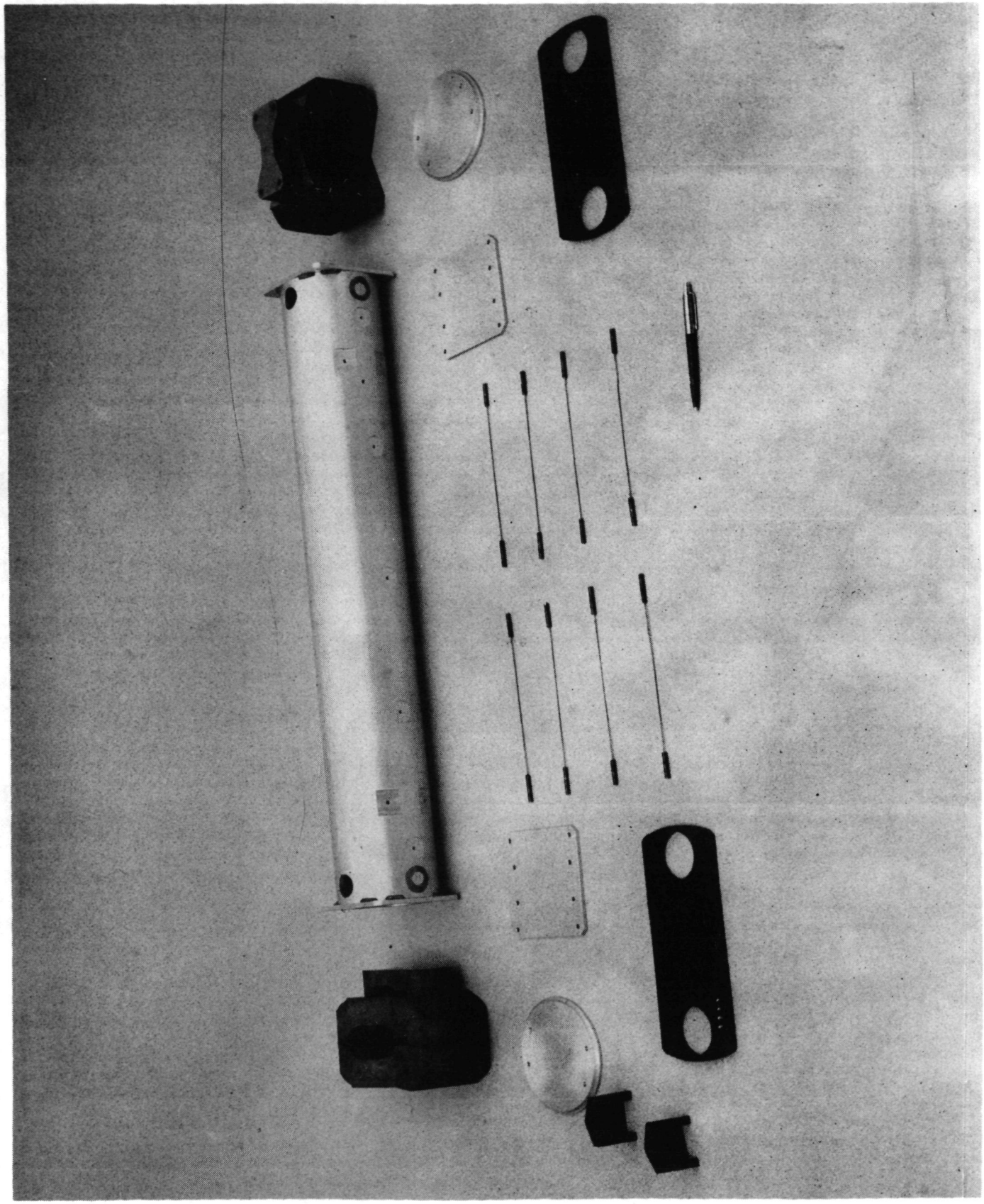

Figure 23 Payload Simulator and Damper Components

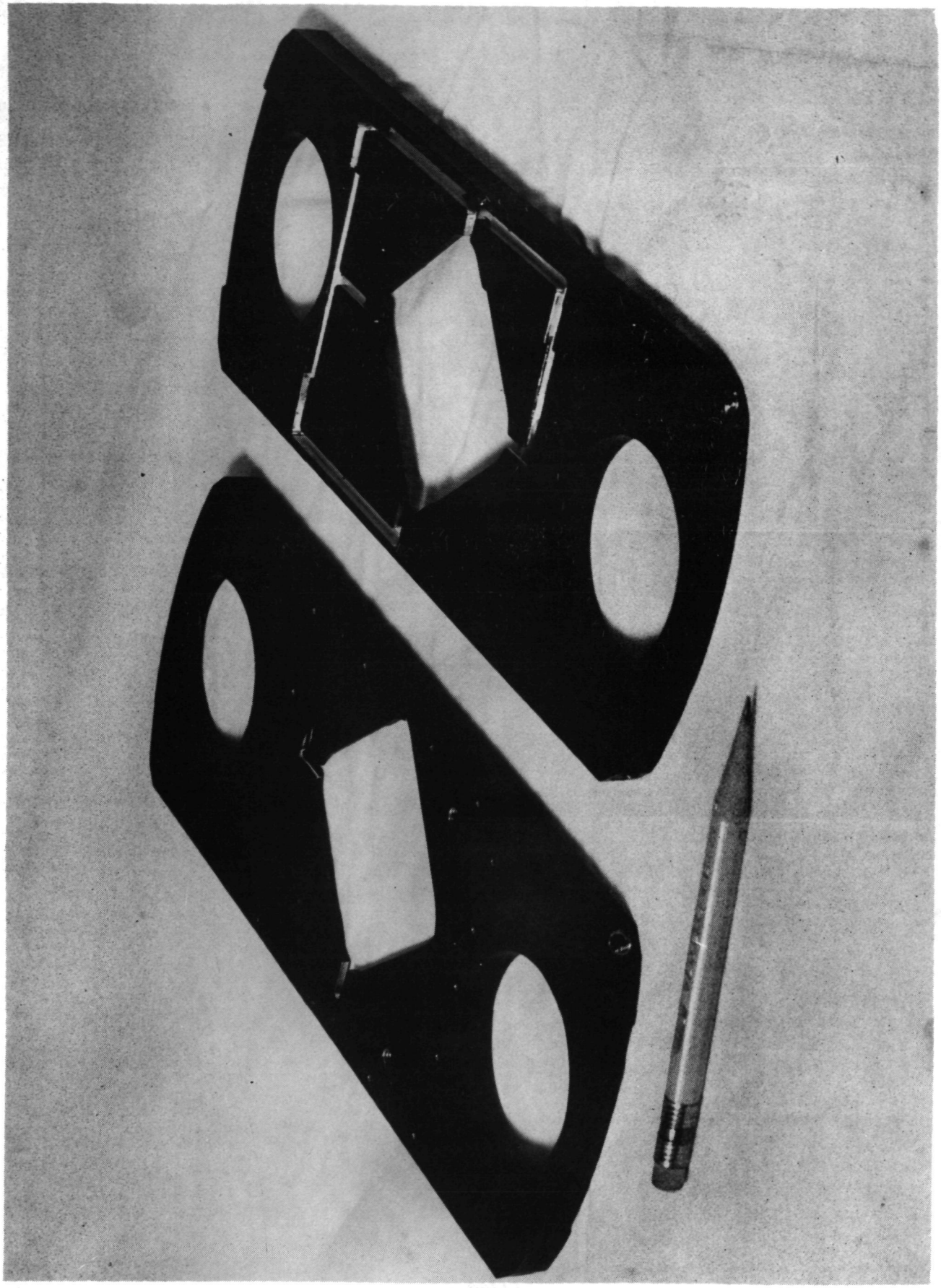

Figure 24 Armature Coil Carrier Plates (Front & Back Views)

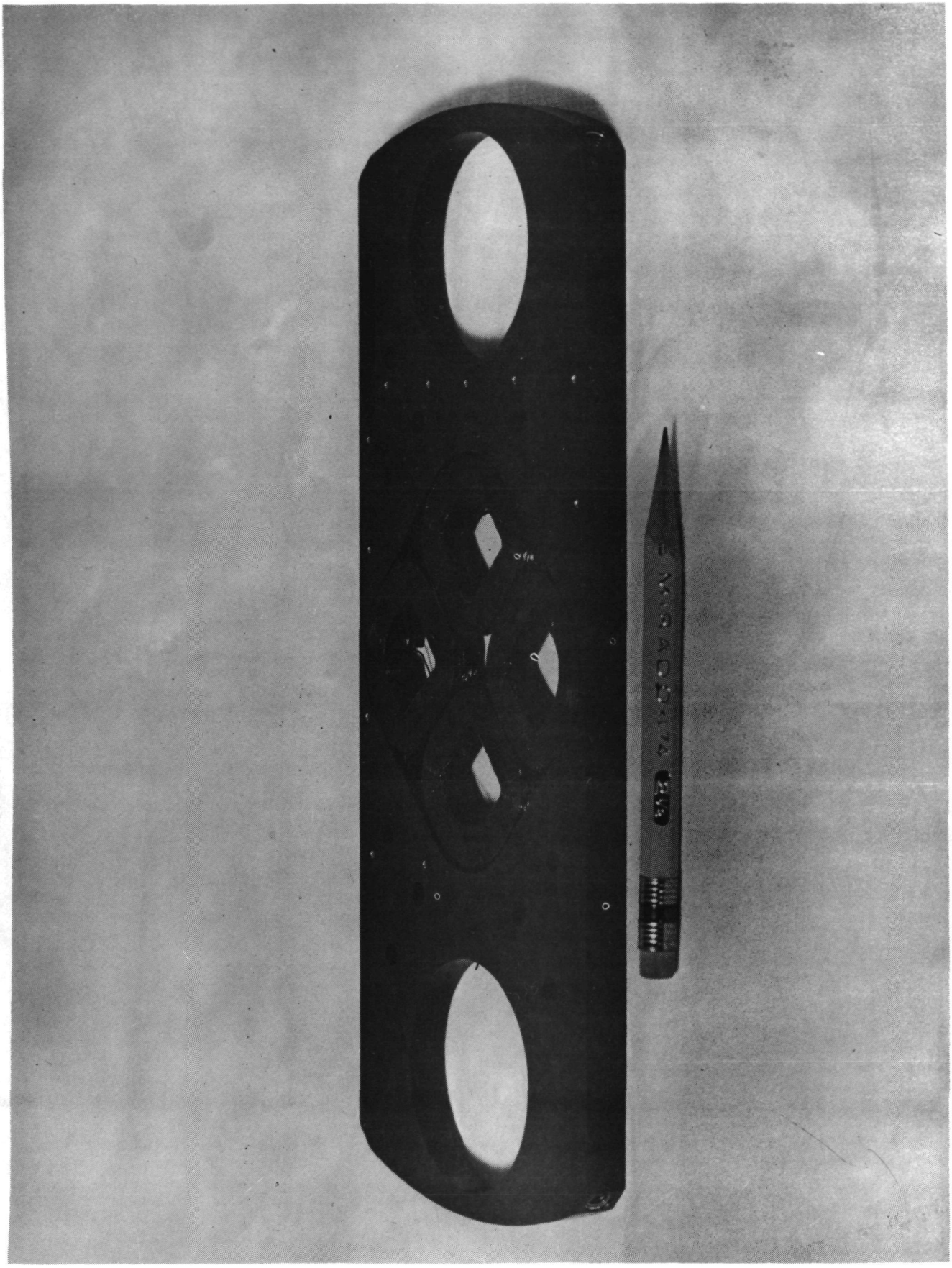

Figure 25. Armature Coils and Carrier Plate (Side 1)

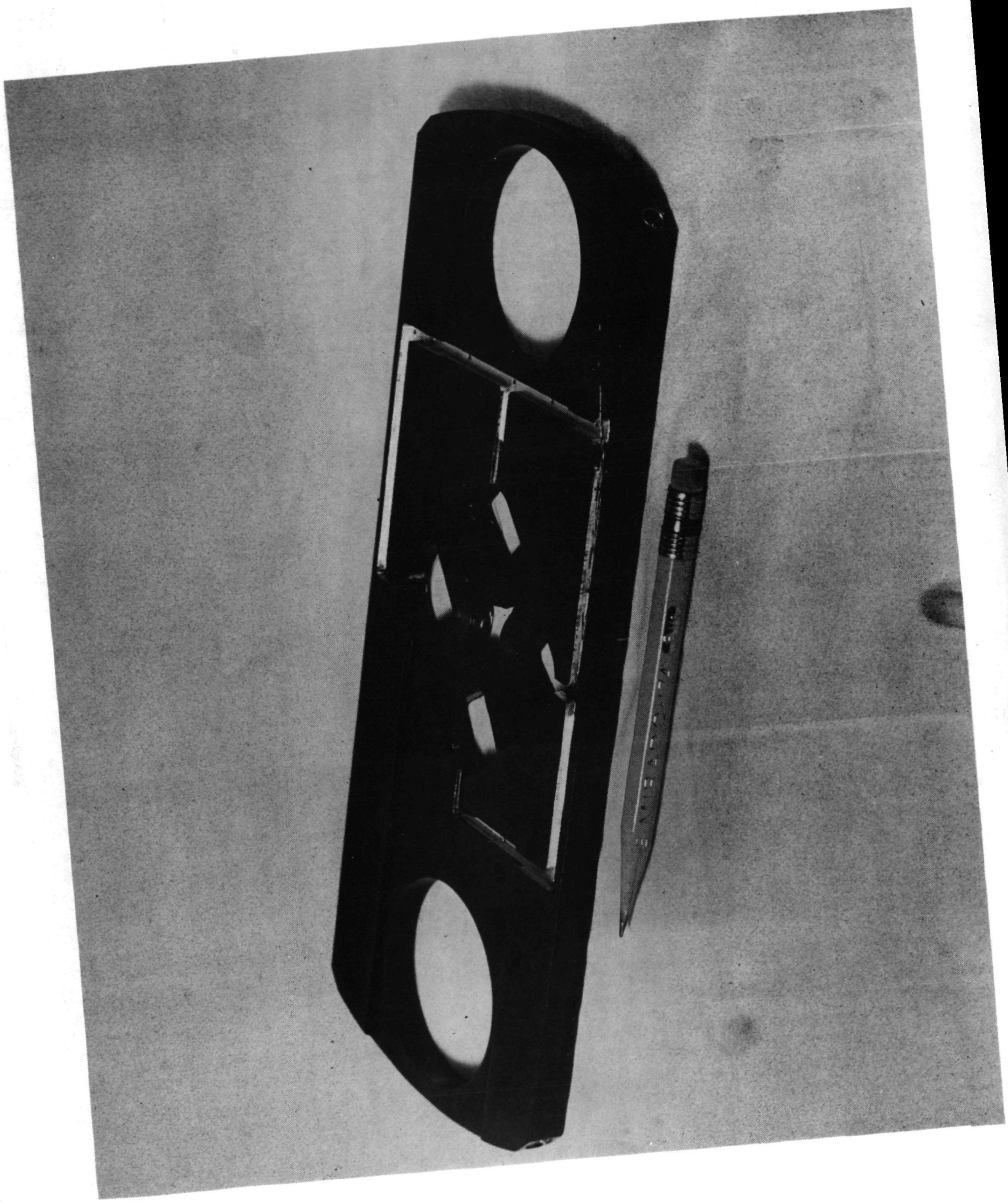

Figure 26. Armature Coils and Carrier Plate (Side 2)

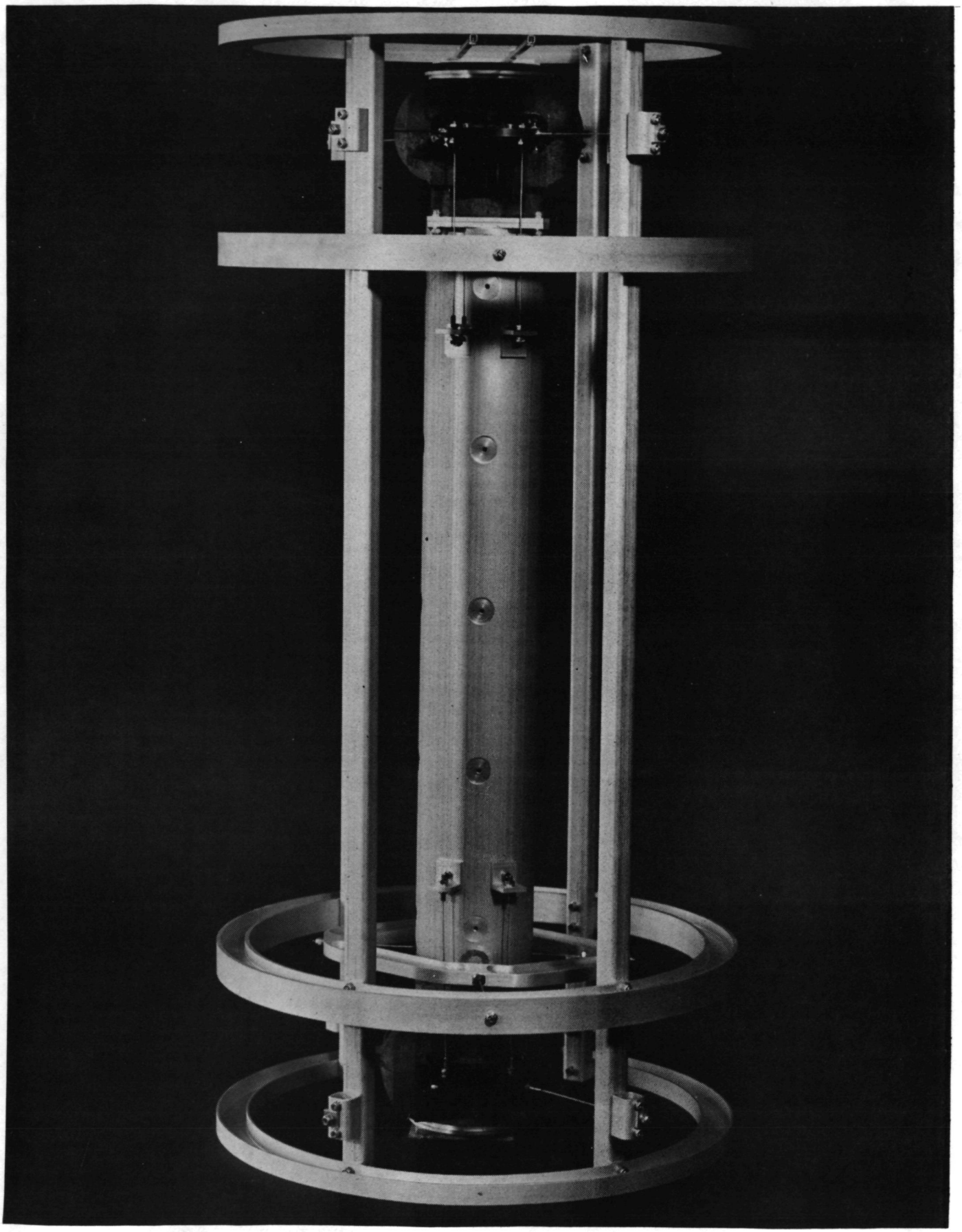

Figure 27 Assembled System View 1

5.3 ASSEMBLY PROCEDURES

The following is the sequence of steps used to assemble the test model.

(a) The cage structure was first assembled in accordance with NTI DWG 70093.

(b) The adapter plate and the inner squeeze-film damper plate were bolted to the magnet assembly.

(c) The lower magnet assembly was bolted to the 72-cm aluminum tube.

(d) The upper diamond-shaped payload suspension frame (NTI DWG 20087) was assembled to the payload package, using a pair of 10.97-cm suspension cables (NTI DWG 20091, sheet 3, Part No. 13).

(e) The payload package was suspended by supporting the suspension frame in the cage structure. The pretension in the suspension was adjusted to the required value by measuring the static deflection of the cables due to the weight of the partially assembled payload. A dial indicator was used to measure the deflections directly.

---

* With the exception of the final modification of the squeeze-film damper, as described on page 67, and in Section 6.

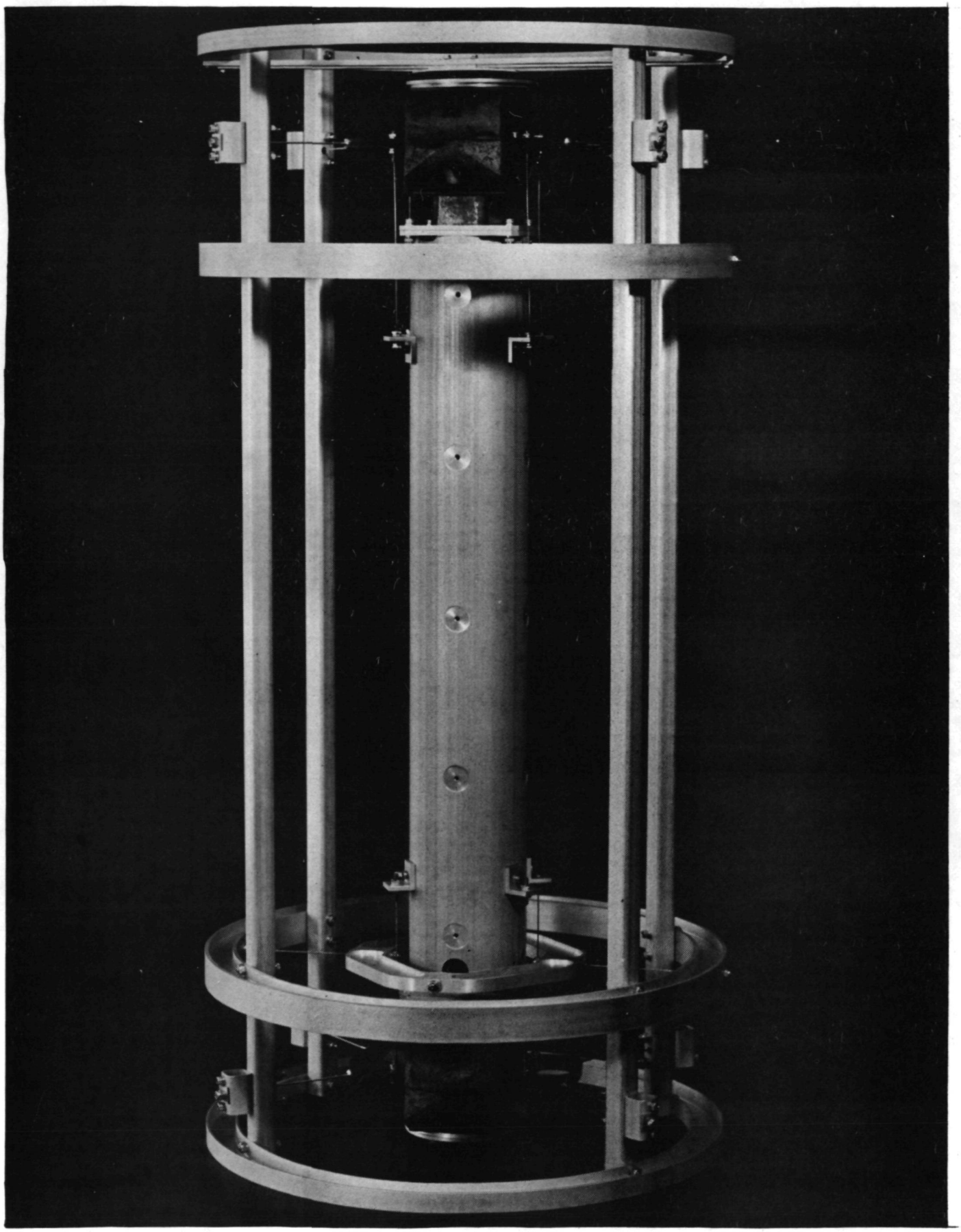

Figure 28 Assembled System View 2

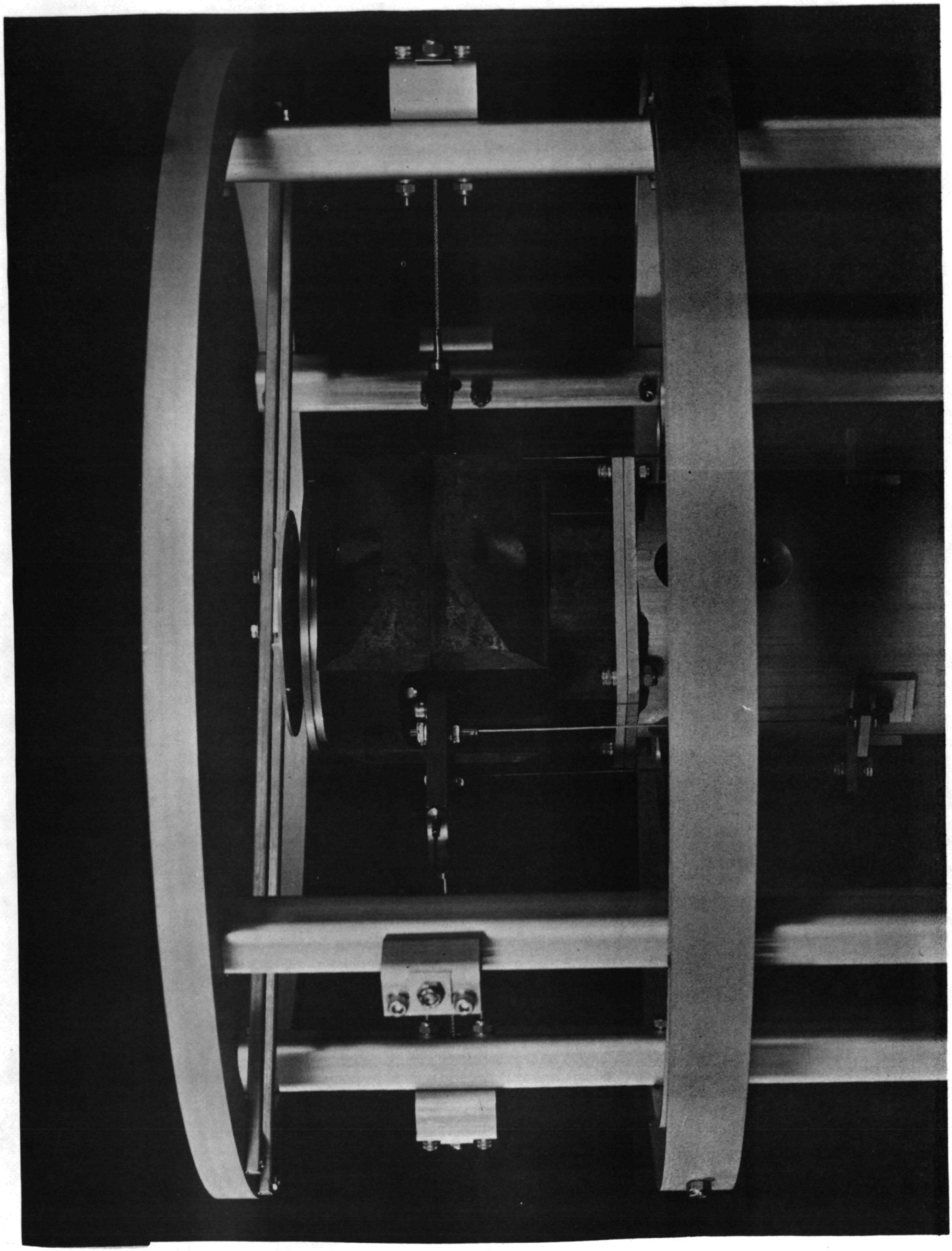

Figure 29 Close-up View of Active Damper Assembly

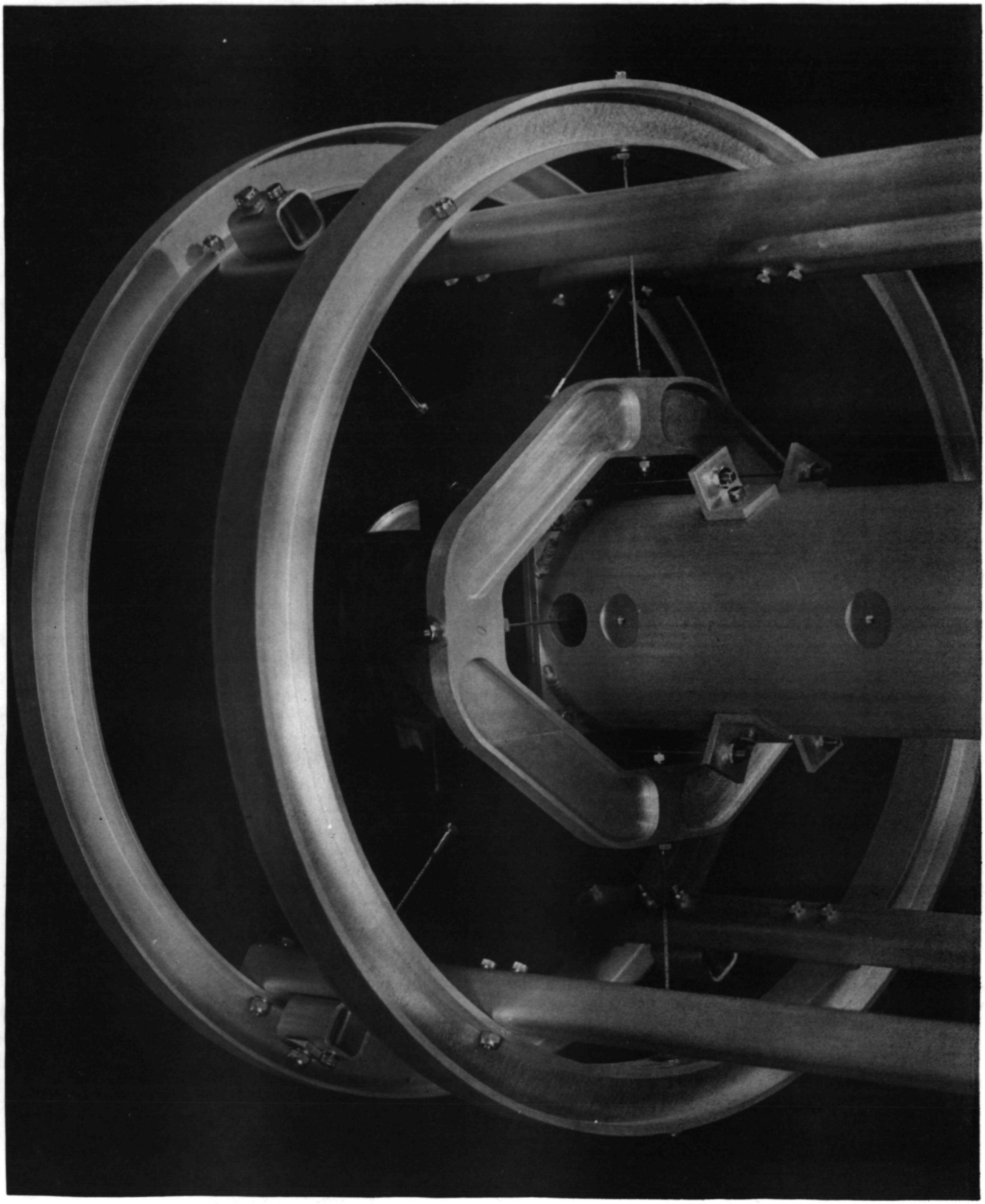

Figure 30 Close-up View of Suspension System

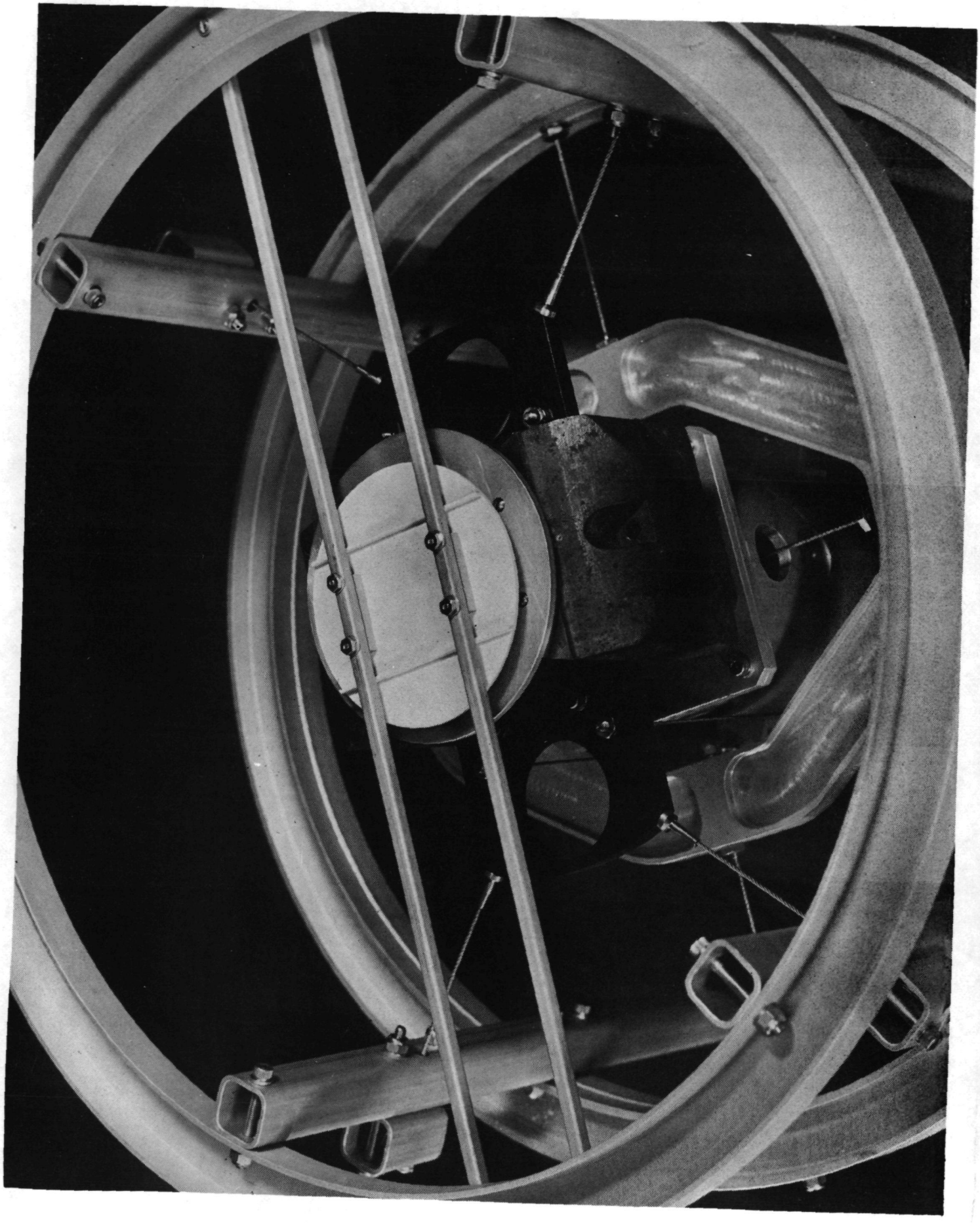

Figure 31 Close-up View of Squeeze-Film Damper, EMA and Suspension System

(f) The lower magnet assembly was removed, and the upper magnet assembly bolted to the aluminum tube. The new partial payload package was turned upside down. The lower payload suspension package was assembled and the lower inner suspension cables were adjusted to the proper pretension.

(g) The upper magnet assembly was removed, the lower magnet assembly was reinstalled, and the partial payload package was suspended to the cage structure with a pair of outer (9.96 cm) suspension cables. The pretension was adjusted to the required value by the static deflection under the weight of the partial payload package.

(h) The other pair of outer suspension cables were pulled tight between the partial payload package and the cage structure.

(i) The upper magnet assembly was added to complete the payload package.

(j) The pretension in the second pair of outer suspension cables was adjusted to the desired value by the static deflection due to the weight of the total payload.

(k) The Aramature Plates were inserted in the magnetic gaps.

(l) The Velocity Sensor Coils were mounted on to the Armature Plates.

(m) The Armature Plate was connected to the four posts of the Cage Structure, using cables for each plate.

(n) The plates were centered in the magnetic gaps by adjusting the tensions in the cables (NTI DWG 20091, Sheet 3), and in the flexures (NTI DWG 20086, Item 9)

(o) The smaller Squeeze-Film Damper Plates were installed, using two steel Support Tubes (NTI DWG 20090, Item 3) for each damper plate.*

(p) The lower Squeeze-Film Damper gap was adjusted to 0.5 cm with the system oriented vertically. The upper Squeeze-Film Damper gap was adjusted to 0.5 cm with the system oriented horizontally.

(q) Grease was injected into the Squeeze-Film Dampers

(r) Power and signal leads were connected to complete the assembly.

The assembled specimen can be oriented in any direction and tested so long as the upper Squeeze-Film Damper gap is not completely closed.

---

* The small Squeeze-Film Damper Plates and square support tubes were later replaced by large end plates rigidly mounted to the cage structure. See discussion in Section 6.

5.4 SYSTEM OPERATIONS

5.4.1 Initial Adjustments

(a) Before connecting the required ± 20 volt power supply to the Damper Control, set front panel* (FP) switches S1 down to open the output curcuit of the Power Amplifier (PA).

(b) Set Damper Control Amplifier and Signal Monitor Amplifier, Damper Control, set (SMA) to maximum gain by turning FP gain adjustments G1, G2, and G4 fully CW.

(c) Short both velocity input terminals and FP input JD to System Common (SC)*.

(d) Trim FP zero adjustment Z2 until the PA output voltage appearing at FP output jack JC is within ± 20 mv from SC.

(e) Trim FP zero adjustment Z1 until the SMA output voltage appearing at FP output jack JA is ± 20 mv from SC.

(f) Connect velocity transducer to Damper Control. Verify cable connections and functioning of amplifiers by the presence of output signal at JA on FP when the transducer is disturbed.

(g) Turn G2 and G4 fully CCW to reduce the gain of the Damper Control to minimum (about 2). Do not open FP switch S2 when reducing G4.

(h) Apply sinusoidal voltage (1v, 0-pk, at 20 Hz) from a low-impedance source to JD. Verify proper functioning of external excitation attennator G3 by monitoring PA output voltage appearing at JC. Maximum gain (corresponding to G3 fully CW) is unity.

(j) Connect PA to actuator armature by closing switch S1. The EMA and the Damper Control are now in the Vibration Test Configuration. (VTC). Determine the lowest natural frequency of specimen. This may be accomplished by the

* See Figure 32.

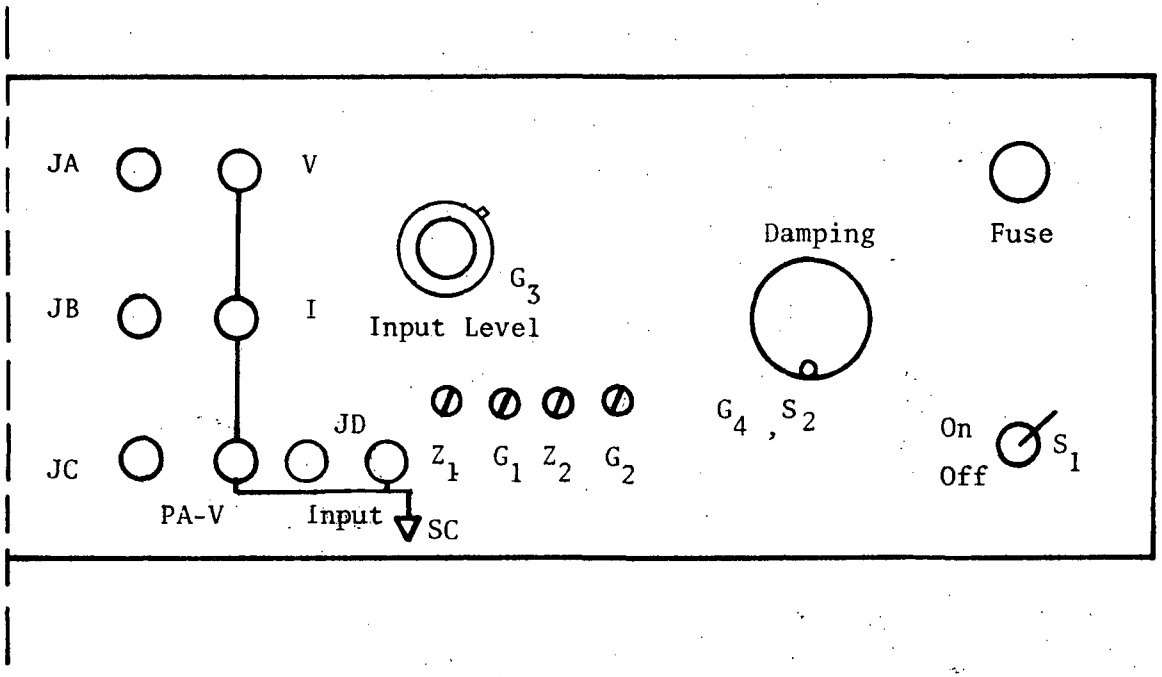

Figure 32 Damper Control Front Panel Layout

use of G3 for level control, and the buffered relative velocity signal from JA. Adjust the frequency of the excitation signal until it and the velocity signal are either in phase or 180° out of phase with each other near this natural frequency. If the signals are in phase, reverse the power amplifier connection. Positive damping will be added to the structure when the signals are 180° out of phase.

(k) Increase damping to the system, (while it is vibrating in its fundamental mode) by gradually rotating G4 until the full CW position is reached. The specimen response amplitude should be reduced by this operation. Further increase in damping is achieved by rotating G2 CW until system instability occurs (a high-frequency oscillation, usually in the audio range). Due to voltage- and current-limiting features in the Damper Control, *sustained oscillation of this type will not damage the system.*

(l) Reduce system gain by rotating G2 CCW until stability is restored.

(m) Review and trim offset adjustments at the final gain settings.

(n) Verify stability of system in simultaneous, 4-channel operation. Slight gain reduction may be necessary.

The active damper systems are now operational.

5.4.2 Miscellaneous Notes On Regular Operations

(a) On account of the low-drift feature of the system electronics, zero offset adjustments were found to be unnecessary in day-to-day operations. Warm-up after turn-on is desirable but not needed.

(b) The power amplifier is internally protected against damage due to accidental short-circuiting of its output leads.

(c) The fuse on the front panel protects the armature windings in the EMA from over-current conditions.

(d) Normal variation of damping is accomplished by adjustment of G4.

Section 6

TESTS AND RESULTS

The 0.125-scale omnidirectional payload isolation model, including the Simulated Payload and the Cage Structure (hereinafter called the specimen) was tested in three phases. Phase I contained a series of vibration tests conducted to establish the low-frequency dynamic characteristics of the specimen experimentally. Phase II contained a series of constant-force frequency sweep tests conducted to establish performance characteristics of the isolation system. Finally, Phase III tests were conducted at LaRC on a large shaker to evaluate the performance characteristics of the isolation system under various controlled input acceleration environments.

6.1 PHASE I TESTS

6.1.1 Test Objectives

Dynamic calibration tests were conducted at NTI. Test objectives were:

(a) To verify results of design, fabrication, assembly and setup procedures, and to establish that the specimen is ready for isolation evaluation tests.

(b) To determine low-frequency dynamic characteristics of the specimen, and their variation with respect to response amplitude.

(c) To determine damper performance and optimal control system gain.

6.1.2 Test Equipment

Exciter:	For lateral vibration tests, the EMA were used to excite the specimen. For longitudinal vibration tests, a Pye-Ling Model V50/A 50-lb shaker was used.
Power Amplifier:	RCA HC2000 H Power Operational Amplifiers
Signal Source:	Exact Model 123 Waveform Generator
Transducers:	Columbia Model 902 H Accelerometers, (2 units at 120 pcb/g) Relative Velocity Transducer (4 units at 5.1 mv/(cm/sec)).
Signal Amplifiers:	Kistler Model 566M117 Charge Amplifiers (2), Datel Model 200 C Instrumentation Amplifiers (4)
Recorders:	Hewlett-Packard Model 7046A X-Y Recorder, Tandberg Series 100 4-track FM Instrumentation Recorder, Bell & Howell Model 5-134 Datagraph with Model 7-316 Galvolometers, driven by Neff Model 129 Amplifiers.
Monitor, Display & Measure:	Tektronics Model 465 Dual Trace Oscilloscope, Hewlett-Packard Model 120513 Dual Trace Oscilloscope. Darcy Model 440 Digital Multimeter, Monsanto Model 100B Timer/Counter.
Filter:	Spectral Dynamics Model SD121 Tracking Filter (Bandwidth = 1 Hz)

6.1.3 Test Setup

6.1.3.1 Test Specimen

Two 15-kg steel plates were bolted to the Cage Structure, using 6 brackets for attachment to the main square tubes, see NTI DWGS 20097 and 20098. These weights were used to simulate, at least in part, the mass of the vehicle model during Phases I and II tests. The test specimen was suspended from above with 1/4-inch Nylon ropes, as shown in Figures 33 and 34. The specimen was set up and tested in three configurations:

Specimen Configuration	Payload Axis	Damper Axes 1 & 3*
IA	Vertical	Horizontal
IB	Horizontal	Horizontal
IC	Horizontal	Vertical

6.1.3.2 Excitation

Steady-state sinusoidal excitation was used for determination of mode shapes, natural frequencies and damping. To excite the specimen in the longitudinal direction, the Pye-Ling V50/A shaker was used. For excitation in the lateral directions, EMA's were used.

6.1.3.3 Damping

For each test configuration and excitation pattern, two test series were conducted, corresponding to low and high damping conditions which are defined below:

Low Damping: Squeeze-Film Dampers without grease; and all Damper Controls on, G4 fully CCW.

High Damping: Squeeze-Film Dampers filled with proper amount** of grease, all Damper Controls set at maximum gain (G4 fully CW).

---

* Damper Axes 1 & 3 coincide with the lengthwise center lines of the force coil plates of the upper and lower EMAs, respectively. Damper Axes 2 & 4 are perpendicular to Axes 1 & 3.

**To be determined during Phase I tests to achieve optimum low-frequency amplitude suppression and high-frequency isolation.

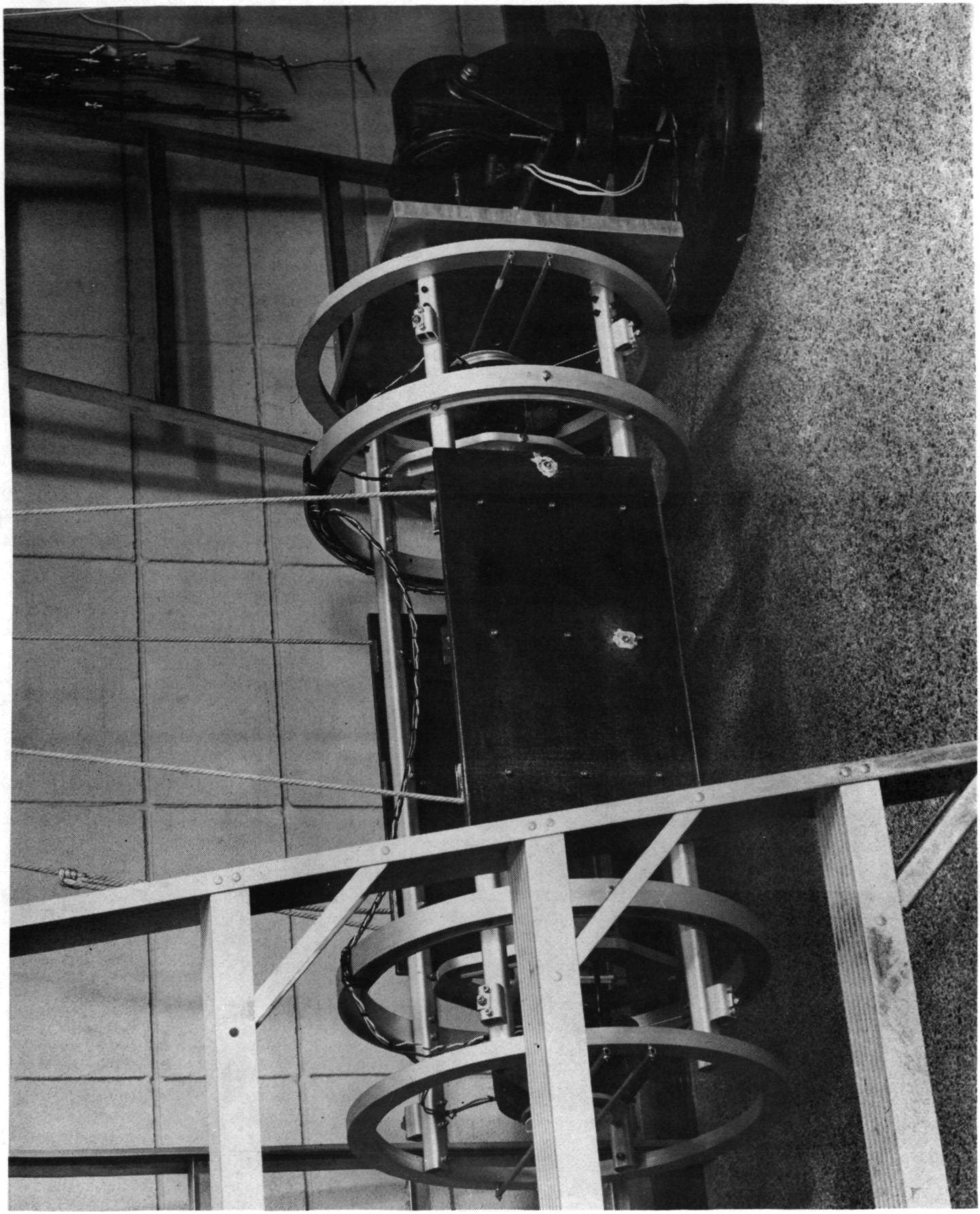

Figure 33 Suspension of Specimen in Phase I & Phase II Tests

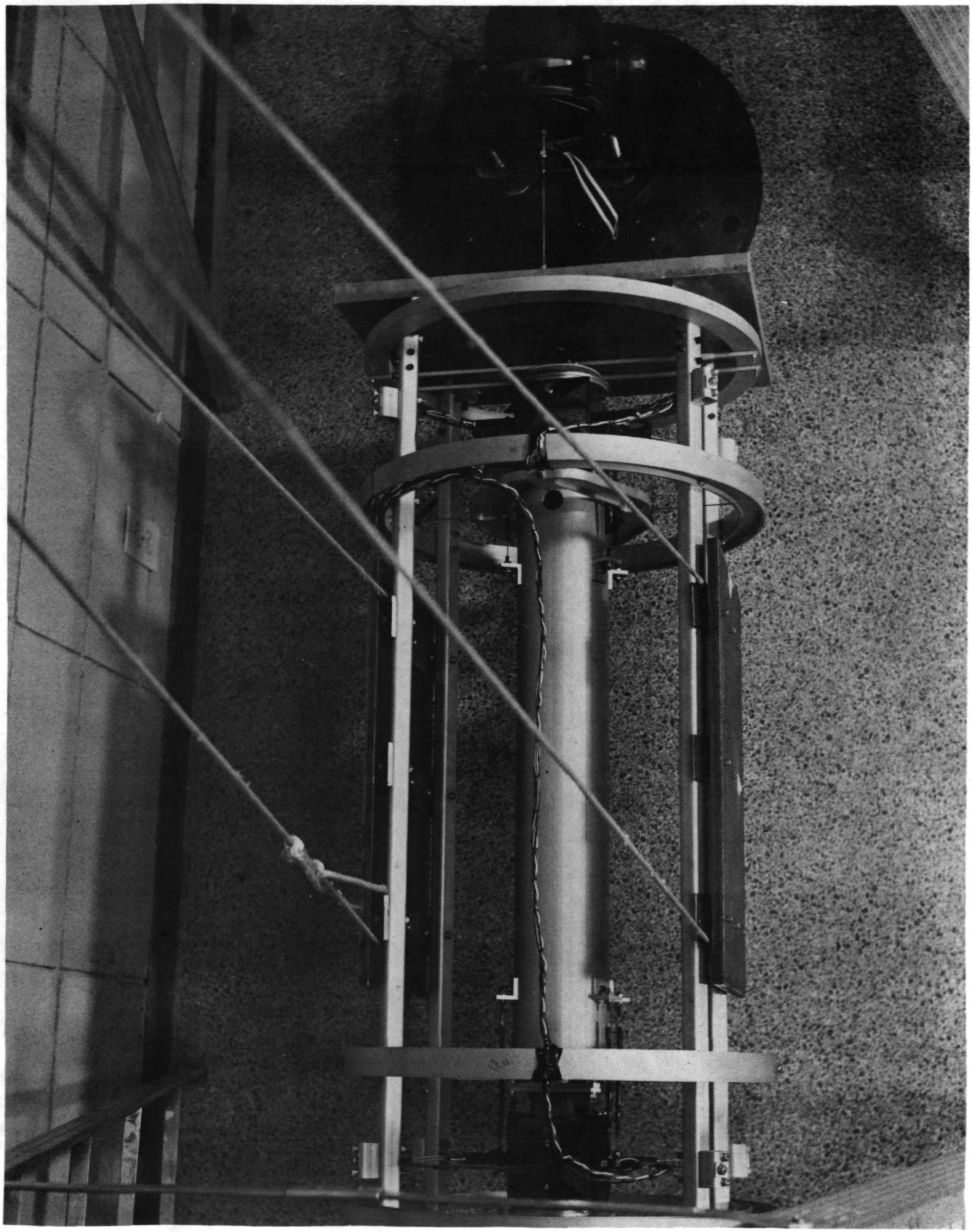

Figure 34 Suspension of Specimen in Phase I & Phase II Tests

6.1.4 Test Procedures

For each low damping test configuration, natural frequencies were determined in steady-state sinusoidal tests, using phase relationship between excitation and response (acceleration or velocity) as criteria. Mode shapes were measured at two points on the payload to identify the modes. In the axial direction, the natural frequency of the rigid-body payload mode is significantly lower than the "elastic" modes and a single shaker was found to be amply adequate for Phase I test objectives. For all lateral modes, it was found necessary to conduct the required "modal survey" tests using all four EMA and Damper Control channels in the VTC simultaneously.

Damping was measured by recording and analyzing free vibration decay records, which were obtained by removing the excitation from the specimen after a steady-state resonance condition was established.

Damping was next added and all above tests were repeated.

Phase I test instrumentation is shown in Figure 35.

6.1.5 Test Results

During Part 1 of Phase I tests, the spring-connected Squeeze-Film Damper was used. The following results were obtained for the rigid-body translational mode of the payload in the axial direction.

Configuration:	IB
Natural Frequency:	8.83 Hz
Low Damping (C/C_{cr}):	0.006
High Damping (C/C_{cr}):	0.057*

---

* At optimum squeeze-film diameter of 2.5 cm, which was determined experimentally and provided maximum damping achievable with the design.

Figure 35 Phase I and Phase II Test Instrumentation

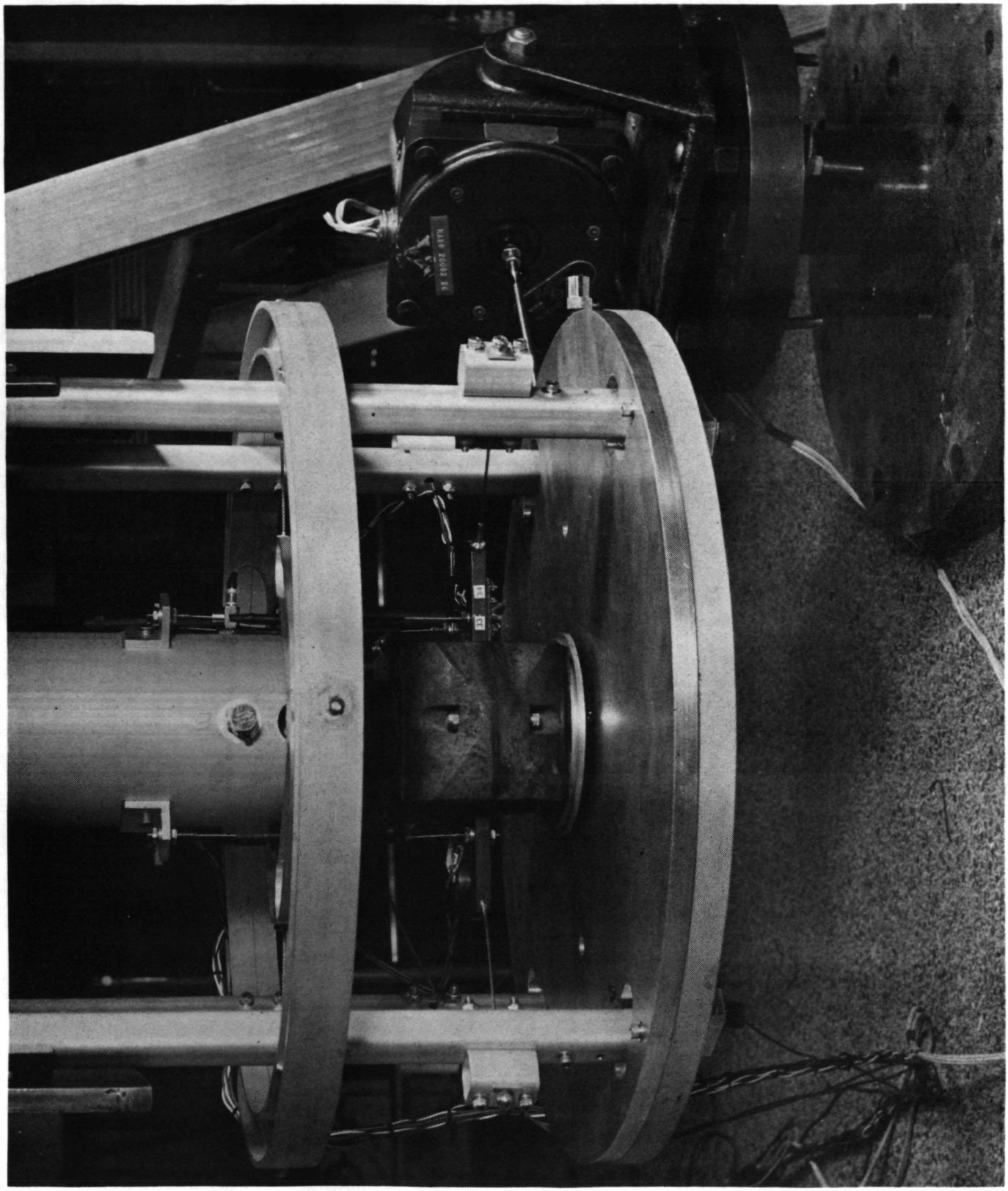

Figure 36 Specimen with Modified (Rigidly Attached) Outer Squeeze-Film Damper Plates

It was verified experimentally that by stiffening the series Springs (the square tubings) connected to the Squeeze-Film Dampers, much greater damping than the value of 0.057 could be achieved. A design modification was accordingly introduced at this time to eliminate these series damper springs (Part No. -3, NTI DWG. 20090, 4 places). The redesign also consisted of the replacement of the original damper plates (Part No. -3, NTI DWG. 20085, 2 places) with two large aluminum plates, each covering the entire end of the Cage Structure. The dimension of the plates are 1.27 cm (t) X 50.8 cm(diam). These plates are bolted on to the Disc Support Rings (Part -3, NTI DWG. 20093,). The modified design is shown in Figure 36 and NTI DWG 20094.

While parts for the above modification were being fabricated, Phase II tests were conducted on the model in its un-altered configuration so that the resulting frequency-sweep test data can be compared with corresponding results after the modification.

Part II of Phase I tests were conducted after the above mentioned modifications on the Squeeze-Film Damper were completed. Test results are summarized in Table I on the following page, and show that

(a) High damping was achieved in the longitudinal direction with the modifications.

(b) High damping was achieved in lateral vibrations in the plane containing active damper axes 2 & 4.

(c) Maximum damping achieved in active dampers 1 & 3 was 30%. To raise the control system gain higher would have caused instability and high frequency (about 1,100 Hz) vibrations would occur.

(d) Natural frequencies of the lateral modes become higher in the preload direction.

Specimen Config.	Mode Description	Natural Frequency	Damping Low	Damping High
	(Rigid-Body Payload Modes)	Hz	%	%
IA	Longitudinal Translation	11.77	0.88	>50
	Rocking in Plane 1-3 Response @ 3>1	7.25	1.8	28
	Rocking in Plane 1-3 Response @ 1>3	8.01	1.6	22
	Translation in Plane Containing Damper Axes 2&4	7.01	1.2	73
	Rocking in Plane Containing Damper Axes 2&4	6.46	1.7	>73
IB	Longitudinal Translation	8.83	0.6	
	Longitudinal Translation	12		>50
	Translation in Plane 1-3	7.66	1.3	30
	Rocking in Plane 1-3	8.33	1.3	28
	Translation in Plane 2-4	10.47	1.5	73
	Rocking in Plane 2-4	10.33	1.0	38
IC	Translation in Plane 1-3	11.06	1.6	12
	Rocking in Plane 1-3	9.99	1.5	24
	Translation in Plane 2-4	7.45	1.2	41
	Rocking in Plane 2-4	8.15	1.9	46

Table I Summary of Phase I, Part II Test Results

6.2 PHASE II TESTS

6.2.1 Test Objectives

Phase II tests were conducted at NTI to establish performance characteristics of the isolation system design.

6.2.2 Test Equipment

All test equipment used for Phase I tests was used. The EMA's were not used as shakers in Phase II tests.

6.2.3 Test Setup

A number of combinations of specimen and excitation orientations were tested to investigate isolation properties of the system. Table II is a resume of the test configurations covered during Phase II tests.

6.2.4 Test Procedures

Sinusoidal frequency sweep tests at constant force amplitudes were used exclusively for Phase II tests. The frequency range covered was either from 5 to 2,000 Hz or from 5 to 200 Hz. The optimum sweep rate was determined experimentally and was approximately 50 Hz/minute from 5 Hz to 50 Hz and 150 Hz/minute from 50 Hz to 2,000 Hz. The amplitude of the excitation was 5.5 N (0-pk), except for Tests II B & II C when the dynamic linearity of the specimen was investigated.

For each test specimen and excitation setup, the frequency response curve of the Cage Structure, as measured by an accelerometer located near the point of excitation, was plotted against the frequency on the H-P 7046A X-Y recorder. The acceleration signal was filtered and converted to a dc voltage proportional to

Test No.	Specimen Config.	Excitation Direction	Excitation Location	Payload Sensor Location	Damper Config.	Data (Fig. No.)	Remarks
II A	IA	Axial	P1	Lower end, Tube	SFD* Empty	37	*SFD=Squeeze-Film Dampers
II B	IA	Axial	P1	Lower end, Tube	SFD Empty	38	Four sweep tests at diff. force levels
II C	IA	Axial	P1	Lower end, Tube	SFD Filled	39	Four Sweep Tests at diff. force levels
II D	IA	2-4	P2	Rel. Vel. V4	AD* on	40	*AD=Active Dampers
II E	IA	2-4	P2	Mid-Span, Tube	AD on and off	41	5-200 Hz
II F	IA	2-4	P2	Mid-Span, Tube	AD on	42	5-2,000 Hz
II G	IB	Axial	P1	Mid-Span, Tube*	SFD Empty	43	Acceleration oriented in longitudinal direction
II H	IB	Axial	P1	Mid-Span, Tube	SFD Filled	44	Acceleration oriented in 1-3 direction
II J	IB	1-3	P3	Mid-Span, Tube	AD off	45	
II K	IB	1-3	P3	Mid-Span, Tube	AD on	46	
II L	IB	1-3	P3	Mid-Span, Tube	AD on & off	47	5-200 Hz
II M	IC	2-4	P2	Rel. Vel. V4	AD on & off	48	
II N	IC	Axial	P1	Mid-Span, Tube	*	49	*SFD empty and filled
II P	IB	1-3	P3*	Mid-Span, Tube	AD off	50	*and acoustic excitation
II Q	IB	1-3	P3	Mid-Span, Tube	AD off	51	

P1 = center, lower SFD plate
P2 = edge, lower SFD plate
P3 = center, steel plate

Table II Resume of Phase II Tests

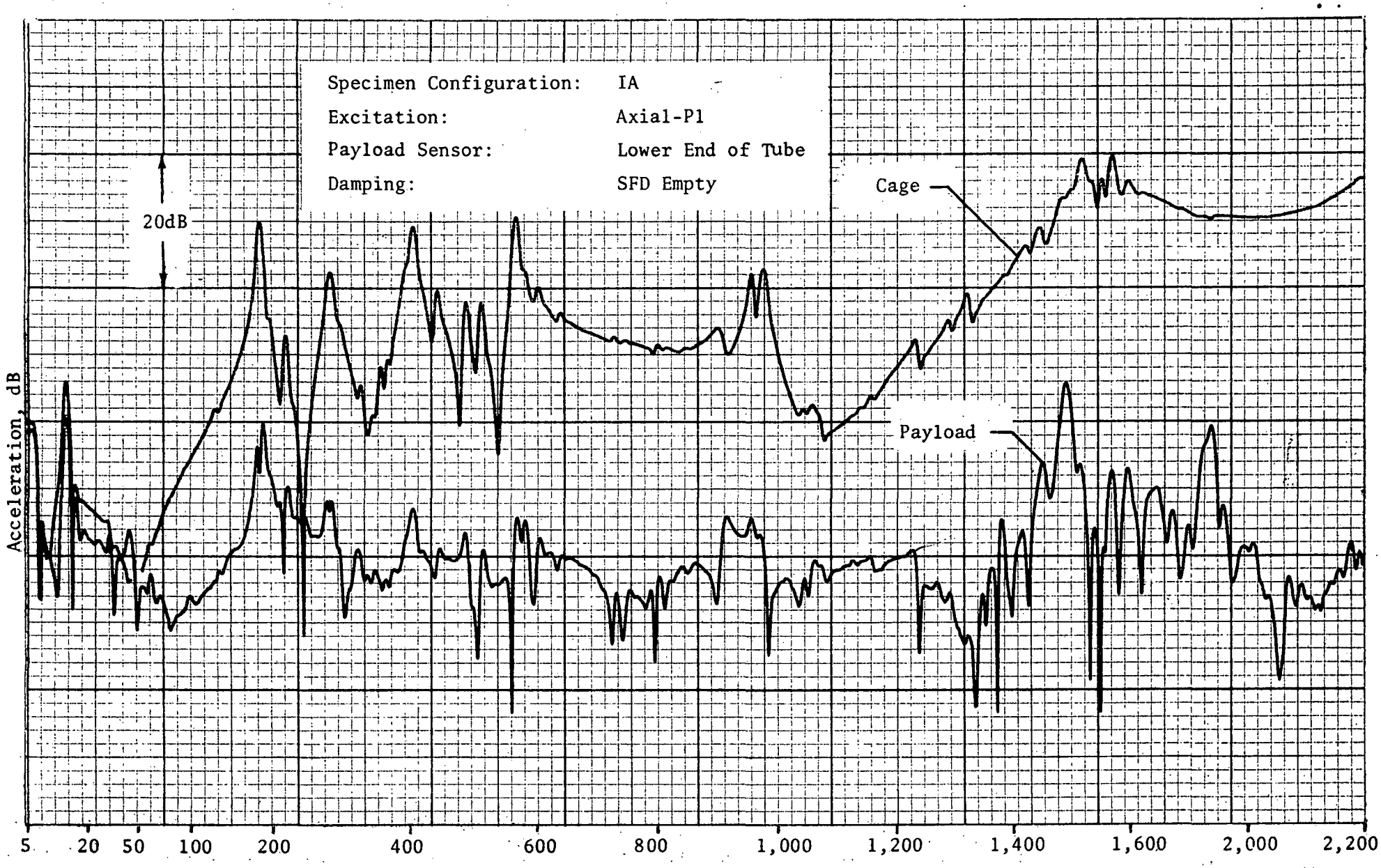

Figure 37 Test IIA

Specimen Configuration: IA

Excitation: Axial-P1

Payload Sensor: Lower End of Tube

Damping: SFD Empty

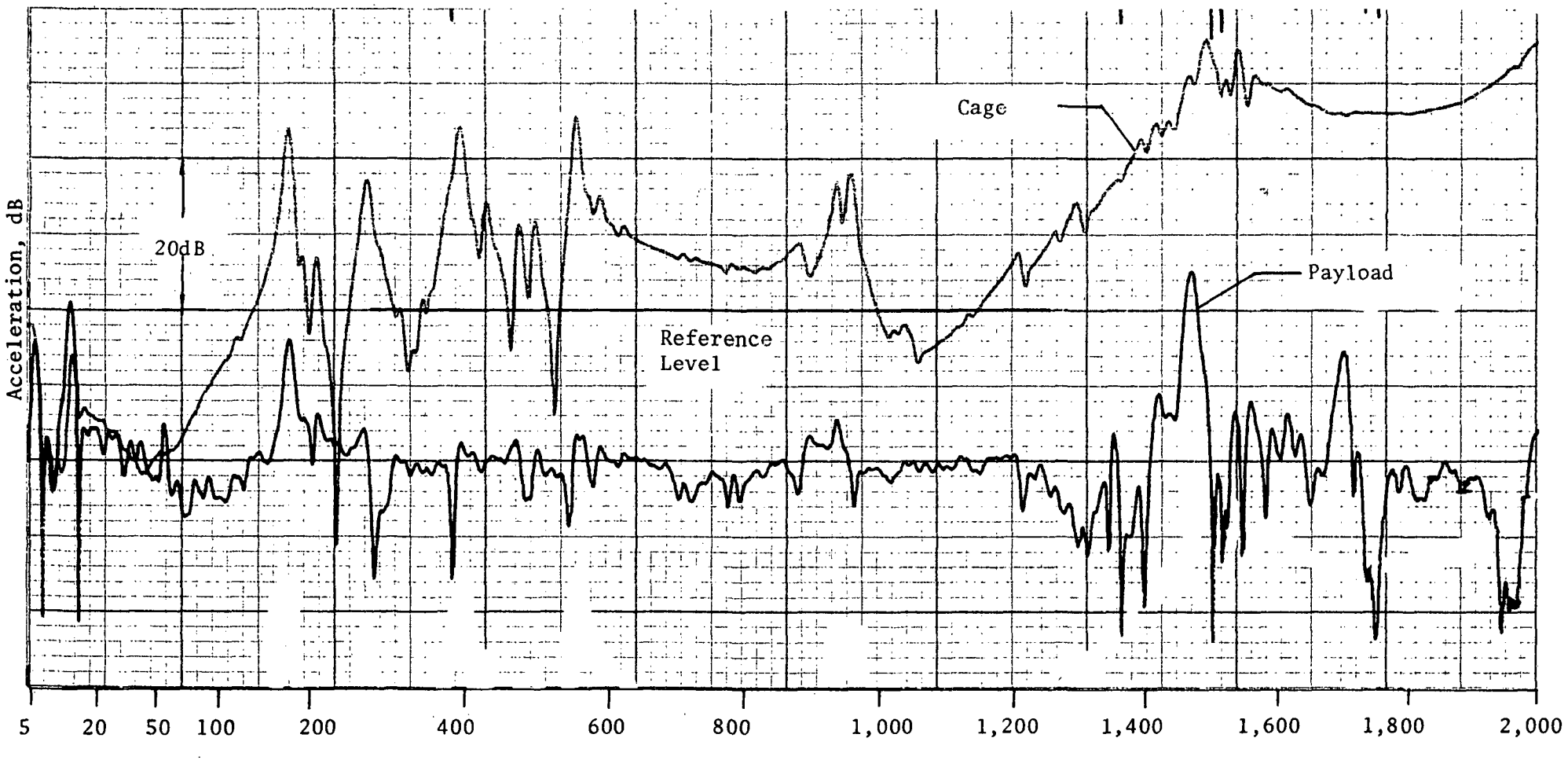

Force Level: 0.5 N pk-pk

Figure 38-1 Test IIB, Sweep No. 1

Specimen Configuration: IA
Excitation: Axial-P1
Payload Sensor: Lower End of Tube
Damping: SFD Empty

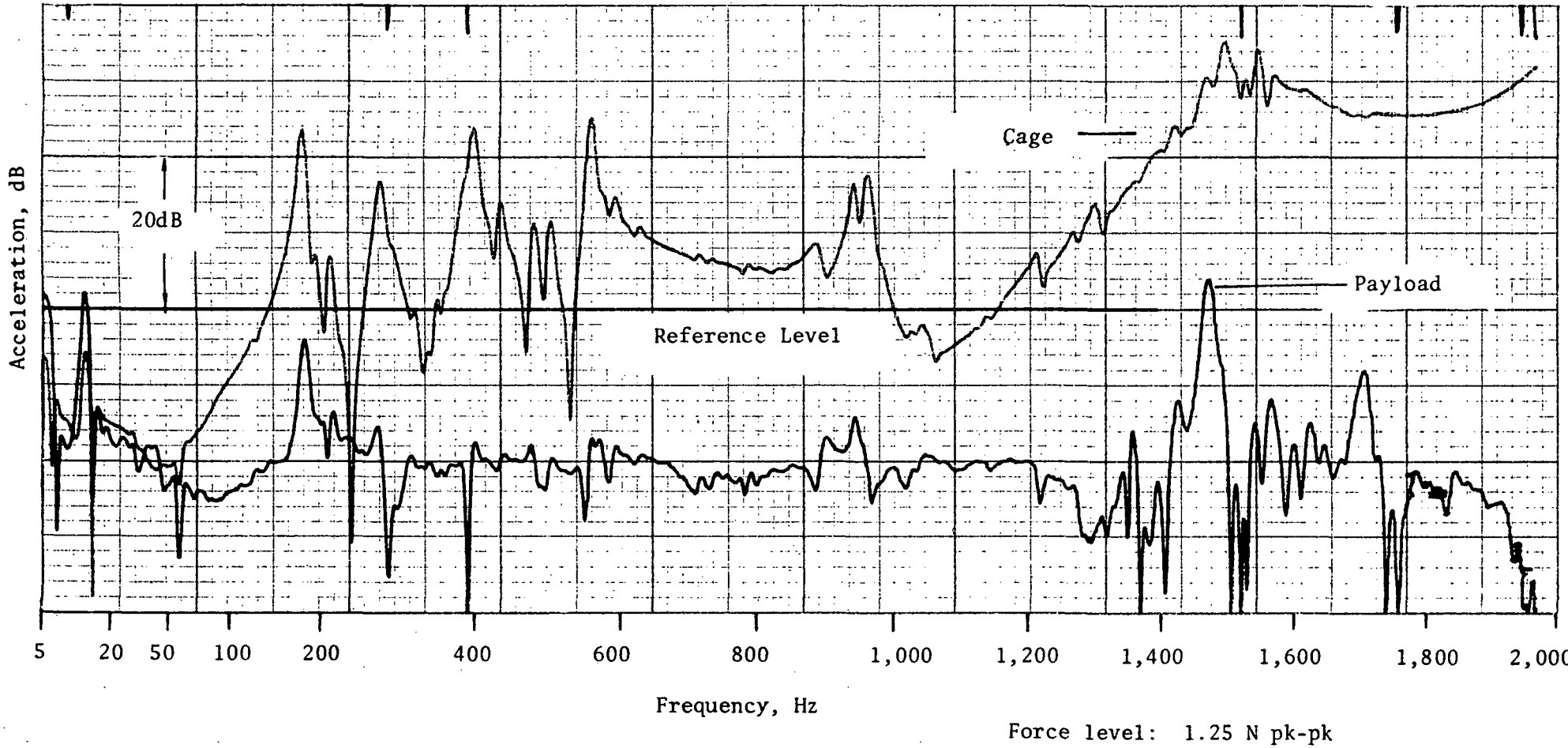

Force level: 1.25 N pk-pk

Figure 38-2 Test IIB, Sweep No. 2

Specimen Configuration: IA
Excitation: Axial-P1
Payload Sensor: Lower End of Tube
Damping: SFD Empty

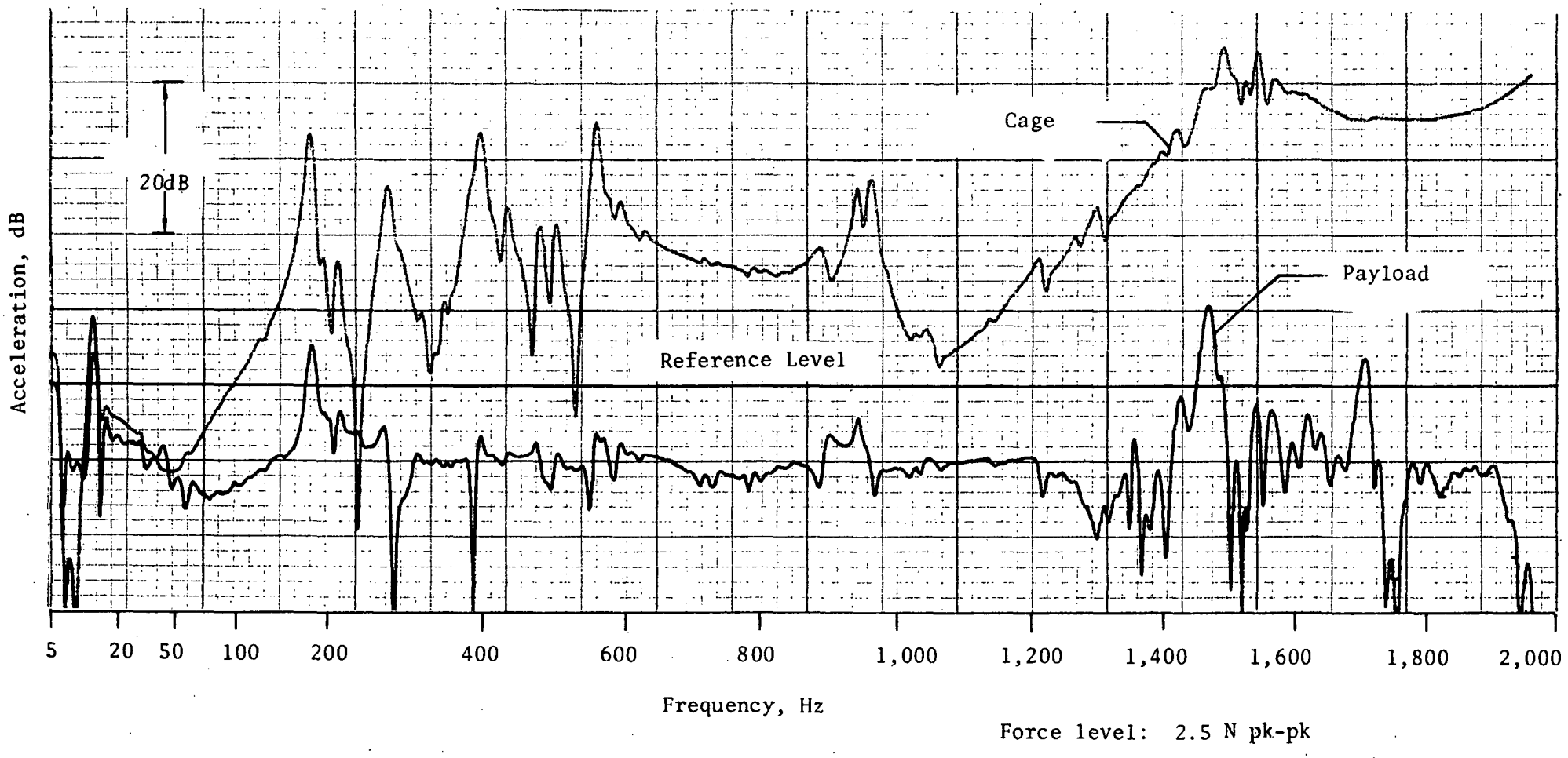

Figure 38-3 Test IIB, Sweep No. 3

Specimen Configuration: IA
Excitation: Axial-P1
Payload Sensor: Lower End of Tube
Damping: SFD Empty

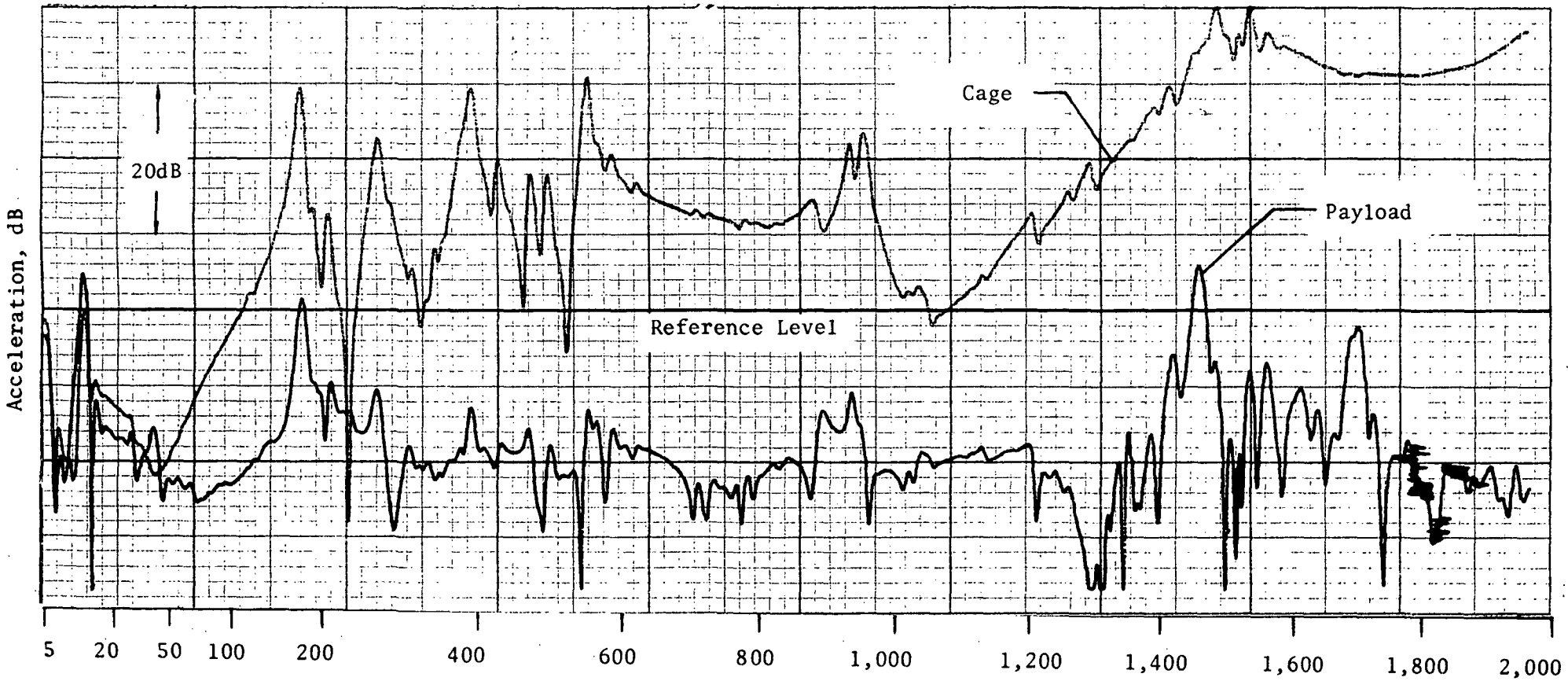

Force level: 5.0 N pk-pk

Figure 38-4 Test IIB, Sweep No. 4

Specimen Configuration: IA
Excitation: Axial-P1
Payload Sensor: Lower End of Tube
Damping: SFD Filled

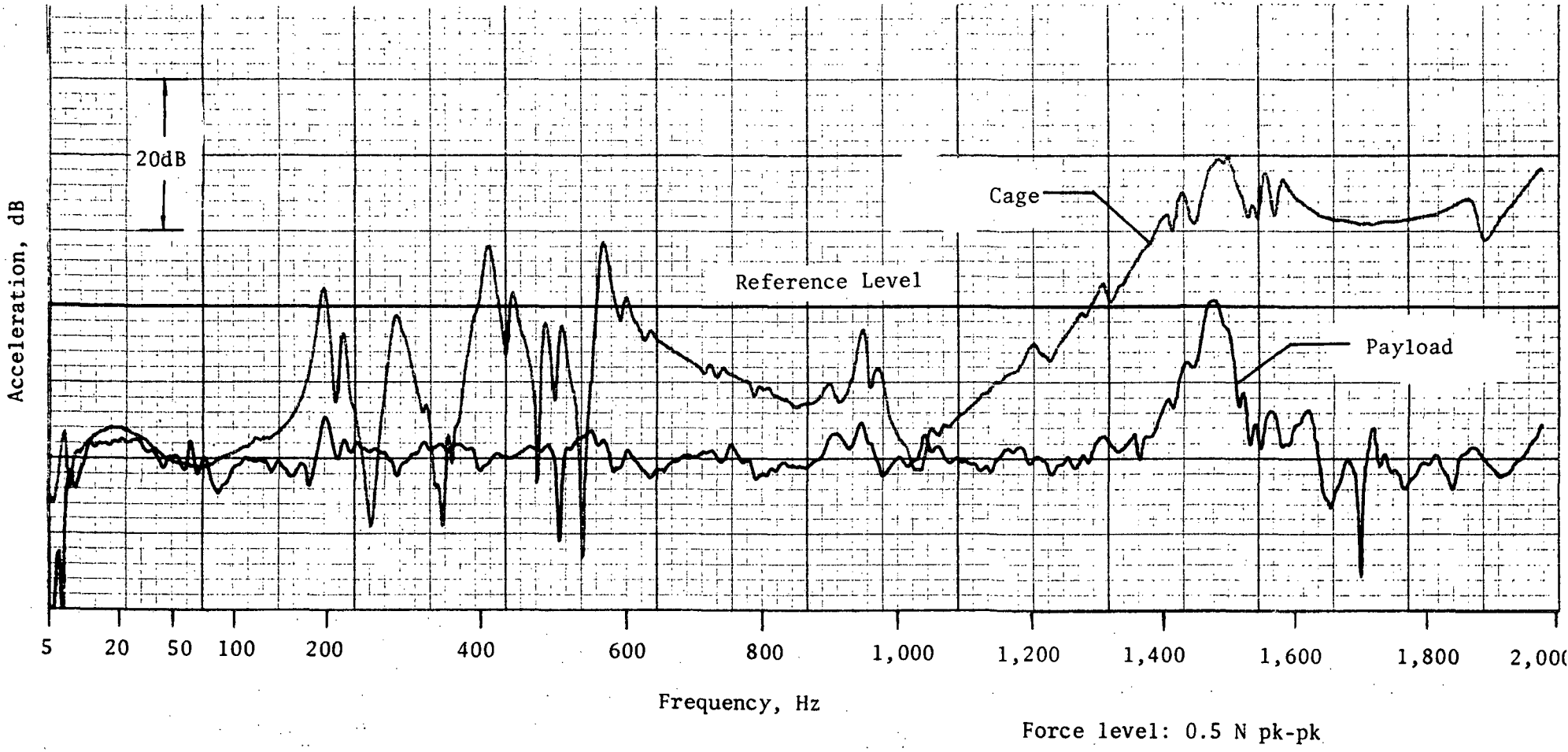

Force level: 0.5 N pk-pk

Figure 39-1 Test IIC, Sweep No. 1

Specimen Configuration: IA
Excitation: Axial-P1
Payload Sensor: Lower End of Tube
Damping: SFD Filled

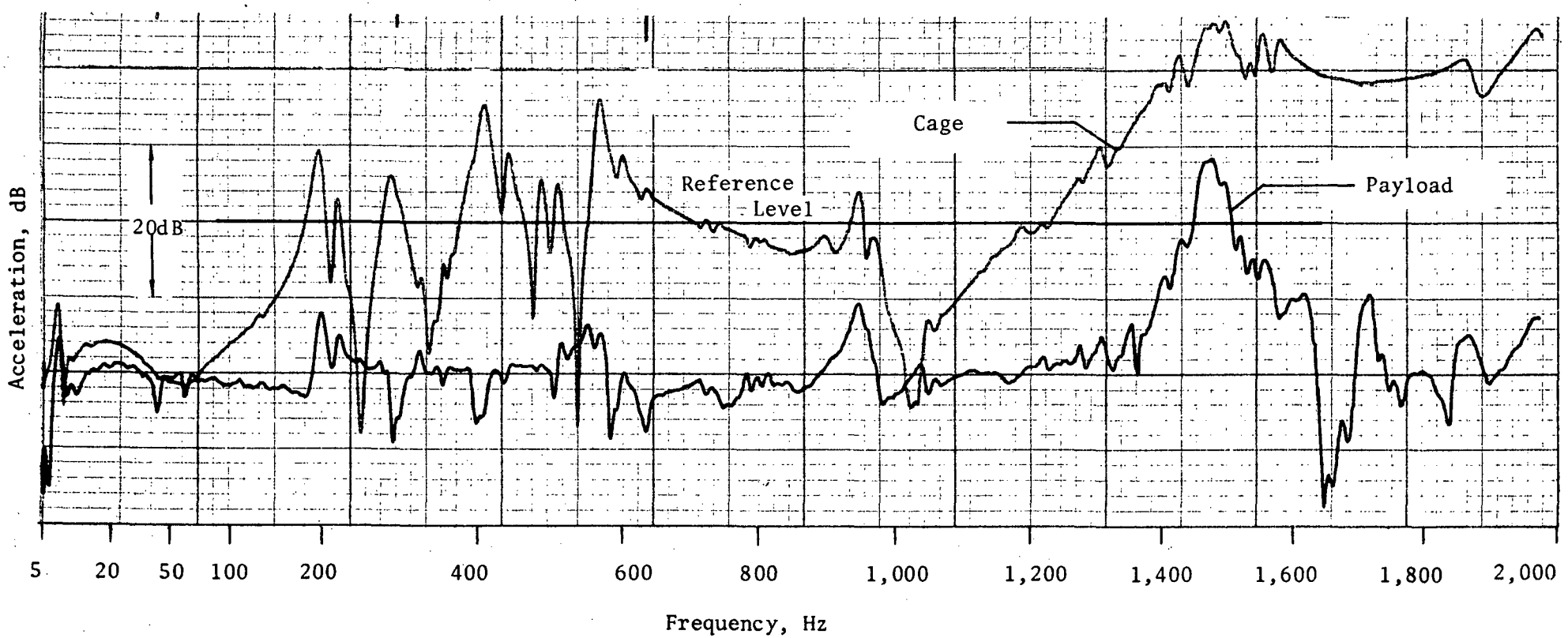

Force level: 1.25 N pk-pk

Figure 39-2 Test IIC, Sweep No. 2

Specimen Configuration: IA
Excitation: Axial-P1
Payload Sensor: Lower End of Tube
Damping: SFD Filled

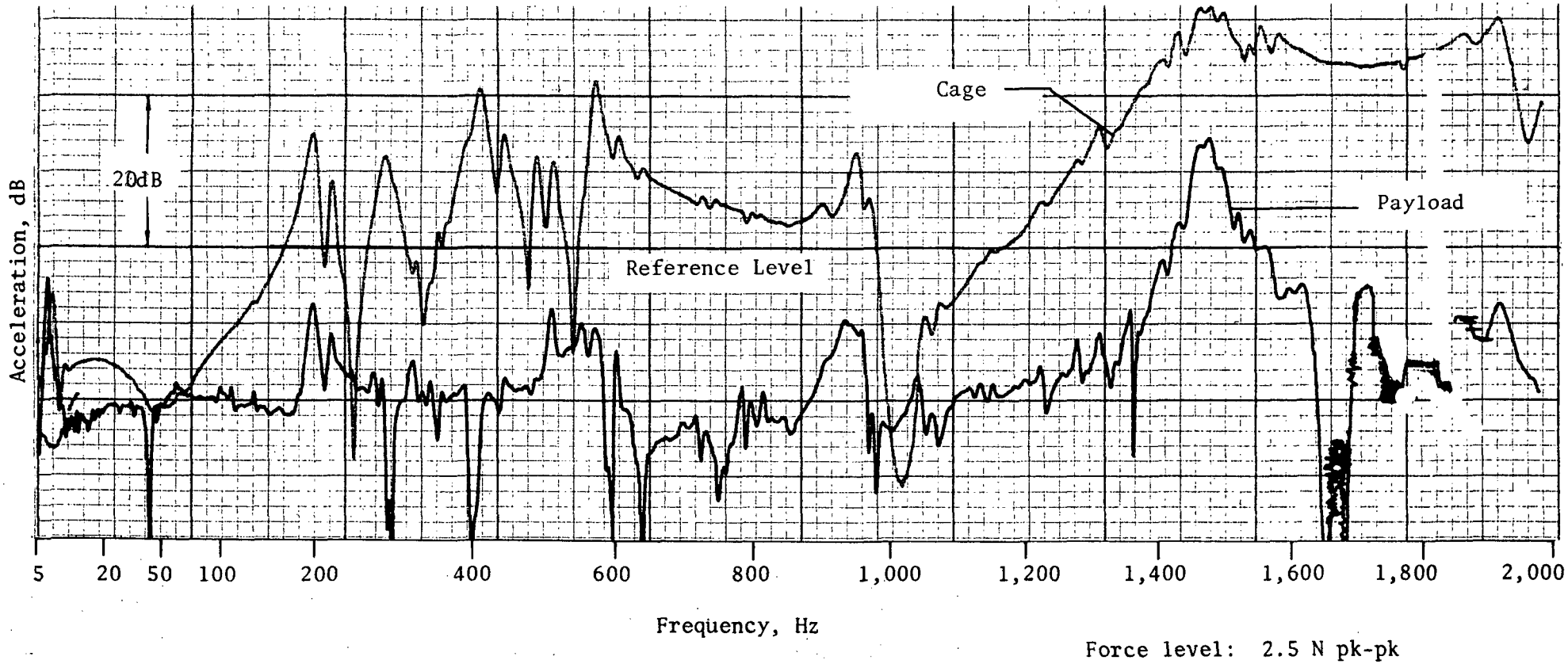

Force level: 2.5 N pk-pk

Figure 39-3 Test IIC, Sweep No. 3

Specimen Configuration: IA
Excitation: Axial-P1
Payload Sensor; Lower End of Tube
Damping: SFD Filled

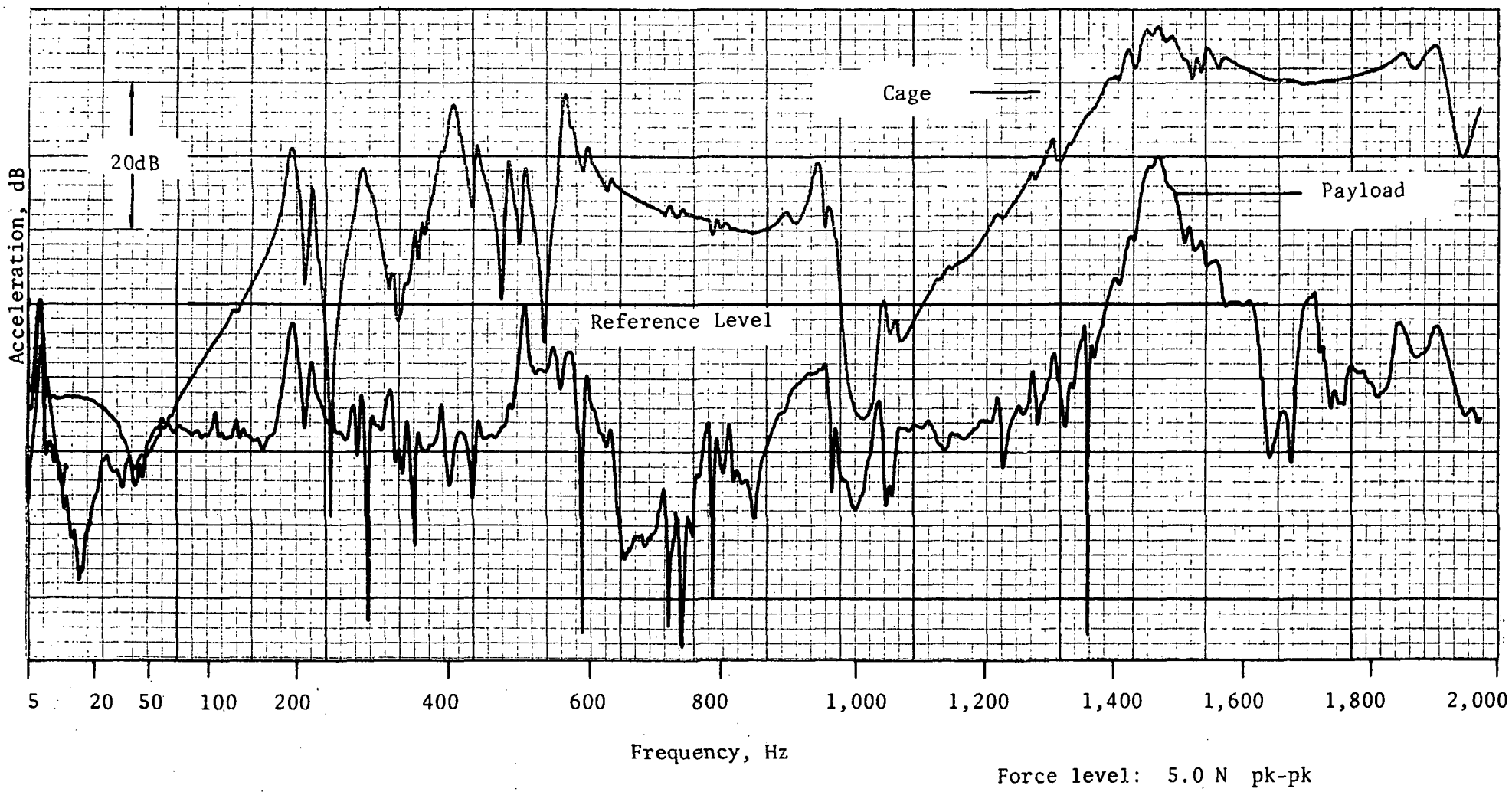

Force level: 5.0 N pk-pk

Figure 39-4 Test IIC, Sweep No. 4

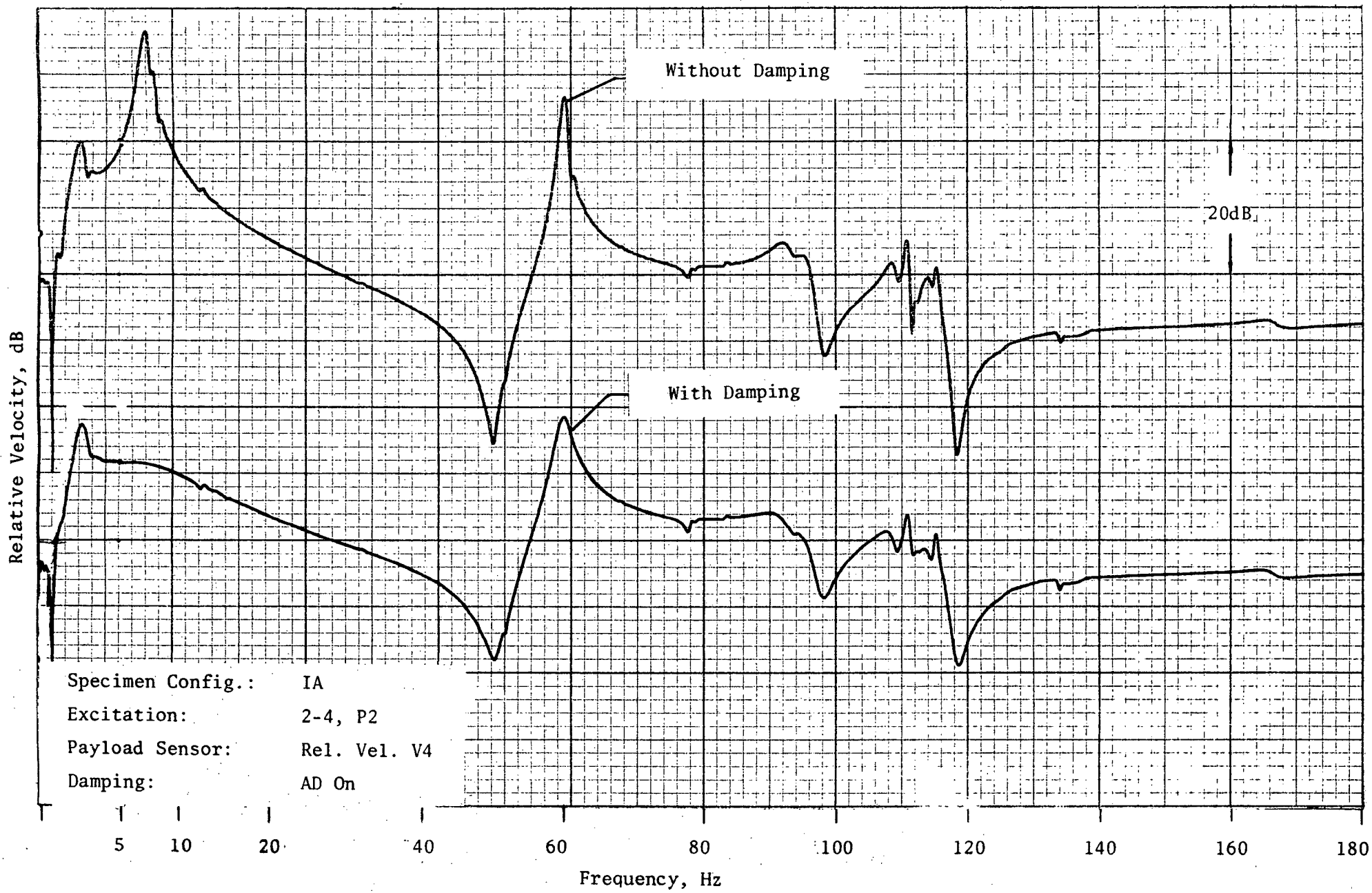

Figure 40 Test IID

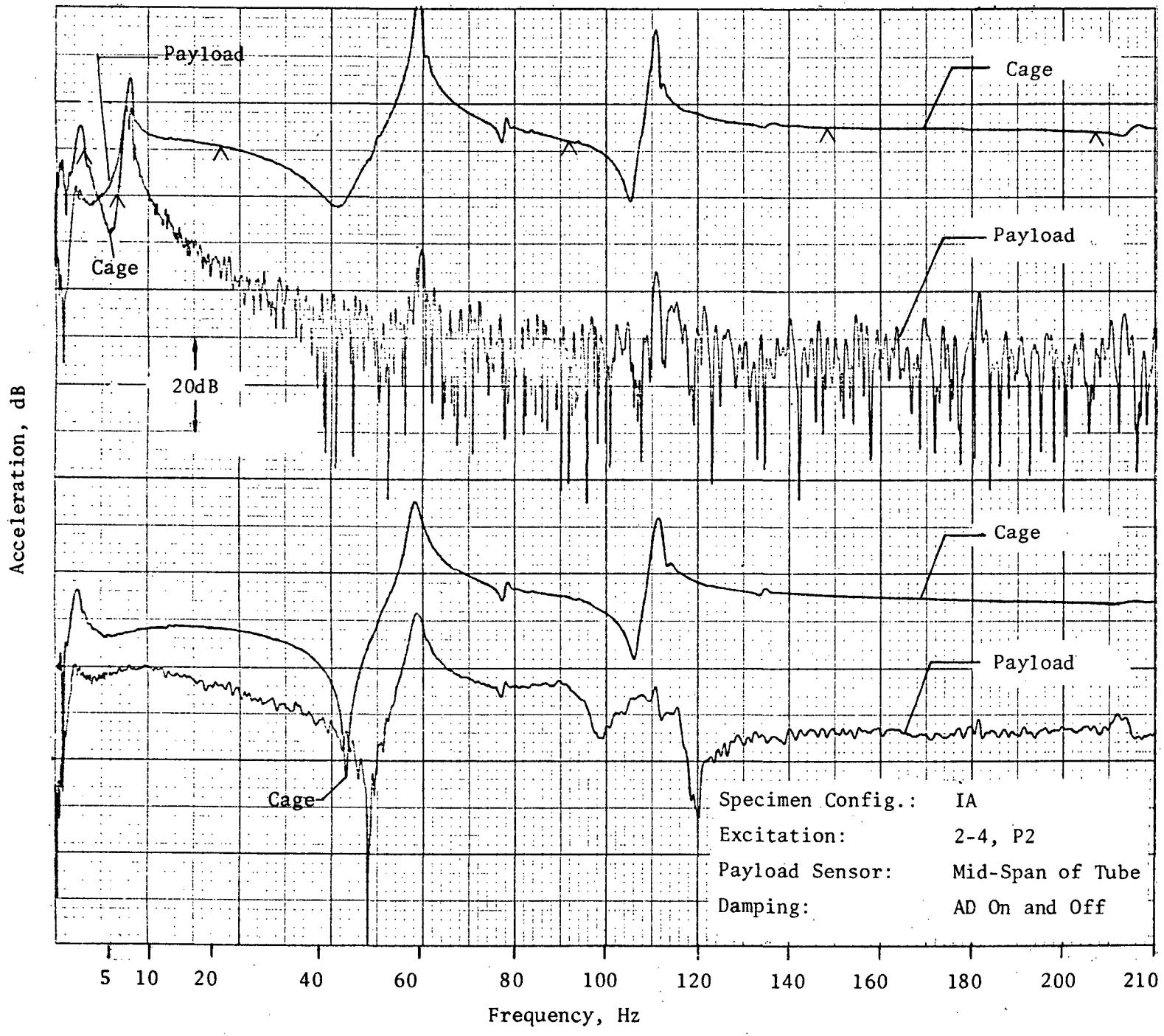

Figure 41 Test IIE

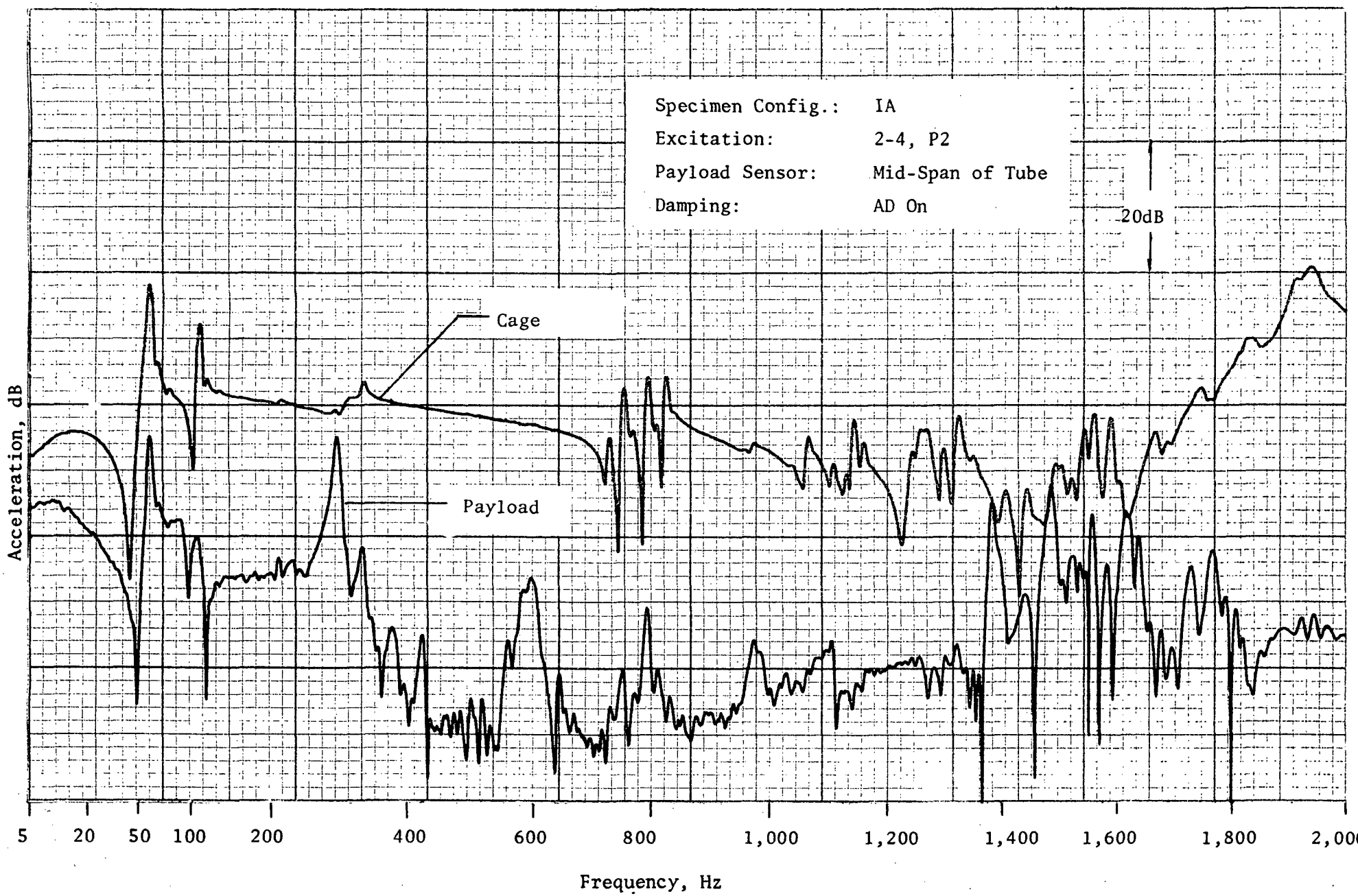

Figure 42 Test IIF

Specimen Config.: IB
Excitation: Axial-P1
Payload Sensor: Mid-Span of Tube
Damping: SFD Empty

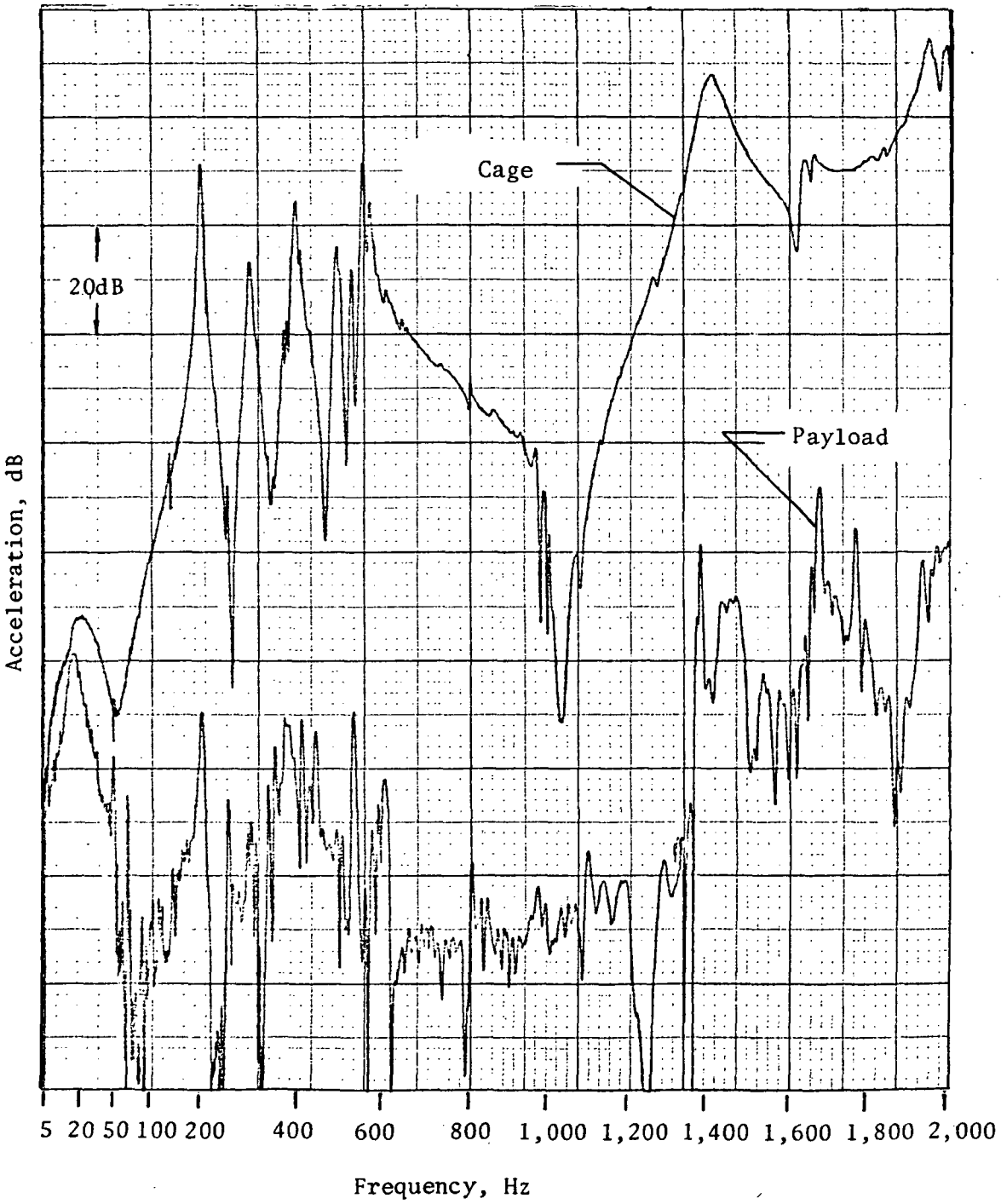

Figure 43 Test IIG

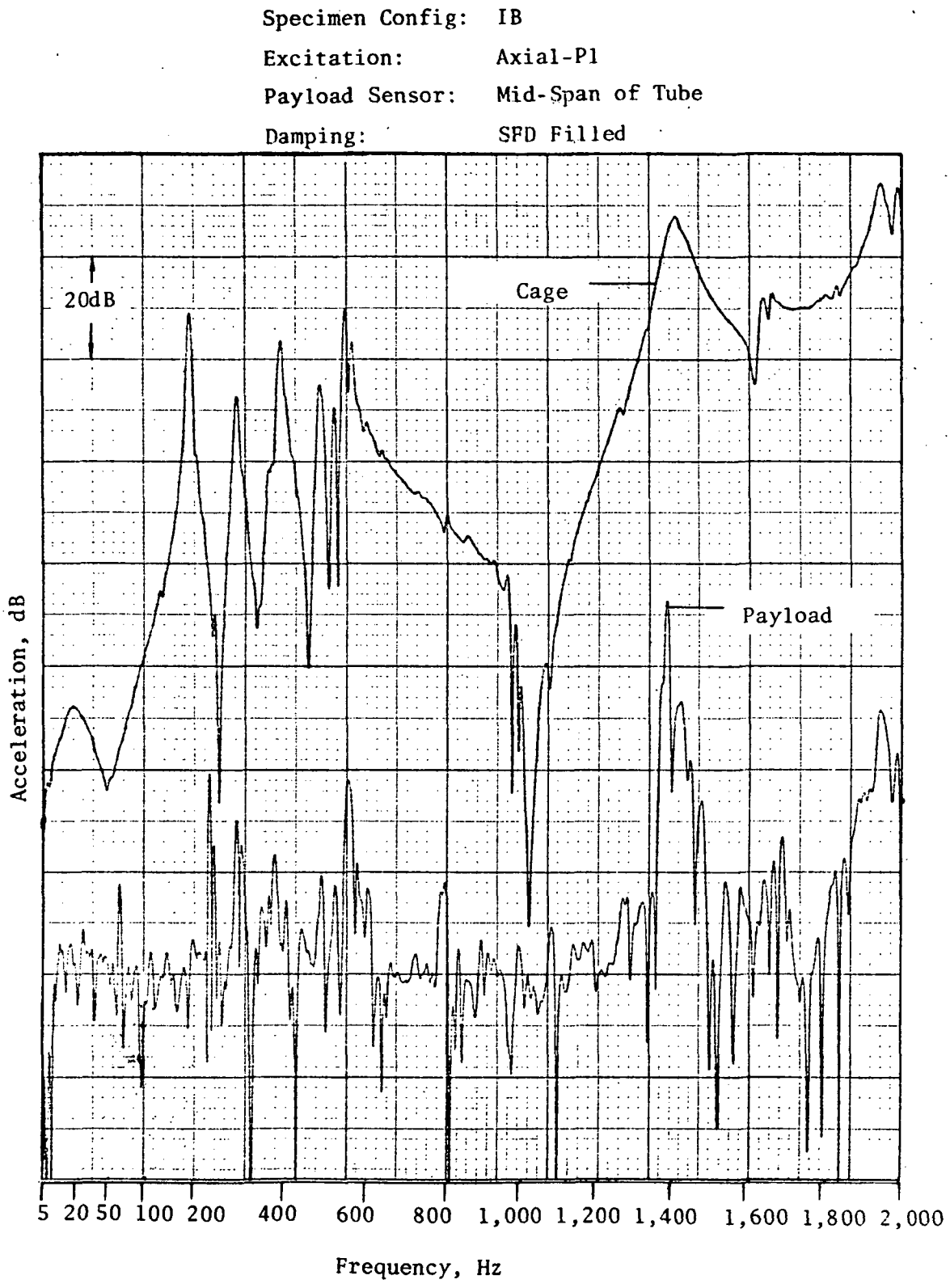

Figure 44 Test IIH

Specimen Config.: IB

Excitation: 1-3, P3

Payload Sensor: Mid-Span of Tube

Damping: AD Off

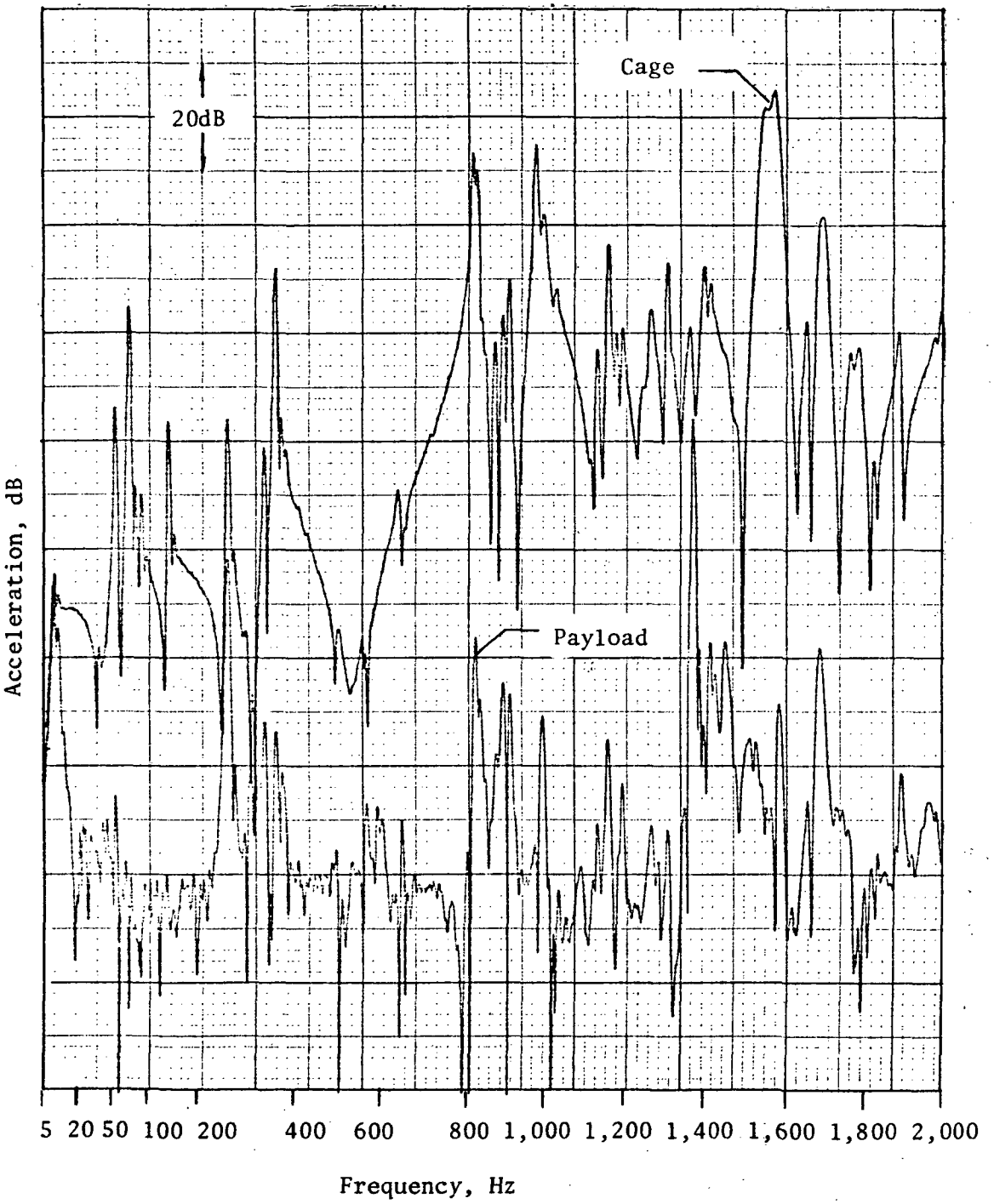

Figure 45 Test IIJ

Specimen Config.: IB

Excitation: 1-3, P3

Payload Sensor: Mid-Span of Tube

Damping: AD On

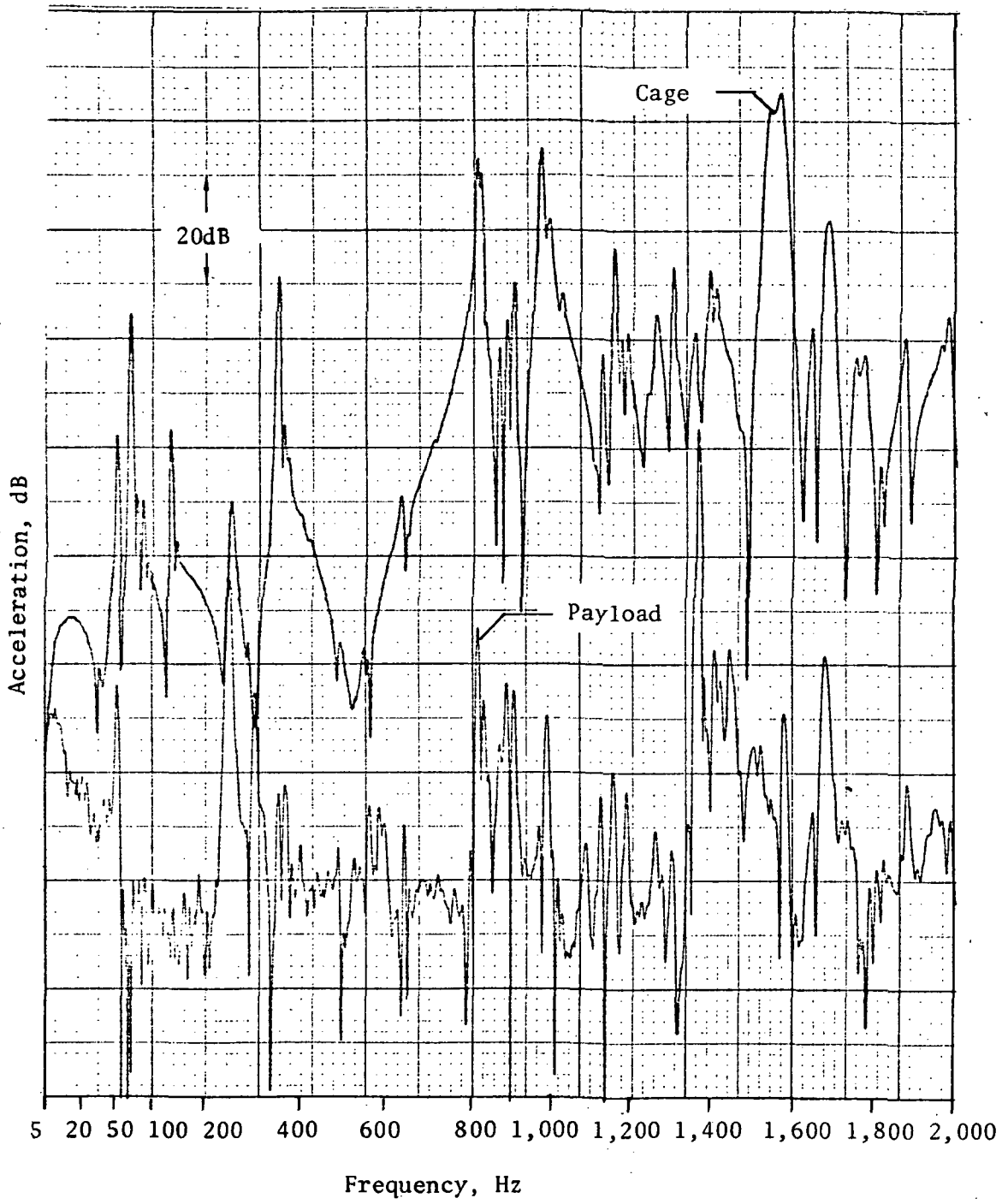

Figure 46 Test IIK

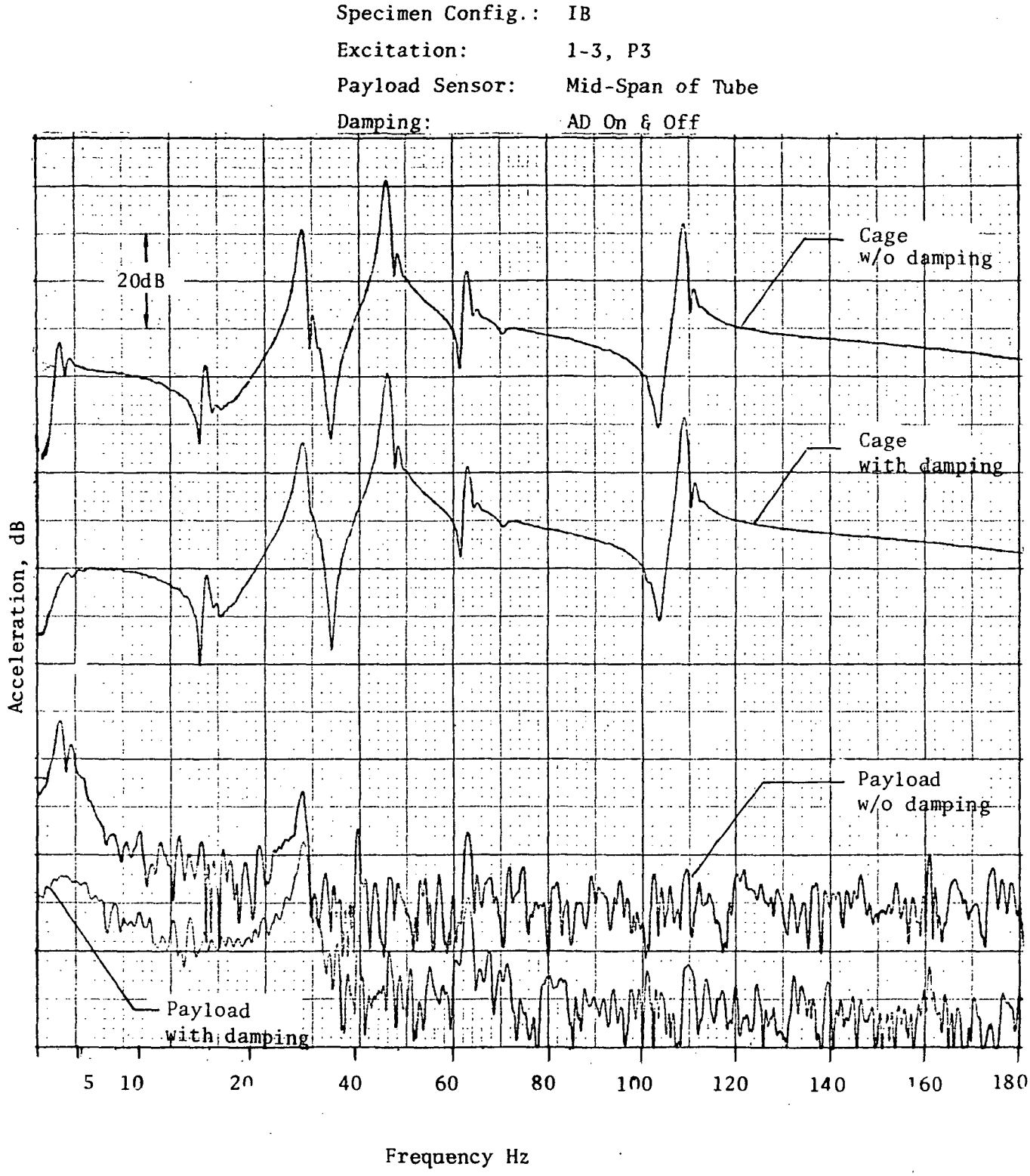

Figure 47 Test IIL

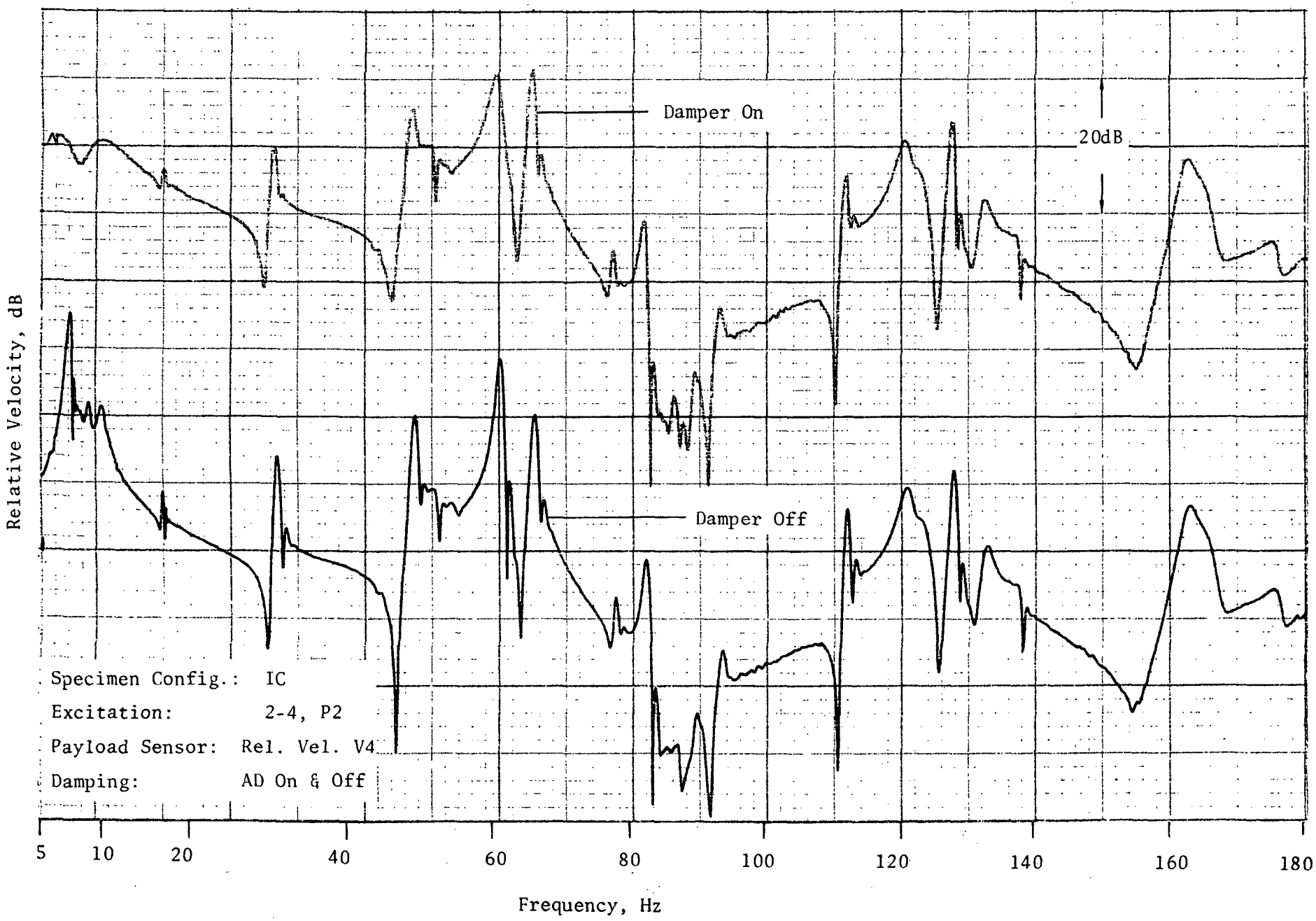

Figure 48 Test IIM

Specimen Config.: IC
Excitation: Axial-P1
Payload Sensor: Mid-Span of Tube
Damping: SFD Empty & Filled

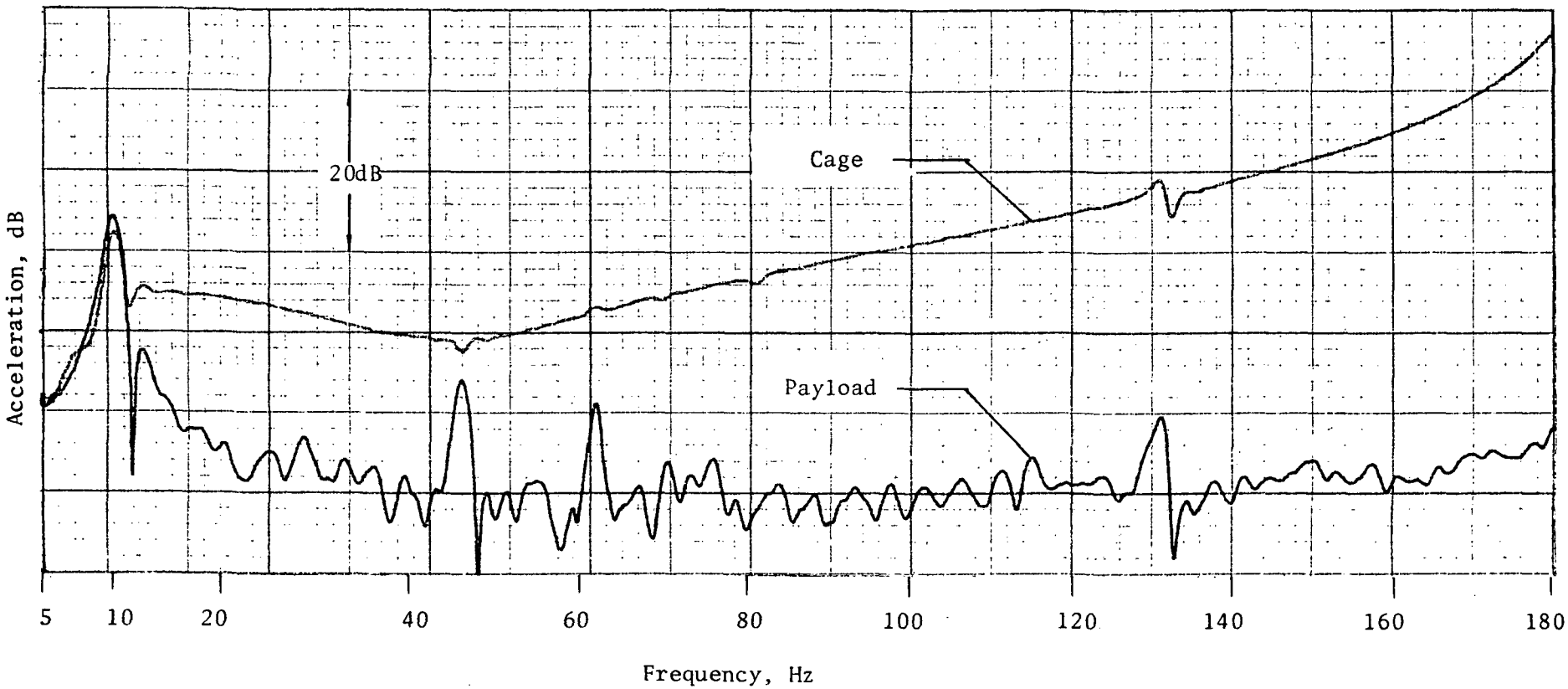

Figure 49-1 Test IIN, Without Damping